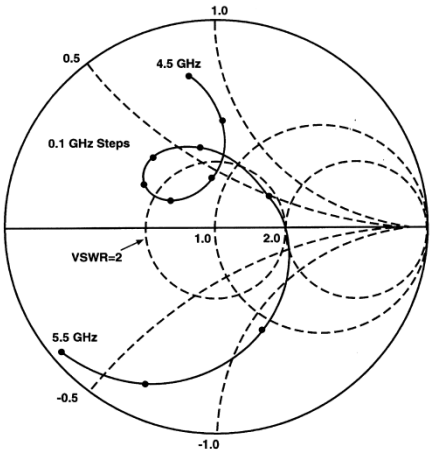

Applied Computational Electromagnetics Society Journal

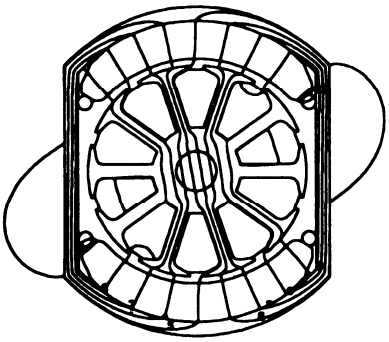

Editor-in-Chief
Atef Z. Elsherbeni

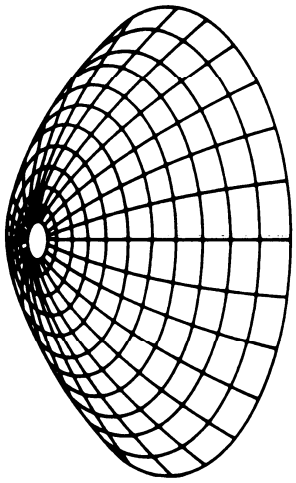

November 2010
Vol. 25 No. 11
ISSN 1054-4887

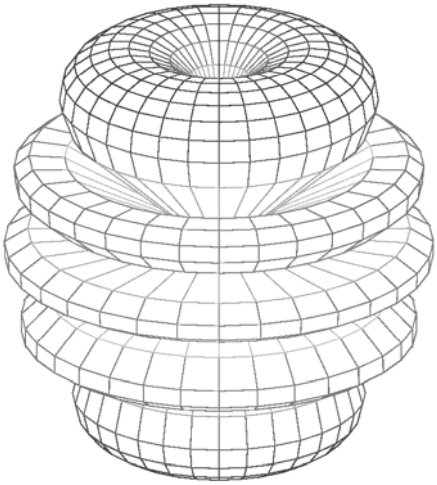

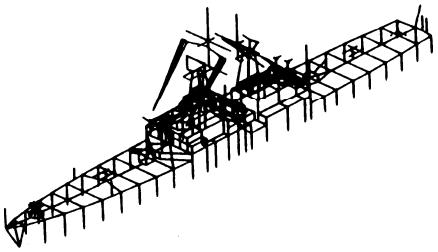

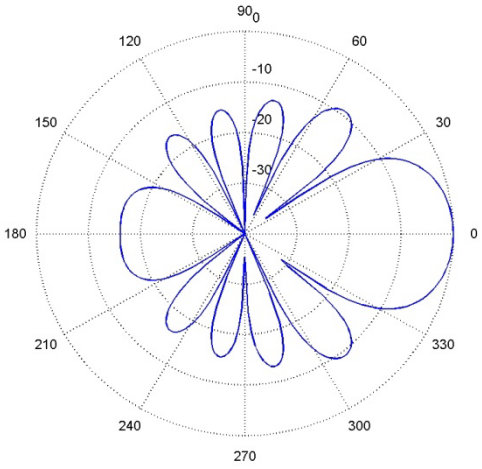

GENERAL PURPOSE AND SCOPE: The Applied Computational Electromagnetics Society ***(ACES)*** Journal hereinafter known as the ***ACES Journal*** is devoted to the exchange of information in computational electromagnetics, to the advancement of the state-of-the art, and the promotion of related technical activities. A primary objective of the information exchange is the elimination of the need to "re-invent the wheel" to solve a previously-solved computational problem in electrical engineering, physics, or related fields of study. The technical activities promoted by this publication include code validation, performance analysis, and input/output standardization; code or technique optimization and error minimization; innovations in solution technique or in data input/output; identification of new applications for electromagnetics modeling codes and techniques; integration of computational electromagnetics techniques with new computer architectures; and correlation of computational parameters with physical mechanisms.

SUBMISSIONS: The ***ACES Journal*** welcomes original, previously unpublished papers, relating to applied computational electromagnetics. Typical papers will represent the computational electromagnetics aspects of research in electrical engineering, physics, or related disciplines. However, papers which represent research in applied computational electromagnetics itself are equally acceptable.

Manuscripts are to be submitted through the upload system of ***ACES*** web site http://aces.ee.olemiss.edu See "Information for Authors" on inside of back cover and at ***ACES*** web site. For additional information contact the Editor-in-Chief:

Dr. Atef Elsherbeni
Department of Electrical Engineering
The University of Mississippi
University, MS 386377 USA
Phone: 662-915-5382 Fax: 662-915-7231
Email: atef@olemiss.edu

SUBSCRIPTIONS: All members of the Applied Computational Electromagnetics Society who have paid their subscription fees are entitled to receive the ***ACES Journal*** with a minimum of three issues per calendar year and are entitled to download any published journal article available at http://aces.ee.olemiss.edu.

Back issues, when available, are $15 each. Subscriptions to ***ACES*** is through the web site. Orders for back issues of the ***ACES Journal*** and changes of addresses should be sent directly to ***ACES***:

Dr. Allen W. Glisson
302 Anderson Hall
Dept. of Electrical Engineering
Fax: 662-915-7231
Email: aglisson@olemiss.edu

Allow four week's advance notice for change of address. Claims for missing issues will not be honored because of insufficient notice or address change or loss in mail unless the Executive Officer is notified within 60 days for USA and Canadian subscribers or 90 days for subscribers in other countries, from the last day of the month of publication. For information regarding reprints of individual papers or other materials, see "Information for Authors".

LIABILITY. Neither ***ACES***, nor the ***ACES Journal*** editors, are responsible for any consequence of misinformation or claims, express or implied, in any published material in an ***ACES Journal*** issue. This also applies to advertising, for which only camera-ready copies are accepted. Authors are responsible for information contained in their papers. If any material submitted for publication includes material which has already been published elsewhere, it is the author's responsibility to obtain written permission to reproduce such material.

APPLIED COMPUTATIONAL ELECTROMAGNETICS SOCIETY JOURNAL

Editor-in-Chief
Atef Z. Elsherbeni

November 2010
Vol. 25 No. 11
ISSN 1054-4887

The ACES Journal is abstracted in INSPEC, in Engineering Index, DTIC, Science Citation Index Expanded, the Research Alert, and to Current Contents/Engineering, Computing & Technology.

The first, fourth, and sixth illustrations on the front cover have been obtained from the Department of Electrical Engineering at the University of Mississippi.

The third and fifth illustrations on the front cover have been obtained from Lawrence Livermore National Laboratory.

The second illustration on the front cover has been obtained from FLUX2D software, CEDRAT S.S. France, MAGSOFT Corporation, New York.

THE APPLIED COMPUTATIONAL ELECTROMAGNETICS SOCIETY
http://aces.ee.olemiss.edu

ACES JOURNAL EDITOR-IN-CHIEF

Atef Elsherbeni
University of Mississippi, EE Dept.
University, MS 38677, USA

ACES JOURNAL ASSOCIATE EDITORS-IN-CHIEF

Sami Barmada
University of Pisa. EE Dept.
Pisa, Italy, 56126

Fan Yang
University of Mississippi, EE Dept.
University, MS 38677, USA

Mohamed Bakr
McMaster University, ECE Dept.
Hamilton, ON, L8S 4K1, Canada

ACES JOURNAL EDITORIAL ASSISTANTS

Matthew J. Inman
University of Mississippi, EE Dept.
University, MS 38677, USA

Mohamed Al Sharkawy
Arab Academy for Science and
Technology, ECE Dept.
Alexandria, Egypt

Christina Bonnington
University of Mississippi, EE Dept.
University, MS 38677, USA

Khaled ElMaghoub
University of Mississippi, EE Dept.
University, MS 38677, USA

Anne Graham
University of Mississippi, EE Dept.
University, MS 38677, USA

ACES JOURNAL EMERITUS EDITORS-IN-CHIEF

Duncan C. Baker
EE Dept. U. of Pretoria
0002 Pretoria, South Africa

Allen Glisson
University of Mississippi, EE Dept.
University, MS 38677, USA

David E. Stein
USAF Scientific Advisory Board
Washington, DC 20330, USA

Robert M. Bevensee
Box 812
Alamo, CA 94507-0516, USA

Ahmed Kishk
University of Mississippi, EE Dept.
University, MS 38677, USA

ACES JOURNAL EMERITUS ASSOCIATE EDITORS-IN-CHIEF

Alexander Yakovlev
University of Mississippi, EE Dept.
University, MS 38677, USA

Erdem Topsakal
Mississippi State University, EE Dept.
Mississippi State, MS 39762, USA

NOVEMBER 2010 REVIEWERS

John Aldrin
Shirook Ali
Sami Barmada
J. Berenger
Raghvendra Chaudhary
Jorge Costa
Khaled El Mahgoub
Said El-Khamy
Antonio Espirito Santo
Chrisophe Fumeaux
Fernando Las-Heras
Paolo Mezzanotte
Andrew Peterson
Lionel Pichon
C. J. Reddy
Colan Ryan
Ari Sihvola
Abhay Srivastava
Erdem Topsakal
Alexander Yakovlev
Su Yan
Huapeng Zhao
Shouzheng Zhu

THE APPLIED COMPUTATIONAL ELECTROMAGNETICS SOCIETY

JOURNAL

Vol. 25 No. 11 November 2010

TABLE OF CONTENTS

"Grid-Based SCT Approach for the Global Electromagnetic Simulation and Design of Finite-Size and Thick Dichroïc Plate"
F. Khalil, E. B. Tchikaya, R. Sharrock, T. Monteil, F. Coccetti, and H. Aubert….....903

"Preconditioned MDA-SVD-MLFMA for Analysis of Multi-Scale Problems"
Z. N. Jiang, Z. H. Fan, D. Z. Ding, R. S. Chen, and K. W. Leung……914

"Parallel SAI Preconditioned Adaptive Integral Method For Analysis of Large Planar Microstrip Antennas"
M. Li, M. Chen, W. Zhuang, Z. Fan, and R. Chen…….….....926

"Well-Conditioned CFIE for Scattering from Dielectric Coated Conducting Bodies above a Half-Space"
D. Ding, J. Ge, and R. Chen……..….....936

"Robust Beamforming Technique with Sidelobe Suppression Using Sparse Constraint on Beampattern"
Y. Zhang, H. Zhao, J. P. Lie, B. P. Ng, and Q. Wan…….....947

"A Frequency-Dependent Hybrid Implicit-Explicit FDTD Scheme for Dispersive Materials"
J. Chen and A. Zhang……..….....956

"Adaptive Mixed-Form Fast Multipole Method for the Analysis of Electromagnetic Scattering"
H. Chen, Z. H. Fan, R. S. Chen, Z. N. Jiang, and M. M. Li…….....962

"Improved Microstrip Folded Tri-Section Stepped Impedance Resonator Bandpass Filter using Defected Ground Structure"
N. M. Garmjani and N. Komjani…….....975

"Impact of the Mobile Phone Dimensions on the Hearing Aids Compatibility"
I. B. Bonev, O. Franek, M. Christensen, and G. F. Pedersen…….....984

"Parametric Analysis of Multi Source Feeding Flare Rolling and Corrugating Effects for H-Plane Horn Radiator"
A. S. Turk and O. Yurduseven……..….....992

© 2010, The Applied Computational Electromagnetics Society

Grid-Based SCT Approach for the Global Electromagnetic Simulation and Design of Finite-Size and Thick Dichroïc Plate

Fadi Khalil [1, 2], Euloge B. Tchikaya [1, 2], Rémi Sharrock [1, 2], Thierry Monteil [1, 2], Fabio Coccetti [1, 2], and Hervé Aubert [1, 2]

[1] CNRS, LAAS, 7 avenue du colonel Roche, F-31077 Toulouse, France

[2] Université de Toulouse, UPS, INSA, INP, ISAE, LAAS, F-31077 Toulouse, France
fadi.khalil@laas.fr, ebtchika@laas.fr, rsharrock@laas.fr,
monteil@laas.fr, fcoccett@laas.fr, haubert@laas.fr

Abstract ─ In the work presented in this paper, a grid-enabled environment for the scale changing technique (SCT) simulations is proposed. This approach allows the fast design of a finite size and thick dichroïc metallic mirror based on global electromagnetic simulation. The computed transmission and reflection coefficients, as well as radiation pattern, satisfying to some predefined technical requirements in X and Ka frequency bands are presented. Simulation results are shown in order to demonstrate the validity of the approach.

Index Terms ─ Dichroïc mirror, distributed computing, electromagnetic analysis, frequency selective surfaces, grid computing, SCT.

I. INTRODUCTION

The trend in radio frequency (RF) and microwave design is towards the accurate prediction of system-level performance and behavior. Engineers simulate larger and more sophisticated design problems in support of that goal. When it involves both large structures (in terms of wavelength) and fine details, the system or structure is said to be complex. The higher the number of scale levels in the system the higher is the complexity. Well-known examples of complex structures are provided by multi-band frequency-selective surfaces, finite-size arrays of non-identical cells and fractal planar objects. Electromagnetic modeling of such structures has been recently discussed [1-2]. In order to simulate such complex multi-scale structures, an efficient electromagnetic approach, named thus scale changing technique (SCT) [3], is used here. The SCT method allows the global simulation of a finite-size thick dichroïc mirror as shown in [4], and detailed here in this article. The scope is to define the most appropriate design of a uniform mirror satisfying to predefined technical requirements of transmission and reflection coefficients in X and Ka frequency bands. Consequently, parametric simulations must be performed.

The parametric distributed study application is now a good candidate to execute in a grid computing (GC) environment [5]. GC has emerged as an important new field, distinguished from conventional distributed computing by its focus on large-scale resource sharing, innovative applications, and, in some cases, high-performance orientation [5-6]. GC provides a safe and pervasive access to dynamically distributed computing resources, providing greater availability, reliability, and cost efficiencies that may exist with dedicated servers. In addition to the central processing unit (CPU) and storage resources, it can provide access to increased quantities of other (shared) resources and to special equipment, software, licenses, and other services.

The SCT has proven itself as a powerful tool for electromagnetic simulation of frequency selective surfaces. Various dimensions of the dichroïc mirror have been simultaneously simulated on GC nodes in order to minimize the

1054-4887 © 2010 ACES

simulation time. Overall computation time for deriving transmission, reflection coefficients, and the radiation pattern of arrays was significantly reduced compared to sequential computation while keeping the solver accuracy by deploying these simulations in distributed environments as GC.

This article is composed of two main parts. First, the frequency selective surfaces and modeling issues are discussed in section II, followed by the scale changing technique (SCT) modeling description in section III.

In the second part, the SCT algorithm is discussed and distributed computing in grid environments is presented in two different approaches. Simulation results, compared to other simulation tools, are shown here.

Finally, in section V, an overview of the key advantages of this approach coupled with SCT in the global electromagnetic analysis and design of the frequency selective surfaces is reported.

II. THE FREQUENCY SELECTIVE SURFACES

The frequency selective surfaces (FSSs) are a key component in the design of multi-frequency systems. They are used as frequency filters, and find applications, e.g. radomes and Cassegrain antenna reflectors. By nature, the FSS play the role of filters, allowing the transmission of certain frequencies and the reflection of others. They generally consist of a periodic array of conducting elements printed on a dielectric substrate, or of an array of apertures in a metallic plate. The nature and the geometry of the element (patch or aperture) are very important in the determination of the frequency response of the structure, like its bandwidth and transfer function. FSS performances depend strongly on the angle of incidence and polarization of the incident electromagnetic waves [7-8]. In our case study, we consider only a perforated metallic plate or roasts metal illuminated by a plane wave (with arbitrary angles of incidence).

Traditionally, FSS performances are assessed by making the assumption of infinite size and periodical FSS by using Floquet modes. Consequently, the computing time is being reduced almost to that of the basic cell.

To take into account the finite size of the array, several methods have been developed [9-10]. Note also that most of the methods treat only FSS with small thickness. However, the simulation of the FSS by the traditional numerical methods based on spatial meshing (finite element method, finite difference method, and method of the moments) or spectral discretization (modal methods) often leads to badly ill-matrix, numerical convergence problems and/or excessive computation times. To avoid all these problems, we adapt to the identified problem an original technique, called the scale changing technique, based on various scales modeling of complicated structures and whose principle consist in the idea that it is desirable to dissociate (separate) the complex problem into several simpler problems (Cf. Section III).

For numerous applications, the FSS is generally in the near field region, so that the operation of the cell strongly depends on its position in the array. The possibility offered by SCT to optimize a non-periodic grid, with each element selected according to its position in the array, should make it possible to improve the response of the FSS usually used, in particular to reduce their impact on the radiation diagram of the source in transmission (deformation of the mean lobe, high cross-polarization…).

Since the SCT allows global electromagnetic simulation of FSS, it will be used here to define the best dimensions design of dichroïc mirror satisfying to predefined reflection and transmission conditions in X and Ka frequency bands without using Floquet modes. It allows taking into account the finite size of the array as well as its thickness. The grid computing nodes will be used to run this parametric study.

III. THE SCALE CHANGING TECHNIQUE

The SCT is an efficient monolithic (unique) formulation for the electromagnetic modeling of complex (multi-scale) structures i.e., structures that exhibit multiple metallic patterns whose sizes cover a large range of scales [3].

SCT consists of interconnecting scale-changing networks (SCN), each network models the electromagnetic coupling between adjacent scale levels. The cascade of the scale changing networks allows the global electromagnetic simulation of multi-scale structures, from the smallest to the highest scale.

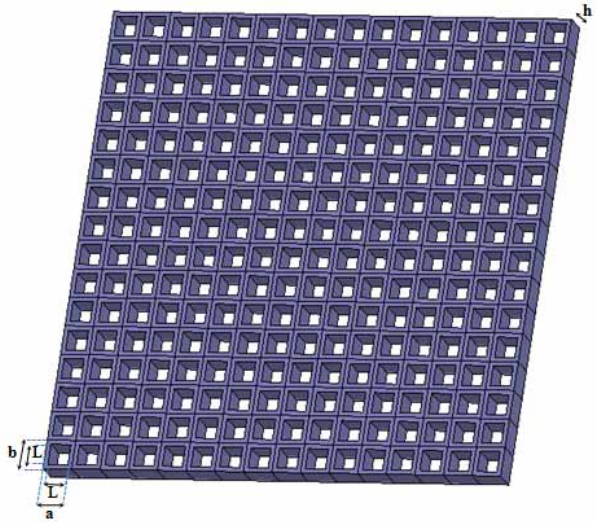

Fig. 1. Topology of a FSS consisting of uniform rectangular waveguides perforating a thick metallic plate.

The global electromagnetic simulation of multi-scale structures via the cascade of the scale changing networks has been applied with success to the design and electromagnetic simulation of specific planar structures such as reconfigurable phase-shifters [11, 12], fractal selective surfaces [13], discrete self-similar (pre-fractal) scatterers [14, 15], and patch antennas [16, 17]. This scale-changing technique is a very fast technique and this makes it a very powerful investigation, design and optimization tool for engineers who design complex circuits [18 - 20].

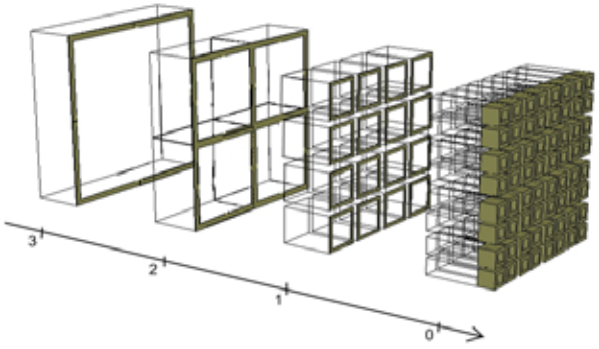

Fig. 2. An example of partitioning of finite size and thick dichroïc metallic mirror.

The proposed topology consists of a metallic grid of thickness h = 5 mm, with a = b = 10 mm (Cf. Figure 1). The dimensions of the apertures are uniform and the cells have the same thickness. To demonstrate the potential of the method, we consider the transmission and reflection coefficients of a finite size (256 cells) uniform FSS illuminated by a normal incident plane wave, as well as the radiation pattern.

A. Partitioning of the finite size and thick dichroïc metallic mirror

The starting point of the proposed approach consists of the coarse partitioning of the dichroïc mirror into large-scale (called scale level s_{max}) sub-domains of arbitrary shape; in each sub-domain a second partitioning is then performed by introducing smaller sub-domains at scale level $s_{max}-1$; again, in each sub-domain introduced at scale level $s_{max}-1$ a third partitioning is performed by introducing smaller sub-domains at scale level $s_{max}-2$; and so on. Such hierarchical domain-decomposition, which allows us to focus rapidly on increasing detail in the dichroïc mirror plane, is stopped when the finest partitioning (scale level s=0) is reached. An illustration of the partitioning of a metallic grid of 265 cells is sketched in Figure 2. We can easily see that a high scale ratio exists between the highest and the smallest dimensions. Four different scale levels exist when cells are grouped by four. Boundary conditions (perfect electric or perfect magnetic boundary conditions) are artificially introduced at the contour of all the sub-domains generated by the partitioning process, taking into account the physics of the problem.

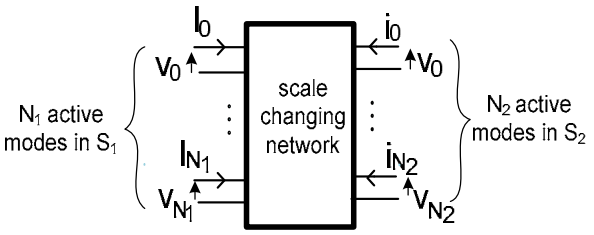

Fig. 3. A scale changing network (SCN) [1].

The next step consists of computing the electromagnetic coupling between two successive scale levels via the scale changing network (SCN) (Cf. Figure 3). The cascade of SCNs allows crossing the scale from the lowest scale (s=0) to the highest one ($s=s_{max}$).

The scale changing technique can be applied several times to different scale levels. The transition from one level to another level is

modeled by multiport associated with active modes of the two scales.

B. Surface impedance matrix

Consider the pattern given in Figure 4(a), where the thickness is taken into account. It presents a passive sub-domain Ds containing many fine geometrical details and composed of: (1) the perfect conductor domain D_M and (2) the aperture domain D_A, with $D_S = D_M \cup D_A$ (Figure 4(b)).

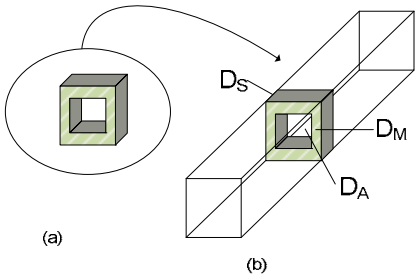

Fig. 4. (a) Initial lossless metallic pattern with a passive sub-domain DS presenting many fine geometrical details; (b) artificial rectangular waveguide of cross section DS in which the set of propagating and evanescent modes constitutes the basis for the electromagnetic field.

The electromagnetic field in Ds can be expanded on a local modal electromagnetic field in basis. Such basis can be viewed as the set of propagating and evanescent modes in the artificial rectangular waveguide of cross section. The time average electromagnetic energy stored by higher-order evanescent modes is localized in the vicinity of discontinuities or geometrical details of the planar structure. Consequently the contribution of such modes in the expansion of the electromagnetic field is expected to be insensitive to the choice of the surface, as far as the boundary conditions enclosing this surface are applied sufficiently far from discontinuities. We consider here that such modes are shunted by their (pure imaginary) impedance and are called *passive* by analogy with variational techniques in waveguide discontinuities. The electromagnetic coupling between the lower-order –or active– modes is characterized by the surface impedance matrix Zs (or admittance matrix Ys) and consequently, the original sub-domain is replaced by surface impedance (or admittance) boundary conditions.

C. S-parameters calculation

The thick metallic grid presents a symmetry plane cutting the thickness of the plate in two equal parts (Figure 5(a)).

The grid impedance matrix $[Z_{total}]$ can then be derived from the combination of the two impedance matrices $[Z_{even}]$ and $[Z_{odd}]$ of half-structures obtained by inserting respectively a magnetic wall and electric wall in the symmetry plane, as follows [5]:

$$[Z_{total}] = \frac{1}{2}\begin{pmatrix} [Z_{even}] + [Z_{odd}] & [Z_{even}] - [Z_{odd}] \\ [Z_{even}] - [Z_{odd}] & [Z_{even}] + [Z_{odd}] \end{pmatrix}. \quad (1)$$

The scattering matrix $[S_{total}]$ is then deduced from the following relationship:

$$[S_{total}] = ([Z_{total}] - [Z_0])([Z_{total}] + [Z_0])^{-1} \quad (2)$$

where $[Z_0]$ designates the diagonal matrix of active mode impedances. The scale changing technique is applied for the derivation of matrices $[Z_{even}]$ and $[Z_{odd}]$ associated with half-structures.

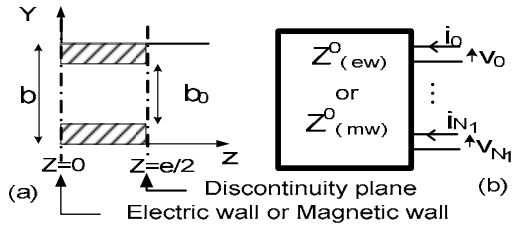

Fig. 5. (a) Side-view of half of the unit-cell for magnetic and electric wall configurations. (b) Surface impedance multiport for modeling the unit-cell. N1 denotes the number of active modes at the smallest scale.

D. Radiation pattern calculation

We consider the scattering of the wave plane incident on the FSS, formed by a thick metal grid. The electromagnetic problem consists in calculating the field scattered by a perfect thick metallic surface when illuminated by a normal plane wave incidence:

$$\vec{E}^{inc} = E^{inc} \exp(jk_0 z)\vec{y}. \quad (3)$$

We consider here the field backscattered by the half-structure obtained by inserting a magnetic wall and electric wall in the symmetry plane z =0.

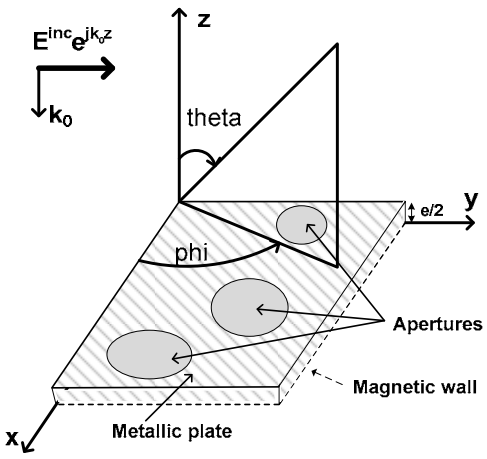

Fig. 6. Scattering problem in free space in the conventional coordinates system [14].

The induced current on the surface is defined while having the total electric field E^{total} equal zero. The integral equation in the electric field is obtained with the equivalence principle application.

With the SCT, we substitute the actual current *J* by an equivalent current *Jeq* defined by the lower-order modes (active modes) of the orthogonal modal-basis of domain S (FSS metallic grid).

The S domain is then characterized by a surface impedance matrix $[Z_s]$ (which fixes the boundary conditions of the problem) such as:

$$[E^{total}] = [Z_s][J_{eq}] \tag{4}$$

$$\vec{J}_{eq} = \sum_{i=1}^{NxN} I_{eq\_i}\, \vec{g}_{eq\_i}, \tag{5}$$

where $\vec{g}_{eq\_i}$ is an entire trial function of the modal basis.

To determine the solution of the boundary value problem in free space, we are led to calculate the electric field radiated by the equivalent current. This last item being expressed on a modal basis, it is better to solve the problem in the spectral domain. Under these conditions, the equation of the boundary value problem in free space becomes:

$$\vec{E}^{inc} + \hat{G}\vec{J}_{eq} = z_s\vec{J}_{eq,} \tag{6}$$

where Ĝ is the dyadic Green's function associated with free space in the spectral domain.

The application of the method of Galerkin makes it possible to establish the following matrix equation:

$$[V^{inc}] - [Z]\left[I_{eq}\right] = [z_s] \tag{7}$$

$$\left[I_{eq}\right] = ([Z] + [z_s])^{-1}[V^{inc}]. \tag{8}$$

The terms are obtained by the following scalar product:

$$[V_{inc}]_j = \langle \vec{g}_{e\_j}, E^{inc} \rangle. \tag{9}$$

The goal is to calculate the $\vec{J}_{eq}$ which will give the field diffracted by the grid. This current can be found from equation (8) if Z and Zs are known.

Z is calculated from free space Green's functions; Zs is calculated by applying the SCT and using the induction theorem and the images equivalent principle to make use of the symmetry of the problem along the z-axis [21].

The SCT is applied by introducing an artificial rectangular waveguide enclosed with periodic boundary conditions. Zs represents the surface impedance matrix of the entire structure after the connection of all bifurcation multiports. The computation is performed for even configuration. Since the structure is symmetric along z-axis, we wish to take this symmetry to consider only half space in the description of the problem.

IV. THE GRID-PARAMETRIC SCT SIMULATIONS

A. Structure of the SCT simulation

As mentioned before, the SCT is a hierarchical domain-decomposition. Consider the metallic grid sketched in Figure 2, with 256 cells. Four different scale levels exist when cells are grouped by four.

First, the dimensions of the studied structure, frequency band, as well as the number of modes (calculated in convergence study) are defined. After an initialization phase, the different SCNs are computed independently.

The algorithm calculates the different correspondent modules, *M,1 M,2 ... M256*, as well as the four modules representing the scale changing, *M257, M258, M259,* and *M260*. Once these modules are computed, the global electromagnetic simulation of multi-scale

structures is done via the cascade represented by *C,1 C2, ... C64*, *C65, ... C80*, *C81, ... C84*, and *C85*. *C1, C2, ... C64* are executed at the first cascade level, *C65 ... C80* at the second level, *C81 ... C84* at the third level and *C85* at the final one. Note that the number of cascades and SCNs depends on the partitioning of the problem and chosen sub-domains defined by the user.
The *SCT* program serial execution:

```
Initialization
     M1
     M2
     .
     .
     M256
     M257
     .
     M260
     C1
     C2
     .
     .
     C64
     C65
     .
     .
     C80
     C81
     .
     .
     C84
     C85
```

B. Grid execution

Two scenarios of grid computing can be applied here with SCT simulations. The first one consists of executing in parallel the independent modules, at every level. This is the parallel application. The second one is based on exploring several different structures simultaneously, by executing the same algorithm but with different parameters. That is the parametric application.

1) Parallel application

The idea here consists of creating for every computing stage of SCT a service. In fact, the whole simulation requires only three types of services, since M1, M2, ... M256 are based on the same computing function. M257, M258, M259, and M260 are based on another computing function. The cascade is the same at all levels. To run a SCT simulation, the services are called with the corresponding parameters. Each service produces its results which can be used by other services. To ensure the good execution of the SCT simulation, an adapted scheduler, knowing the level scales, organize the relation between the services.

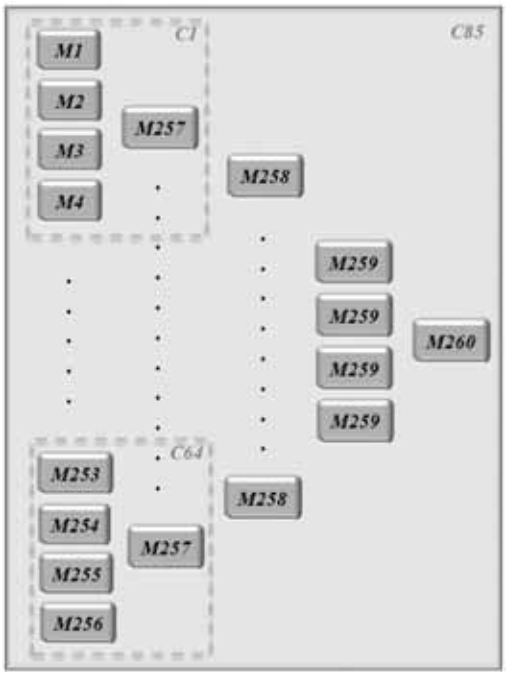

Fig. 7. SCT flowchart.

Fig. 8. Distributed parametric computing.

The services are created with the DIET tool [22], an application service provider (ASP) able to ensure the scalability of the solution on several thousand grid computing nodes if necessary. The deployment of the application on the grid is realized by TUNe [23], an efficient tool able to repair some parts of the deployment and execution (which is a critical point of the Grid).

2) Parametric application

The parametric execution (also known as embarrassingly parallel), involves execution of the same code with different input parameters, which do not request data transfer during executions. Some typical examples include frequency sweeps

for antenna characterization, or design of optimal antenna geometries.

In this case, a multiple frequency band analysis (the pass band and the stop band) is required. Normally, this case is not very suitable for frequency domain software since the pass band and the stop band are 2 to 3 octaves apart.

In distributed parametric SCT simulations, a wide range of design parameters are evaluated in a single analysis run with the goal of exploring the entire design space and selecting the optimized design without need for the normal iterative process (Figure 8). In our case, the idea is to modify the aperture length, and verify the corresponding transmission coefficient.

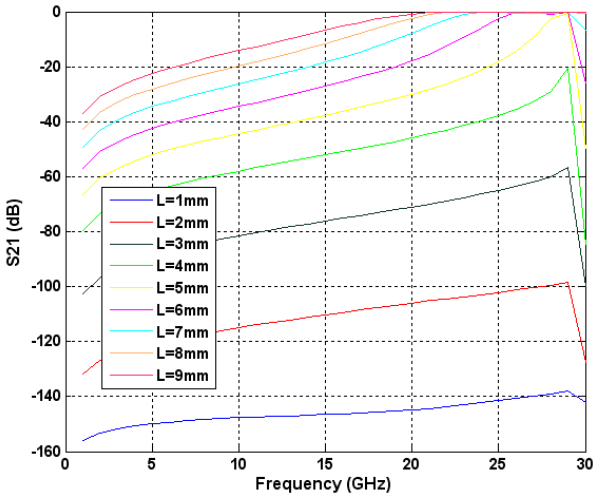

Fig. 9. Design dimension sweep of the aperture length L of 16 x 16-element uniform thick dichroïc plate.

C. Results

Figure 9 displays the simulated transmission coefficients of a uniform metallic grid (a = b= 10 mm) (Figure 1) with a thickness h=5mm in the case of a normal plane wave incidence for different aperture length L. In this figure only a few curves are presented.

Since the transmission we are looking for is in the range of frequency going from 20 GHz to 30 GHz, an aperture of 8.2 mm will give such performance. Increasing the aperture length L of the cells, which is related to the cutoff frequencies, increased the bandwidth.

Figure 10 displays the simulated reflection and transmission coefficients of a uniform metallic grid (Figure 1) with a thickness h = 5mm and an aperture of L = 8.2 mm in the case of a normal plane wave incidence. Ansoft HFSS [24] (version 11.2) was used for FEM implementation with 0.02 stopping criterion for the adaptive convergence solution. An excellent agreement between the HFSS- and SCT-results can be observed.

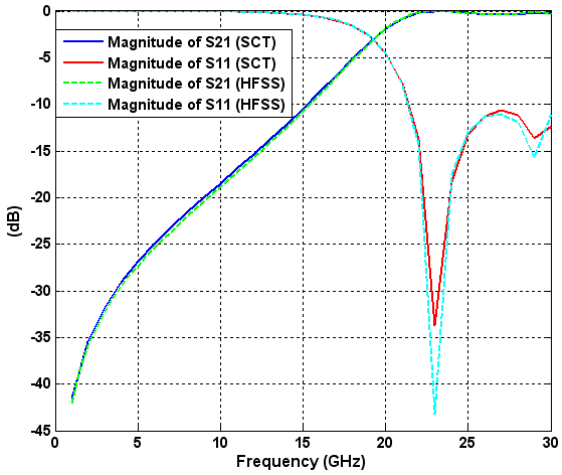

Fig. 10. S11 and S21 coefficients.

Figure 11 shows the radiation patterns in the case of a 16 x 16-element uniform thick dichroïc plate shown in Figure 1 simulated at a single point of frequency in the case of a normal plane wave incidence.

Figure 12 represents the simulation time evolution on the same computer for these two techniques calculating the transmission and reflection coefficient when the number N of cells increases.

For a given thick dichroïc plate and simulation technique, the computation time in this figure is normalized to the time required for calculating these coefficients in the case of a 4–cell array. For the scale changing technique computation, time increases very slowly as the number N of cells increases. Meanwhile, in the case of the finite element method, they increase dramatically, because of the mesh refinement needed to insure convergence.

As expected, for the parametric application, the overall execution time of the simulations depends on the number of nodes that are used, or more precisely, on the number of simulations that are executed on each node. A speed-up of ~ 2(compared to the time needed for the computation on one computer only) is reached by using two computers. Increasing the number of

computing nodes to solve the problem increases the speed-up. Speedup up to 10 or more could be easily reached by distributing the simulations on less than one hundred computers.

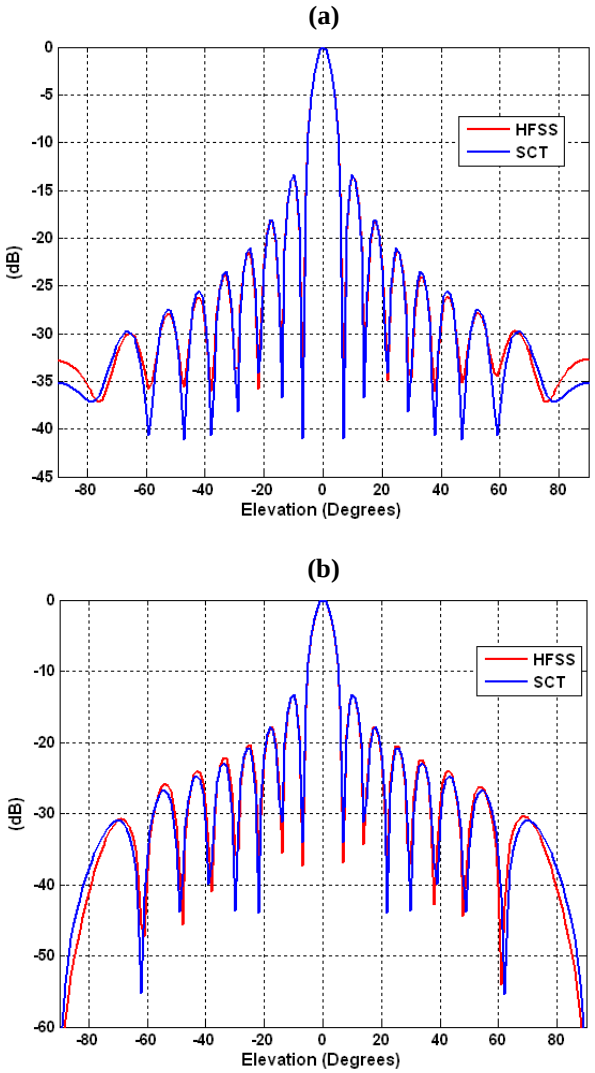

Fig. 11. Co-polarization in (a) E-plane, and (b) H-plane @ 15 GHz.

Users must choose in advance the number of grid nodes reserved in order to accommodate heavier or lighter electromagnetic simulation requests. The best performance is obtained while distributing the simulations in a way to execute one simulation per computing node. These results point out the benefit from using a large number of computational nodes for running SCT simulations.

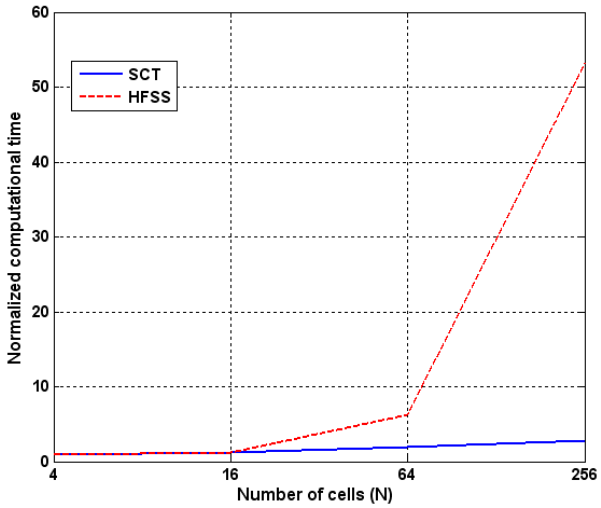

Fig. 12. Evolution of computing time compared to the standard time for the calculation of two cells of uniform arrays on the same computer.

V. CONCLUSION

Two efficient solutions contributing to the electromagnetic modeling and design of a thick dichroïc plate have been presented in this paper.

First, the scale changing technique modeling method, a well-adapted method for the problems of complex multi-scale structures and which demonstrated very good computing performance even in sequential on one computer, compared to existing commercial codes.

Second, the use of grid computing to solve electromagnetic problems was presented in an example of distributed parametric simulation of thick dichroïc plates. A wide range of design parameters are evaluated in a single analysis run with the goal of satisfying to predefined technical requirements of transmission and reflection coefficients in X and Ka frequency bands. Regardless of the number of possible parametric configurations antenna elements may have, their full-wave analysis can be carried out at the computational costs of a single one, by distributing them over a corresponding number of nodes.

Consequently, the approach consisting of combining the advantages of the scale changing technique and grid computing is so promising.

ACKNOWLEDGMENT

Experiments presented in this paper were carried out using the Grid'5000 experimental test bed, being developed under the INRIA ALADDIN

development action with support from CNRS, RENATER and several Universities as well as other funding bodies (see https://www.grid5000.fr). Part of this work has been supported by Thales Alenia Space, Toulouse and the French Space Agency (CNES).

REFERENCES

[1] N. Farahat and R. Mittra, "Multiscale Analysis of Panel Gaps in a Large Parabolic Reflector," Applied Computational Electromagnetics Society (ACES) Journal, vol. 21, no. 1, March 2006.

[2] R. Mittra, J.-F. Ma, E. Lucente, and A. Monorhio, "CBMOM - An iteration free MoM approach for solving large multiscale EM radiation and scattering problems," IEEE Antennas and Propagation Society International Symposium, vol. 2B, 2-5, Washington, D.C., Jul. 3-8, 2005.

[3] H. Aubert, "The Concept of Scale-Changing Network in the Global Electromagnetic Simulation of Complex Structures," *PIER B*, vol. 16, pp. 127-154, 2009.

[4] E. B. Tchikaya, A. Rashid, F. Khalil, H. Aubert, H. Legay, and N. J.G. Fonseca, "Multi-scale Approach for the Electromagnetic Modeling of Metallic FSS Grids of Finite Thickness with Non-uniform Cells," *2009 Asia-Pacific Microwave Conference* (APMC 2009), Singapore, December 7-10, 2009.

[5] L. Tarricone and A. Esposito: *Grid Computing For Electromagnetics*. Artech House Publishers (2004).

[6] I. Foster, "What is the Grid? A Three Point Checklist," *GRIDtoday*, vol. 1, no. 6, July 22, 2002.

[7] B. A. Munk, *Frequency Selective Surfaces: Theory and Design*, First Edition, Wiley, New York, 2000.

[8] W. L. Ko and R. Mittra "Implementation of Floquet boundary condition in FDTE for FSS analysis," in *1993 IEEE APS, Int. Symp. Dig.*, vol. 1, pp. 14-1, June 28-July 2.

[9] T. Koleck, H. Diez, and J.C. Bolomey, "Technique for analyzing Finite Frequency Selective Surfaces," *IEEE international conference on Antennas and propagation*, Digest, 14-17, April 1997.

[10] R. Mittra, C.H. Chan, and T. Cwilk, 1998, "Techniques for analysing Frequency Selectives Surfaces-A review," *Proc. Of the IEEE*, vol. 76, 1593-1614, Dec. 88.

[11] E. Perret, H. Aubert, and H. Legay, "Scale-Changing technique for the electromagnetic modeling of MEMS-controlled planar phase-shifters," *IEEE Trans. Microwave Theory and Tech.*, vol. 54, no. 9, 3594-3601, Sep. 2006.

[12] E. Perret, N. Raveu, H. Aubert, and H. Legay, "Scale-Changing technique for MEMS-controlled phase-shifters," *36th European Microwave Week*, 866-869, Manchester, United Kingdom, Sep. 10-15, 2006.

[13] D. Voyer, H. Aubert, and J. David, "Scale-changing technique for the electromagnetic modeling of planar self-similar structures," *IEEE Trans. Antennas Propagat.*, vol. 54, no. 10, 2783-2789, Oct. 2006.

[14] D. Voyer, H. Aubert, and J. David, "Radar cross section of discrete self-similar objects using a recursive electromagnetic analysis," IEEE Antennas and Propagation Society International Symposium, vol. 4, 4260-4263, Monterey, California, USA, Jun. 20-26, 2004.

[15] D. Voyer, H. Aubert, and J. David, "Radar cross section of self-similar targets," Electronics Letters, vol. 41, no. 4, 215-217, Feb. 17, 2005.

[16] E. Perret, and H. Aubert, "Scale-Changing technique for the computation of the input impedance of active patch antennas," IEEE Antennas and Wireless Propagation Letters, vol. 4, 326-328, 2005.

[17] E. Perret, and H. Aubert, "A multi-scale technique for the electromagnetic modeling of active antennas," IEEE Antennas and Propagation Society International Symposium, vol. 4, 3923-3926, Monterey, California, USA, Jun. 20-25, 2004.

[18] N. Raveu, G. Prigent, H. Aubert, P. Pons, and H. Legay, "Scale-Changing technique design and optimisation tool for active reflect-arrays cell," 37th European Microwave Conference, 736-739, München, Germany, Oct. 9-12, 2007.

[19] Nathalie Raveu, E. Perret, Hervé Aubert, and H. Legay, "Design of MEMS controlled phase shifter using SCT," PIERS Online, vol. 3, no. 2, 230-232, Beijing, China, Mar. 26-30, 2007.

[20] N. Raveu, E. Perret, H. Aubert, and H. Legay, "Scale-changing technique: A design tool for reflectarrays active cells," Proceedings of the European Microwave Association, vol. 4, no. 2, 163-168, Journal of the European Microwave Association, Jun. 2008.

[21] R. F. Harrington, Time-Harmonic Electromagnetic Fields. NewYork: McGraw-Hill, 1961, pp.106-118.

[22] E. Caron and F. Desprez, "DIET: A scalable toolbox to build network enabled servers on the grid," International Journal of High Performance Computing Applications, 20(3):335–352, 2006.

[23] L. Broto, D. Hagimont, P. Stolf, N. Depalma, and S. Temate, "Autonomic management policy specification in Tune," Annual ACM Symposium on Applied Computing (SAC 2008), Fortaleza, Ceará, Brazil, ACM, pp. 1658-1663, 16-20 March 2008.

[24] Ansoft HFSS Homepage. Copyright Ansys 2010. http://www.ansoft.com/products/hf/hfss/

Fadi Khalil was born in Beirut, Lebanon, in March 1983. He received his B.S. degree in Electrical Engineering from the Lebanese University, Lebanon in 2005, and the M.S. degree in Modeling, Information and Systems, in 2006 from Toulouse University, France.

From November 2006 to November 2009, Fadi was working toward the Ph.D. degree in Micro- and Nano-systems for Wireless Communications Research Group at the Laboratory of Analysis and Architecture of Systems (LAAS-CNRS) in Toulouse, France. His research interests include computational electromagnetics, modeling of complex (multi-scale) structures and reconfigurable circuits for RF and microwave applications, high performance computing, and wireless sensors networks. Author is affiliated with the ACES applied society, IEEE MTT (microwave theory and techniques) Society and the IEEE AP (antennas and propagation).

Euloge B. Tchikaya was born in Pointe-Noire, Congo. He received his B.S. degree in Electrical Engineering from the University of Rennes, France in 2005, and the M.S. degree in Electrical Engineering, in 2007 from University of Rennes, France. He is currently working toward the Ph.D. in Micro- and Nano-systems for wireless Communications Research Group at the Laboratory of Analysis and Architecture of Systems (LAAS-CNRS) in Toulouse, France. His research interests include frequency selective surfaces, computational electromagnetics, modeling of complex (multi-scale) structures and reconfigurable circuits for RF and microwave applications.

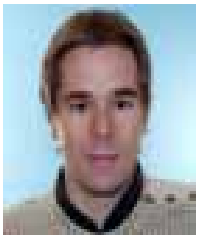

Rémi Sharrock holds a Certified Engineering degree in Networks and Telecommunications from INSA Toulouse. He obtained his M.S. in 2007 from the National Polytechnic Institute of Toulouse. He is now a Ph.D. student in grid computing and applications.

Thierry Monteil is Assistant Professor in Computer Science at INSA of Toulouse and researcher at LAAS-CNRS. He has a Doctorate in Parallel Computing and the Certified Engineer Degree in Computer Science and Applied Mathematics. He works on parallel computing (LANDA parallel environment), grid resources management (AROMA project), computer and network modeling, autonomous policies to improve performance on distributed applications, and parallelization of large electromagnetic simulation. He has managed a SUN center of excellence in the field of grid and cluster for network applications and a Cisco academy.

Fabio Coccetti received the Laurea (M.S.) degree in Electrical Engineering from the University of Perugia, Perugia, Italy, and the Ph.D. title in High-Frequency Engineering at the Lehrstuhl fur Hochfrequenztechnik at the Technische UniversitatMunchen (TUM) in Munich, Germany, in 1999 and 2004, respectively. In 2000, he spent 7 months as Visiting Scientist at the Radiation Lab at University of Michigan, U.S.A. During the period 2001–2002, he joined a number of design and fabrication projects with German companies (BOSCH, Siemens, Rohde & Schwarz) and the European Space Agency (ESA) in the area of micro-electro-mechanical Systems (RF-MEMS) based circuits. Since September 2004, he is working as Research Scientist at the Laboratoire d'Analyse et d'Architectures des Systèmes at the Centre National de la Recherche Scientifique (LAAS-CNRS) in Toulouse, France. During this period, he has worked on numerous research projects going from the theoretical and experimental investigation of power handling in RF-MEMS to design modelling and experimental validation of RF Microsystems. During 2004–2007, he has been the Administrative Coordinator of the European Network of Excellence on RF-MEMS and RF Microsystems (AMICOM NoE) and member of the ARRRO consortium, a specific support action aiming at defining the RF-MEMS and RF-NEMS technology roadmap up to 2020 (both projects were funded by the European Commission under the 6th Framework Program). His research interests include numerical techniques optimization, multiphysics (concurrent electrical and thermomechanical), and reliability analysis of RF-MEMS components, design and modelling of reconfigurable circuits for microwave and millimeter applications. Dr. Coccetti is a member of the IEEE society, of the European Microwave Association (EUMA) and one of the five co-founders of the European Forum of Experts on RF-MEMS and RF-MST.

Hervé Aubert was born in Toulouse, France, in July 1966. He received the Eng. Dipl. in July 1989 and the Ph.D. degree (with high-honors) in January 1993, both in Electrical Engineering and both from the "Institut National Polytechnique" (INPT), Toulouse, France. Since February 2001, Hervé Aubert is Professor at INPT. He has joined the "Laboratoire d'Analyse et d'Architecture des Systèmes," National Center for Scientific Research, Toulouse, in February 2006. From April 1997 to March 1998, he was a Visiting Associate Professor at the School of Engineering and Applied Science, University of Pennsylvania, Philadelphia, USA. Dr. Aubert is a contributor to the books Fractals: Theory and Applications in Engineering (Springer, 1999), Micromachined Microwave Devices and Circuits (Romanian Academy Edition, 2002) and New Trends and Concepts in Microwave Theory and Techniques (Research Signpost, 2003). He has authored or co-authored one book, 44 papers in refereed journals and over 120 communications in International Symposium Proceedings. He holds 4 international patents in the area of antennas. Dr. Aubert is the Secretary of "IEEE Antennas and Propagation French Chapter" and was the Vice-Chairman of this Chapter from 2004 to 2009 and Secretary from 2001 to 2004. Dr. Aubert is a senior member of IEEE (1999) and a member of URSI commission B.

Preconditioned MDA-SVD-MLFMA for Analysis of Multi-Scale Problems

Z. N. Jiang, Z. H. Fan, D. Z. Ding, R. S. Chen, and K. W. Leung

Department of Communication Engineering
Nanjing University of Science and Technology, Nanjing, China, 210094
eechenrs@mail.njust.edu.cn

***Abstract*-** Multilevel fast multipole algorithm (MLFMA) has been widely used to solve electromagnetic scattering problems from the electrically large size objects. However, it consumes very large memory to store near the interaction matrix for the object with fine structures because the "low frequency breakdown" phenomenon would happen when the finest level box's size is below 0.2 wavelengths. The matrix decomposition algorithm - singular value decomposition (MDA-SVD) is one remedy to alleviate this pressure because it has no limit of the box's size. However, the matrix assembly time of MDA-SVD is much longer than that of the MLFMA. In this paper, a hybrid method called MDA-SVD-MLFMA is proposed to analyze multi-scale problems, which uses the main framework of MLFMA but adopts the MDA-SVD to deal with the near interaction of MLFMA. This method takes advantage of the virtues of both MLFMA and MDA-SVD and is more efficient than either conventional MLFMA or conventional MDA-SVD. An efficient preconditioning technique is combined into the inner-outer flexible generalized minimal residual (FGMRES) solver to speed up the convergence rate. Numerical results are presented to demonstrate the accuracy and efficiency of the proposed method.

***Index Terms*-** Flexible generalized minimal residual (FGMRES), matrix decomposition algorithm - singular value decomposition (MDA-SVD), multilevel fast multipole algorithm (MLFMA).

I. INTRODUCTION

In electromagnetic wave scattering calculations, a classical problem is to compute the equivalent surface currents induced by a given incident plane wave. Such calculations, relying on the Maxwell equations, are required in the simulation of many industrial processes ranging from antenna design, electromagnetic compatibility, computation of back-scattered fields, and so on. All these simulations require fast and efficient numerical methods to compute an approximate solution of Maxwell's equations. The method of moments (MoM) [1-2] is one of the most widely used techniques for electromagnetic problems. It is basically impractical to analyze electrically large problems using MoM because its memory requirement and computational complexity both are $O(N^2)$, where N refers to the number of unknowns. Recently, a wide range of fast methods have been developed for accelerating the iterative solution of the electromagnetic integral equations discretized by MoM. One of the most popular techniques is MLFMA [3-6], which has $O(N\log N)$ complexity for a given accuracy.

The increased power and availability of

1054-4887 © 2010 ACES

computational resources and acceleration schemes have enabled the solution of problems with a very large number of unknowns, varying from a few thousands to a few millions [3-6]. Another class of problems arises when analyzing structures which require a high local density of unknowns to accurately capture geometric features. This class of problems is referred to as multi-scale problems exhibit multiple scales in length. For example, small length scale discretizations are required to capture sharp or fine geometric features that are embedded within large and smooth geometries discretized at a coarser length scale. Generally, the characteristic of a multi-scale problem is the concentration of large number of unknowns in electrically small domains. However, when the finest level box's size is below 0.2 λ (λ indicates the incident wavelength), MLFMA will suffer from the "low frequency breakdown" phenomenon [4].

MDA-SVD is another popular technique used to analyze the scattering/radiation [7-8], which has no limit of the box's size. However, the matrix assembly time of MDA-SVD is much larger than that of MLFMA. In this paper, a hybrid method called MDA-SVD-MLFMA is proposed, which uses the main framework of MLFMA but adopts the MDA-SVD to deal with the near interaction of MLFMA. This method takes advantage of both MLFMA and MDA-SVD and is more efficient than either conventional MLFMA or conventional MDA-SVD for analyzing the multi-scale problems.

It is well known that the matrix condition number of the electric field integral equation (EFIE) for an electrically large problem is large. Furthermore, for multi-scale problems, the matrix condition number is even larger due to the mixed discretization. Therefore, the system has poor convergence history and requires urgently a good solver or preconditioner. In this paper, an efficient preconditioning technique is combined into the inner-outer flexible generalized minimal residual (FGMRES) solver to improve the property of EFIE [9-12].

The remainder of this paper is organized as follows. Section II demonstrates the formulation of EFIE and the theory of MDA-SVD briefly. Section III describes the theory and implementation of MDA-SVD-MLFMA in more details and gives a brief introduction to the inner-outer flexible generalized minimal residual (FGMRES) method. Numerical experiments are presented to demonstrate the efficiency of this proposed method in Section IV. Conclusions are provided in Section V comments.

II. THE THEORY OF MDA-SVD

A. The formulation of EFIE

In this paper, the electric field integral equation (EFIE) is used to analyze electromagnetic scattering problems. The EFIE formulation of electromagnetic wave scattering problems using planar Rao-Wilton-Glisson (RWG) basis functions for surface modeling is presented in [2]. The resulting linear systems from EFIE formulation after Galerkin's testing are briefly outlined as follows

$$\sum_{n=1}^{N} Z_{mn} I_n = V_m, \qquad \mathrm{m} = 1, 2, ..., N \tag{1}$$

where

$$\begin{aligned} Z_{mn} = \frac{jk}{4\pi}\Big(\iint_s \Lambda_m(\mathbf{r}) \cdot \iint_s G(\mathbf{r},\mathbf{r}')\Lambda_n(\mathbf{r}')dS'dS \\ -\frac{1}{k^2}\iint_s \nabla\cdot\Lambda_m(\mathbf{r}) \cdot \iint_s G(\mathbf{r},\mathbf{r}')\nabla\cdot\Lambda_n(\mathbf{r}')dS'dS\Big) \end{aligned} \tag{2}$$

and

$$V_m = \iint_s \Lambda_m(\mathbf{r}) \cdot \left(\frac{1}{\eta}\mathbf{E}^i(\mathbf{r})\right) dS \text{ ,}$$

$$G(\mathbf{r},\mathbf{r}') = \frac{e^{-jk|\mathbf{r}-\mathbf{r}'|}}{|\mathbf{r}-\mathbf{r}'|}$$

Here, $G(\mathbf{r},\mathbf{r}')$ refers to the Green's function in free space and $\{I_n\}$ is the column vector containing the unknown coefficients of the surface current expansion with RWG basis functions. Also, as usual, $\mathbf{r}$ and $\mathbf{r}'$ denote the observation and source point locations. $\boldsymbol{E}^i(\mathbf{r})$ is the incident excitation plane wave, and η and k denote the free space impedance and wave number, respectively. N is the number of unknowns used to discretize the object.

Once the matrix equation (1) is solved, the expansion coefficients $\{I_n\}$ can be used to calculate the scattered field and RCS. In the following, we use Z to denote the coefficient matrix in equation (1), $I = \{I_n\}$ and $V = \{V_n\}$ for simplicity. Then, the EFIE matrix equation (1) can be symbolically rewritten as

$$ZI = V \tag{3}$$

To solve the above matrix equation by an iterative method, the matrix-vector products are needed at each iteration. Traditionally, a matrix-vector production requires the operation cost $O(N^2)$.

B. The theory of MDA-SVD

The multilevel matrix decomposition algorithm (MLMDA) was originally proposed for two-dimensional geometries in [13], which utilizes the idea of equivalent point sources. The extension of this algorithm is presented in [14-19] for analyzing arbitrary three-dimensional geometries. However, it is efficient only for planar or piecewise planar objects and is inefficient for analyzing the general electrically large scatterer. MDA-SVD presented in [7-8] shows a better efficiency by recompressing the matrix of MDA using the SVD technique.

Consider, there exists two subdomains, the first one is an observation box i that contains m_1 basis functions; whereas, the second one is a source box j that contains m_2 test functions. When the two boxes are sufficiently separated, the impedance matrix associated with them can be expressed using low rank representations [20]. In MDA implementation, the impedance matrix which is gotten through the EFIE of two well-separated regions can be expressed as three small matrices

$$[Z_{mn}] = [U_{mr}][\omega_{rr}]^{-1}[V_{rn}] \tag{4}$$

where $[Z_{m\ n}]$ is the interaction matrix between observation and source subdomains, r denotes the number of equivalent RWG sources, which is much smaller than n and m. Therefore, the matrix-vector product operation of the three matrices is much smaller than the operation of the direct multiplication [16].

Since the matrices $[U_{mr}]$ and $[V_{rn}]$ generated by MDA are usually not orthogonal, they may contain redundancies, which can be removed by the following algebraic recompression technique. This method may be regarded as the singular value decomposition optimized for rank-k matrices. Utilize QR and SVD to reorthonormalize $[U_{mr}]$ and $[V_{rn}]$ and the equation (4) can be obtained as

$$[Z_{mn}] = [U][\omega][V]^T \tag{5}$$

where $[U]$ and $[V]$ are both orthogonal. These techniques can reduce the required amount of storage of MDA, while the asymptotic complexity of the approximation remains the same.

MDA-SVD is one of the most popular methods for analyzing three-dimensional electromagnetic problems, but the far-field matrix assembly time of MDA-SVD is much longer than that of MLFMA. In order to reduce the matrix assembly time of MDA-SVD, a new hybrid method is proposed in the following.

III. FORMULATION

According to [3-6], MLFMA has been widely used to solve the scattering from the electrically-large size objects. When it is applied

into analyzing the scattering from the multi-scale objects where dense discretization is necessary to capture geometric features accurately, the memory usage of MLFMA is very large. MDA-SVD is another popular technique for solving the three dimensional problems in [7-8], but the far-field matrix assembly time of MDA-SVD is much longer than that of MLFMA. In this section, a hybrid method called MDA-SVD-MLFMA is proposed.

Take three dimensional problems into account, both MLFMA and MDA-SVD are based on the data structure of the octree. In Fig.1, the box enclosing the object is subdivided into smaller boxes at multiple levels, in the form of an octal tree. The largest boxes not touching each other are at level 2, while the smallest boxes are at level *L*. The subdivision process runs recursively until the finest level *L*.

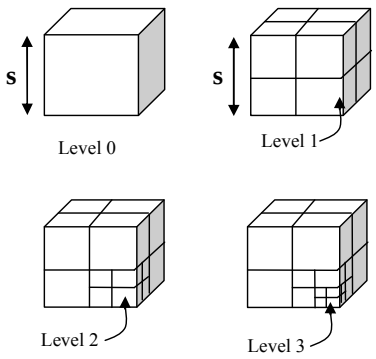

Fig. 1. The sketch of the octree structure.

It is well known that when the box size is less than 0.2 λ, MLFMA will suffer from the "low frequency breakdown" phenomenon. The relative error of MLFMA and MDA-SVD corresponding to the size of the finest level box is analyzed. The formulation of the relative error is described by

$$\text{Relative error} = \|T - M\| / \|M\|,$$

where *M* denotes the bistatic scattering from PEC sphere computed by Mie series while *T* is the bistatic scattering computed by MLFMA or MDA-SVD. The incident direction is $\theta_i = 0^\circ, \phi_i = 0^\circ$ and the scattered angles vary from 0° to 180° in azimuth direction when pitch angle is fixed at 0°. The number of unknowns is 15918 and the MDA-SVD truncating tolerance is 10^{-3} relative to the largest singular value. Figure 2 shows the relative error of MLFMA will increase greatly when the size of the finest level box is less than 0.2 λ. It can be seen that MDA-SVD has an acceptable precision even when the finest level box size is below 0.2 λ.

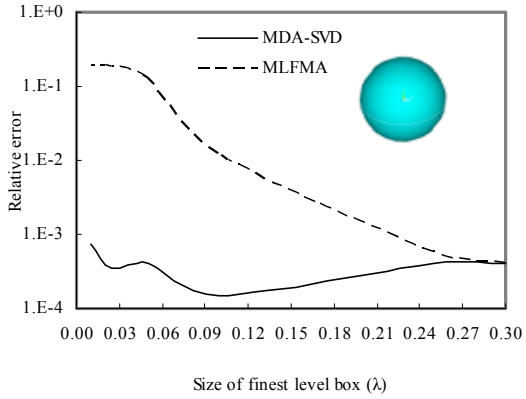

Fig. 2. Relative error of MLFMA and MDA-SVD for a sphere corresponding to the size of finest level box for bistatic scattering.

When the multi-scale problems are analyzed, MDA-SVD is adopted for the level with the box size smaller than 0.2 λ while MLFMA is adopted for other cases. The details of the hybrid method are shown in algorithm I.

Algorithm I: MDA-SVD-MLFMA

1) Grouping on the target to achieve multilevel structures with the largest level *L*. When the number of basis functions of the box is less

than or equal to the number of equivalent RWG sources of the box, the finest level L is gained. At each level, the sizes of the boxes are same.

2) For each level, determine which algorithm is applied according to the box size. MDA-SVD is adopted for the level with the box size smaller than 0.2 λ while MLFMA is adopted for other cases. L_{MLFMA} is the level beginning of the MLFMA.

3) Calculation of the impedance matrix

   a) MoM is used to calculate the near interaction impedance matrix.

   b) From $l = L : L_{\mathrm{MLFMA}}+1$

   MDA-SVD is applied to calculate the impedance matrix

   End

   c) From $l = L_{\mathrm{MLFMA}}: 2$

   MLFMA is used to calculate the impedance matrix

   End

4) Iterative solution of the matrix equation

   d) The direct matrix-vector production is used to the near interaction impedance matrix.

   e) From $l = L : L_{\mathrm{MLFMA}}+1$

   MDA-SVD is applied to speed up matrix-vector production

   End

   f) From $l = L_{\mathrm{MLFMA}}: 2$

   MLFMA is used to speed up matrix-vector production

   End

This new method takes advantages of the virtues of both MLFMA and MDA-SVD, which uses MLFMA to reduce the matrix assembly time of MDA-SVD and utilizes MDA-SVD to alleviate the near field burden of MLFMA. The efficiency of the method is demonstrated by the numerical results.

In this paper, the FGMRES is used as the iterative solver for the EFIE to further accelerate the convergence [9-12]. Consider the iterative solution of equations of the form $Ax=b$. The GMRES algorithm with right preconditioning solves the modified system $AM^{-1}(Mx)=b$, where the preconditioner M is constant. However, in FGMRES, the preconditioner is allowed to vary from one step to another in the outer iteration. We have GMRES for the inner iterations whose preconditioner is chosen as the near interaction of MDA-SVD-MLFMA.

IV. NUMERICAL RESULTS

To validate and demonstrate the accuracy and efficiency of the proposed MDA-SVD-MLFMA, some numerical results are presented in this section. All the computations are carried out on a personal computer with 1.86 GHz CPU and 1.96GB RAM in single precision and the MDA-SVD truncating tolerance is 10^{-3} relative to the largest singular value. The restart number of GMRES is set to be 30 and the stop precision for restarted GMRES is denoted to be 10^{-3}. Both the inner and outer restart numbers of FGMRES are 30. The stop precision for the inner and outer iteration in the FGMRES algorithm is 10^{-2} and 10^{-3}, respectively. The normalized RCS is defined as

$$\frac{RCS(\theta,\phi)}{\lambda^2}=\frac{1}{\pi}\lim_{r\to\infty}\left\{(kr)^2\frac{\left|E^s(r,\theta,\phi)\right|^2}{\left|E^i(r,\theta,\phi)\right|^2}\right\}, \qquad (6)$$

for any direction (θ,ϕ), where E^s and E^i represent the scattered and incident electric fields.

A. The plane-cylinder geometry

The multi-scale examples are analyzed in the following. The first multi-scale example is plane-cylinder geometry. The edge length of the square plane is 4 m, the radius of the small column is 0.1 m, and the height of small column is

2 m. The rotation axis is z-axis. Here, the small column is densely discretized in comparison to the plane part of the structure. The incident and observed angles are ($\theta_i = 0^\circ, \phi_i = 0^\circ$) and ($0^\circ \le \phi_s \le 180^\circ, \theta_s = 90^\circ$), respectively. The size of the lowest-level box of the MDA-SVD-MLFMA is 0.16 λ , while the size of the lowest-level box of the MLFMA is 0.33 λ . Figure 3(a) shows that the result of MDA-SVD-MLFMA agrees very well with the FEKO [21].

Table 1 summarizes the matrix assembly time and the memory storages of the MDA-SVD-MLFMA, MDA-SVD, and MLFMA. "MVP time" in the table indicates the time of one matrix-vector production. It can be observed that the matrix assembly time of the MDA-SVD-MLFMA is half less than that of MDA-SVD and is, also, less than that of MLFMA. The total memory consumption of MDA-SVD-MLFMA is half less than that of MLFMA and is less than that of MDA-SVD. The MVP time of MDA-SVD-MLFMA is, also, much less than that of either MLFMA or MDA-SVD.

Figure 3(b) gives the convergence history curves of MDA-SVD-MLFMA solved with GMRES and FGMRES. In this numerical experiment, GMRES requires 6190 s with 5896 iterative steps, while FGMRES requires only 667 s with 46 outer iterative steps. The solving time of GMRES is 9 times longer than that of FGMRES in this example.

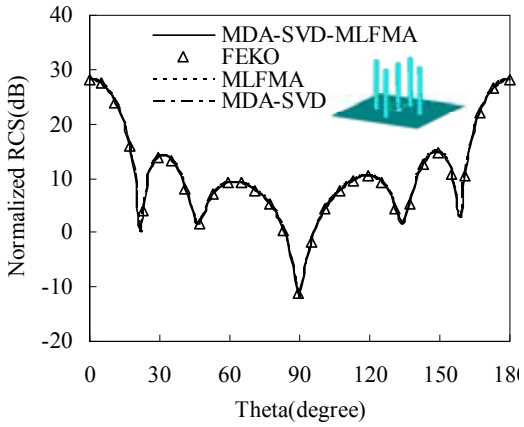

(a)

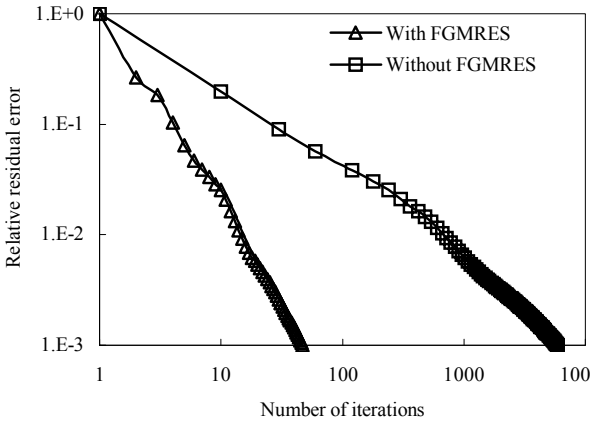

(b)

Fig. 3. (a) Bistatic scattering cross section of plane-cylinder geometry. (b) Convergence histories of MDA-SVD-MLFMA solved with GMRES and FGMRES.

Table 1: The total memory, the matrix assembly time, and one matrix-vector multiplication time of MLFMA, MDA-SVD, and MDA-SVD-MLFMA of plane-cylinder geometry

Frequency (MHz)	Unknowns	Algorithms	Matrix assembly time (s)	Memory (MB)	MVP time (s)
200	28756	MDA-SVD-MLFMA	400	458	1.05
		MDA-SVD	1101	666	1.53
		MLFMA	415	968	1.70

B. The missile geometry

The second multi-scale example is missile geometry. The height of the cylinder is 4.7 m, and the radius of the cylinder is 0.5 m. The rotation axis of missile geometry is *z*-axis. The incident and scattered angles are ($\theta_i = 0^\circ, \phi_i = 0^\circ$) and ($0^\circ \le \phi_s \le 180^\circ, \theta_s = 90^\circ$), respectively. The size of the lowest-level box of the MDA-SVD-MLFMA is 0.14 λ , while the size of the lowest-level box of MLFMA is 0.29 λ . Table 2 shows the matrix assembly time, the memory storages, and MVP time of MDA-SVD-MLFMA, MDA-SVD, and MLFMA. Again, the matrix assembly time of MDA-SVD-MLFMA is half less than that of MDA-SVD and is, also, less than that of MLFMA. The memory usage of MDA-SVD-MLFMA is half less than that of MLFMA and is less than that of MDA-SVD. The MVP time of MDA-SVD-MLFMA is also much less than that of MLFMA and MDA-SVD. The bistatic RCS by use of MDA-SVD-MLFMA is shown in Fig. 4(a), and is agreed well with FEKO. The convergence curves are plotted for MDA-SVD-MLFMA solved with GMRES and FGMRES in Fig. 4(b). GMRES requires 7964 s with 4958 iterative steps, while FGMRES requires only 1095 s with 65 outer iterative steps. The solving time of GMRES is 7 times longer than that of FGMRES, in this example.

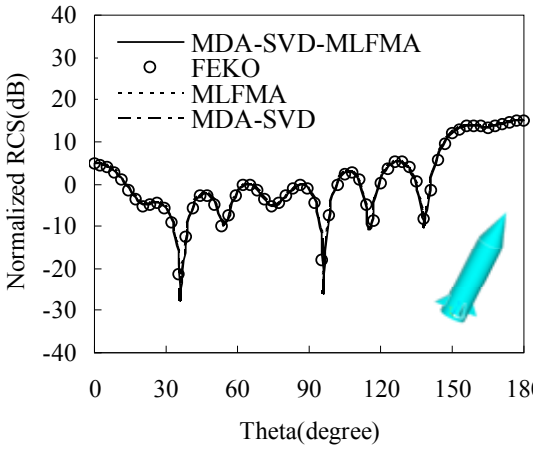

(a)

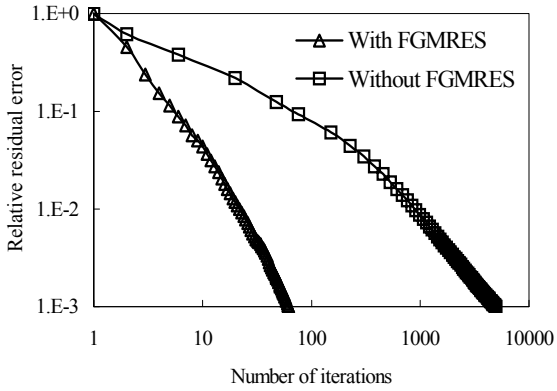

(b)

Fig. 4. (a) Bistatic scattering cross section of missile geometry. (b) Convergence histories of MDA-SVD-MLFMA solved with GMRES and FGMRES.

Table 2: The total memory, the matrix assembly time, and one matrix-vector multiplication time of MLFMA, MDA-SVD, and MDA-SVD-MLFMA of missile geometry

Frequency (MHz)	Unknowns	Algorithms	Matrix assembly time (s)	Memory (MB)	MVP time (s)
300	38145	MDA-SVD-MLFMA	600	638	1.60
		MDA-SVD	1757	949	2.01
		MLFMA	643	1272	2.22

C. The VIAS geometry

The third multi-scale example is the VIAS geometry [22]. The geometry fits within a cuboid with aspect radio $6:5:0.5$ and the maximum dimension is 6λ at 300 MHz. The incident and scattered angles are ($\theta_i = 0^\circ, \phi_i = 0^\circ$) and ($0^\circ \le \phi_s \le 180^\circ, \theta_s = 90^\circ$), respectively. The size of the lowest-level box of the MDA-SVD-MLFMA is 0.18 λ , while the size of the lowest-level box of MLFMA is 0.37 λ . The matrix assembly time, the memory storages and MVP time of MDA-SVD-MLFMA, MDA-SVD, and MLFMA are shown in Tab. 3. The matrix assembly time of MDA-SVD-MLFMA is much less than that of MDA-SVD and is, also, less than that of MLFMA, while the memory usage of MDA-SVD-MLFMA is much less than that of MLFMA and is less than that of MDA-SVD. The bistatic RCS by use of MDA-SVD-MLFMA is shown in Fig. 5(a), and is agreed well with that of MLFMA and MDA-SVD. The convergence curves are plotted for MDA-SVD-MLFMA solved with GMRES and FGMRES in Fig. 5(b). GMRES requires 2403 s with 1190 iterative steps, while FGMRES requires only 411 s with 84 outer iterative steps. The solving time of GMRES is 5 times longer than that of FGMRES in this example.

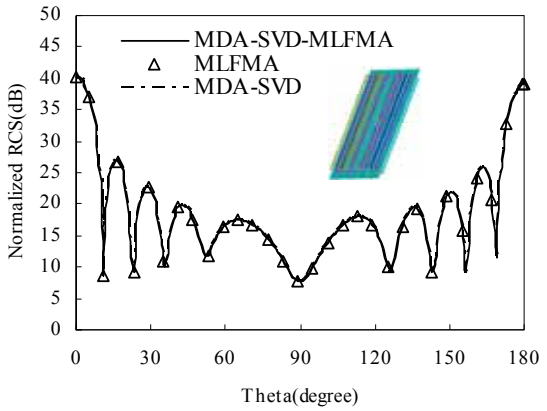

(a)

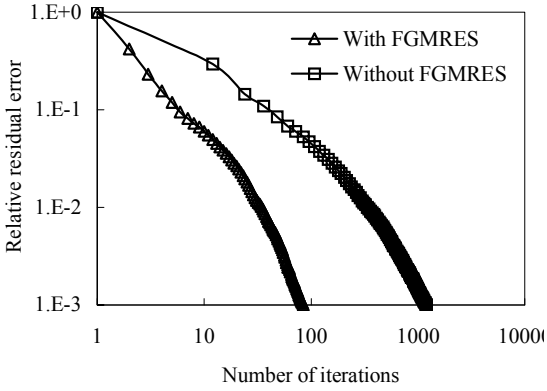

(b)

Fig. 5. (a) Bistatic scattering cross section of VIAS geometry. (b) Convergence histories of MDA-SVD-MLFMA solved with GMRES and FGMRES.

Table 3: The total memory, the matrix assembly time, and one matrix-vector multiplication time of MLFMA, MDA-SVD, and MDA-SVD-MLFMA of VIAS geometry

Frequency (MHz)	Unknowns	Algorithms	Matrix assembly time (s)	Memory (MB)	MVP time (s)
300	61099	MDA-SVD-MLFMA	811	661	2.02
		MDA-SVD	2631	922	2.43
		MLFMA	827	1284	2.90

In summary, the memory of MDA-SVD-MLFMA is much less than that of MLFMA and the matrix assembly time of MDA-SVD-MLFMA is much less than that of MDA-SVD. The matrix-vector multiplication of MDA-SVD-MLFMA is more efficient than that of either MLFMA or MDA-SVD. It can be applied to the monostatic RCS calculation of the complex object in future. The MDA-SVD-MLFMA is much more efficient than either MLFMA or MDA-SVD for the multi-scale problems. It is observed that the convergence rate of GMRES is remarkably accelerated by the application of FGMRES algorithm.

V. CONCLUSIONS

In this paper, a new efficient hybrid method named MDA-SVD-MLFMA is proposed. The MDA-SVD-MLFMA takes advantage of the virtues of both MLFMA and MDA-SVD, which uses MLFMA to reduce the matrix assembly time of MDA-SVD and utilizes MDA-SVD to alleviate the near field burden of MLFMA. The numerical results demonstrate that the memory of MDA-SVD-MLFMA is much less than that of MLFMA and the matrix assembly time of MDA-SVD-MLFMA is much less than that of MDA-SVD. It is observed that the convergence rate of GMRES is remarkably accelerated by the application of FGMRES algorithm. MDA-SVD-MLFMA combined with FGMRES is very efficient for analyzing the multi-scale problems.

ACKNOWLEDGMENT

We would like to thank the support of Major State Basic Research Development Program of China (973 Program: 2009CB320201); Natural Science Foundation of 60871013, 60701004, 60928002; Jiangsu Natural Science Foundation of BK2008048.

REFERENCES

[1] R. F. Harrington, *Field Computations by Moment Methods*, MacMillan, New York, 1968.

[2] S. M. Rao, D. R. Wilton, and A. W. Glisson, ‘‘Electromagnetic Scattering by Surfaces of Arbitrary Shape,’’ *IEEE Trans. Antennas Propagat.*, vol. AP-30, pp. 409-418, May 1982.

[3] R. Coifman, V. Rokhlin, and S.Wandzura, “The fast multipole method for the wave equation: A pedestrian prescription,” *IEEE Antennas Propag. Mag.*, vol. 35, no. 6, pp. 7-12, Jun. 1993.

[4] W. C. Chew, J. M. Jin, E. Michielssen, and J. Song, *Fast efficient algorithms in computational electromagnetics*, Boston, MA: Artech House, 2001.

[5] H. Zhao, J. Hu, and Z. Nie, "Parallelization of MLFMA with Composite Load Partition Criteria and Asynchronous Communication," ACES Journal, vol. 25, no. 2, pp. 167-173, 2010.

[6] H. Fangjing, N. Zaiping, and H. Jun, "An Efficient Parallel Multilevel Fast Multipole Algorithm for Large-scale Scattering Problems," ACES Journal, vol. 25, no. 4, pp. 381-387, 2010.

[7] J. M. Rius, J. Parron, A. Heldring, J.M. Tamayo, and E. Ubeda, “Fast iterative solution of integral equations with method of moments and matrix decomposition algorithm - singular value decomposition,” *IEEE Trans. Antennas Propag*, vol. 56, no. 8, pp. 2314-2324, Aug. 2008.

[8] J. M. Rius, A. Heldring, J.M. Tamayo, and J. Parron, “The MDA-SVD algorithm for fast direct or iterative solution of discrete integral equations,” Antennas Propag, EuCAP The Second European Conference on, pp. 1-8, 2007.

[9] Y. Saad and M. H. Schultz, "GMRES: A generalized minimal residual algorithm for solving nonsymmetric linear systems," *SIAM J. Sci. Statist. Comput*, vol. 7, pp. 856–869, Jul. 1986.

[10] Y. Saad, "A flexible inner-outer preconditioned GMRES algorithm," *SIAM J. Sci. Statist. Comput*., vol. 14, pp. 461-469, 1993.

[11] R. S. Chen, D. Z. Ding, Z. H. Fan, E. K. N. Yung, and C. H. Chan, "Flexible GMRES-FFT method for fast matrix solution: Application to 3D dielectric bodies electromagnetic scattering," *Int. J. Numer. Model.: Electronic. Networks, Devices and Fields*, vol. 17, pp. 523–537, 2004.

[12] R. S. Chen, Y. Q. Hu, Z. H. Fan, D. Z. Ding, D. X. Wang, and E. K. N. Yung, "An efficient surface integral equation solution to EM scattering by chiral objects above a lossy half space," *IEEE Trans. Antennas Propag*, vol. 57, no. 11, pp. 3586-3593, Nov. 2009.

[13] E. Michielssen and A. Boag, "A multilevel matrix decomposition algorithm for analyzing scattering from large structures," *IEEE Trans. Antennas Propag*, vol. 44, no. 8, pp. 1086–1093, Aug. 1996.

[14] J. M. Rius, J. Parron, E. Ubeda, and J. Mosig, "Multilevel matrix decomposition algorithm for analysis of electrically large electromagnetic problems in 3-D," *Microw. Opt. Technol. Lett*, vol. 22, no. 3, pp. 177-182, Aug. 1999.

[15] J. Parron, G. Junkin, and J. M. Rius, "Improving the performance of the multilevel matrix decomposition algorithm for 2.5-d structures. application to metamaterials," *in Proc. Antennas Propag. Soc. Int. Symp*, pp. 2941-2944, Jul. 2006.

[16] J. Parron, J. M. Rius, and J. Mosig, "Application of the multilevel decomposition algorithm to the frequency analysis of large microstrip antenna arrays," *IEEE Trans. Magn*, vol. 38, no. 2, pp. 721-724, Mar. 2002.

[17] J. Parron, J. M. Rius, A. Heldring, E. Ubeda, and J. R. Mosig, "Analysis of microstrip antennas by multilevel matrix decomposition algorithm," in Proc. Euro. Congress Computational Methods Applied Sciences in Engineering, Barcelona, Spain, Sept. 2000.

[18] J. Parron, J. M. Rius, and J. Mosig, "Method of moments enhancement technique for the analysis of sierpinski pre-fractal antennas," *IEEE Trans. Antennas Propag*, vol.51, no.8, pp. 1872-1876, Aug. 2003.

[19] J. M. Rius, A. Heldring, J.M. Tamayo, and J. Parron, "New and more efficient formulation of MLMDA for arbitrary 3D antennas and scatterers," Antennas Propag, EuCAP The First European Conference on, pp. 1-6, 2006.

[20] A. Heldring, J.M. Tamayo, J.M. Rius, and J. Parron, "Multilevel MDA-CBI for Fast Direct Solution of Large Scattering and Radiation Problems", IEEE AP-S International Symposium 2007, Honolulu, Hawaii, USA, 10-15 June 2007.

[21] Z. Zivkovic, and A. Sarolic, "RCS simulation and comparison of two shipboard cylindrical trihedral radar reflectors in S-band and X-band", Software, Telecommunications & Computer Networks. SoftCOM 2009. 17th International Conference on pp. 60-64, 2009.

[22] J. Cheng, S. A. Maloney, R. J. Adams and F.X. Canning, "Efficient fill of a nested representation of the EFIE at low frequencies," IEEE Antennas and Propagation Society Int. Symp., pp.1-4, 2008.

Zhaoneng Jiang was born in Jiangsu Province, the People's Republic of China. He received the B.S. degree in Physics from Huaiyin Normal College in 2007, and is currently working toward the Ph.D. degree at Nanjing University of Science and Technology (NJUST), Nanjing, China. His current research interests include computational electromagnetics, antennas and electromagnetic scattering and propagation, electromagnetic modeling of microwave integrated circuits.

Zhen-Hong Fan was born in Jiangsu, the People's Republic of China in 1978. He received the M.Sc. and Ph.D. degrees in Electromagnetic Field and Microwave Technique from Nanjing University of Science and Technology (NJUST), Nanjing, China, in 2003 and 2007, respectively. During 2006, he was with the Center of wireless Communication in the City University of Hong Kong, Kowloon, as a Research Assistant. He is currently an associated Professor with the Electronic Engineering of NJUST. He is the author or coauthor of over 20 technical papers. His current research interests include computational electromagnetics, electromagnetic scattering, and radiation.

Dazhi Ding was born in Jiangsu, the People's Republic of China. He received the B.S. and Ph.D. degrees in Electromagnetic Field and Microwave Technique from Nanjing University of Science and Technology (NJUST), Nanjing, China, in 2002 and 2007, respectively. During 2005, he was with the Center of Wireless Communication in the City University of Hong Kong, Kowloon, as a Research Assistant. He is currently a Lecturer with the Electronic Engineering of NJUST. He is the author or coauthor of over 20 technical papers. His current research interests include computational electromagnetics, electromagnetic scattering, and radiation.

Ru-Shan Chen (M'01) was born in Jiangsu, P. R. China. He received his B.Sc. and M.Sc. degrees from the Dept. of Radio Engineering, Southeast University, in 1987 and in 1990, respectively, and his Ph.D. from the Dept. of Electronic Engineering, City University of Hong Kong in 2001. He joined the Dept. of Electrical Engineering, Nanjing University of Science & Technology (NJUST), where he became a Teaching Assistant in 1990 and a Lecturer in 1992. Since September 1996, he has been a Visiting Scholar with the Department of Electronic Engineering, City University of Hong Kong, first as a Research Associate, then as a Senior Research Associate in July 1997, a Research Fellow in April 1998, and a Senior Research Fellow in 1999. From June to September 1999, he was also a Visiting Scholar at Montreal University, Canada. In September 1999, he was promoted to Full Professor and Associate Director of the Microwave & Communication Research Center in NJUST and in 2007, he was appointed Head of the Dept of Communication Engineering, Nanjing University of Science & Technology. His

research interests mainly include microwave/millimeter-wave systems, measurements, antenna, RF-integrated circuits, and computational electromagnetics. He is a Senior Member of the Chinese Institute of Electronics (CIE). He received the 1992 third-class science and technology advance prize given by the National Military Industry Department of China, the 1993 third class science and technology advance prize given by the National Education Committee of China, the 1996 second-class science and technology advance prize given by the National Education Committee of China, and the 1999 first-class science and technology advance prize given by JiangSu Province as well as the 2001 second-class science and technology advance prize. At NUST, he was awarded the Excellent Honor Prize for academic achievement in 1994, 1996, 1997, 1999, 2000, 2001, 2002, and 2003. He has authored or co-authored more than 200 papers, including over 140 papers in international journals. He is the recipient of the Foundation for China Distinguished Young Investigators presented by the National Science Foundation (NSF) of China in 2003. In 2008, he became a Chang-Jiang Professor under the Cheung Kong Scholar Program awarded by the Ministry of Education, China.

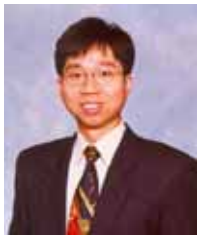

Kwok Wa Leung was born in Hong Kong SAR. He received his B.S. (Electronics) and Ph.D. (Electronic Engineering) from The Chinese University of Hong Kong in 1990 and 1993, respectively. From June 1988 to August 1989, he spent 15 months as a student trainee in the RF division of Motorola (HK) Limited. In 1994, he joined the City University of Hong Kong (CityU) as an Assistant Professor and is currently a Professor. From Jan. to June 2006, he was a Visiting Professor in the Department of Electrical Engineering, The Pennsylvania State University, USA. He was the Leader of the Departmental Graduate Research Programmes and of the BEng (Honors) Programme in Electronic and Communication Engineering at CityU. Professor Leung was the Chairman of the IEEE AP/MTT Hong Kong Joint Chapter for the years of 2006 and 2007. He was the Co-Chair of the Technical Program Committee, IEEE TENCON, Hong Kong, Nov. 2006, and was the Finance Chair of PIERS 1997, Hong Kong. He is currently the Chairman of the Technical Program Committee, 2008 Asia-Pacific Microwave Conference. His research interests include RFID tag antennas, dielectric resonator antennas, microstrip antennas, wire antennas, guided wave theory, numerical methods in electromagnetics, and mobile communications. He serves as an Editor for HKIE Transactions. He, also, serves as an Associate Editor for IEEE Transactions on Antennas and Propagation and for IEEE Antennas and Wireless Propagation Letters. Professor Leung received the International Union of Radio Science (USRI) Young Scientists Awards in 1993 and 1995, awarded in Kyoto, Japan and St. Petersburg, Russia, respectively. He is a Fellow of HKIE and a Senior Member of IEEE.

Parallel SAI Preconditioned Adaptive Integral Method For Analysis of Large Planar Microstrip Antennas

Mengmeng Li, Ming Chen, Wei Zhuang, Zhenhong Fan, and Rushan Chen

Department of Communication Engineering
Nanjing University of Science and Technology, China
david2000abc@126.com, eechenrs@mail.njust.edu.cn

Abstract ─ An efficient parallel sparse approximate inverse (PSAI) preconditioning of the adaptive integral method (AIM) is proposed to analyze the large-scale planar microstrip antennas. The PSAI preconditioner is based on the parallelized Frobenius-norm minimization, and is used to speed up the convergence rate of the loose generalized minimal residual method (LGMRES) iterative solver. The parallel AIM is used to accelerate the required matrix vector product operations. Numerical results demonstrate that the PSAI preconditioner is effective with the AIM and can increase the parallel efficiency significantly when analyzing the large planar microstrip antennas.

Index Terms ─ Adaptive integral method, microstrip antennas, parallel sparse approximate inverse.

I. INTRODUCTION

In electromagnetic (EM) calculations, the calculation of the currents generated on the surface of an object when illuminated by a given incident plane wave or fed by a microstrip line is essential for the simulation of microstrip structures. For the microstrip structures, the finite element method (FEM), and the finite-difference time-domain (FDTD) method often have a large number of unknowns due to the volumetric discretization. The method of moments (MoM) is a preferred method to solve this problem, since by using the integral equation (IE) and the layered media Green's functions, it only discretizes the metallic surface, which leads to a relative small number of unknowns. The implementation of the MoM requires $O(N^3)$ operations and $O(N^2)$ memory storage [1], where N is the number of unknowns. The size of the MoM matrix increases so rapidly with the increase of the number of unknowns that the computation will be intractable for the computational capacity. The difficulty can be overcome by use of Krylov iterative methods, and the required matrix-vector product operations can be accelerated by AIM [2]. The application of AIM reduces the memory requirement to $O(N)$ and the computational complexity to $O(NlogN)$.

With the increase of the dimensions of the object to be solved, the impedance matrix associated with the linear systems becomes larger. The computation will be time consuming for a single processor. Fortunately, the parallel technique is applied in many fast EM methods to circumvent the above difficulty. The parallel multilevel fast multipole method (MLFMA) is proposed in [3, 4] for the solution of scattering from large-scale objects, the mpi-based parallel precorrected fast Fourier transform (FFT) algorithm is proposed in [5] for analyzing scattering from arbitrary shaped three-dimensional objects, a methodology for designing a high performance parallel 3-D finite element method (FEM) is proposed in [6]. All of these techniques provide an efficient parallel scheme to deal with the large-scale problems.

Although the computational complexity and memory requirement is decreased in the fast EM methods and the computational capacity is increased by use of the parallel technique, the number of iterations needed to achieve the desired precision remains the same as the original MoM. It is natural to use preconditioning techniques [7-9] to improve the convergence of the linear systems. There are many preconditioning techniques. Simple diagonal or diagonal blocks of the impedance matrix can be parallelized easily, while

1054-4887 © 2010 ACES

they are effective only when the matrix has some degree of diagonal dominance [10]. Block diagonal preconditioner is generally more robust, which requires matrix permutations or renumbering of the grid points to cluster the large entries close to the diagonal. Incomplete LU (ILU) has been used for solving nonsysmmetric dense systems [11] and the threshold-based incomplete LU (ILUT) has been applied in the AIM [12], while the factorization is often ill conditioned that leads to the triangular solvers unstable. Shifted symmetric successive over-relaxation (SSOR) [13] and spectral two-step preconditioning techniques [14] are efficient while they are difficult to be parallelized. The SAI preconditioner based on Frobenius-norm minimization is chosen in this paper because it allows the decoupling of the constrained minimization problem into independent linear least-squares problems for each rows of the preconditioner. This is convenient to be used by parallelization. Recently, PSAI is proposed to be combined with MLFMA for solving scattering problems with a large number of unknowns [15, 16]. For layered media spatial domain Green's function, using MLFMA is much more involved than in the surface scattering problems where the free space Green's would be employed [17]. Therefore, in this paper a synthesis of the AIM and PSAI preconditioning technique is proposed for analyzing large-scale planar microstrip antennas. To the best of our knowledge, it is the first time that the parallel SAI preconditioning technique was applied into the AIM in our work. As a result, the parallel efficiency is greatly enhanced.

The paper is organized as follows. Section 2 describes the essential algorithms for the analysis of the planar microstrip antennas. The workflow of the parallel AIM is described in section 2.1; the construction of the PSAI preconditioner in the parallel AIM is described in section 2.2. Numerical results in section 3 demonstrate the efficiency of the proposed method. Finally, a brief conclusion is given in Section 4.

II. THEORY

A. The parallel AIM algorithm

For the sake of brevity, the summary, and sequence of the operations in the parallel AIM will be only described, the basic principles of the AIM can be found in [2]. It is known that the computation of the AIM technique mainly contains four parts: evaluate the near field impedance matrix, evaluate the expansion coefficients (i.e. projecting the RWG basis functions onto the rectangular grids), evaluate the matrix-vector product operations of the near field sparse matrix, and evaluate matrix-vector product operations of the far field. The AIM is able to be parallelized, since the above four operations are independent and there is independence in each operations. In this paper, the computation task is decomposed by distributing an equal number of unknowns to each processor for balancing the four operations simultaneously. The scheme is described below:

Step 1. The elements of the near field matrix are evaluated by MPIE and stored in a compressed sparse column format. The basis functions are distributed equally to every processor, and the relative elements of the near field impedance matrix are computed and stored, respectively. There is no inner-processor communications in this step.

Step 2. The basis functions are mapped onto a regular grid in order to apply the FFT to a Toeplitz matrix for speedup the matrix-vector product operations. The solution can be highly parallelized, since every basis function is independent during computation. As step1, the basis functions are distributed equally to every processor. Only part of the expansion coefficients just need to be computed for each processor.

Step 3. The direct matrix-vector product operations of the near field sparse matrix are parallelized as step 1 and step 2 by distributing the basis functions. However, frequent inner-processor communications are required during the iterative solution of the linear system, which leads to frequent inner-processor communications. The inner-processor communications will take the most of the computational time if the number of unknowns is small, and leads to a low parallel efficiency.

Step 4. The matrix-vector product operation of the Toeplitz matrix of the far field is accelerated by FFT. In the code, the two dimensional Toeplitz matrix is first extended to a one dimensional circulant matrix, and the one dimensional FFT [18] is implemented in the circulant matrix, thus the matrix-vector product operation of the far field can be parallelized by the parallel one dimensional FFT. It should be noted that the inner-processor

communication time and the synchronization time should, also, be considered as step 3.

From the above steps, it is found that there is a balance between the computational time and inner-processor communication time. For objects with a small number of unknowns, the inner-processor communication takes the most of the total solution time which leads to a low efficiency of the parallel algorithm. For objects with a large number of unknowns, the computation takes the most of the total solution time which leads to a high efficiency of the parallel algorithm. Since a fast convergence solution of the liner systems plays an important role for the efficiency of the parallel scheme, the PSAI preconditioning technique will be proposed in detail in the next part.

B. The PSAI preconditioning technique

First, we consider the SAI preconditioner combined with the AIM. In the context of AIM, the $N \times N$ dense impedance matrix is decomposed as $\mathbf{Z}=\mathbf{Z}_s + \mathbf{Z}_{AIM}$ [2], where $\mathbf{Z}_s = \mathbf{Z}_{near} - \mathbf{Z}_{near\_AIM}$. $\mathbf{Z}_{near}$ is the MoM interaction between elements, $\mathbf{Z}_{near\_AIM}$ is the inaccurate contribution from grid and $\mathbf{Z}_{AIM}$ is the matrix related to interaction from far field. Since $\mathbf{Z}_s$ is already stored in the memory, $\mathbf{Z}_s$ is chosen instead of $\mathbf{Z}_{near}$ for the construction of the SAI preconditioner and the approximation is of the form $\mathbf{M} \approx \mathbf{Z}_s^{-1}$. It is found that the iterative steps of the LGMRES with SAI preconditioner constructed by $\mathbf{Z}_s$ are similar with constructed by $\mathbf{Z}_{near}$, and it is shown in section 3. The SAI preconditioner in this paper is based on a Frobenius-norm minimization. The approximate inverse of $\mathbf{Z}_s$ is computed by minimizing

$$\left\| \mathbf{I} - \mathbf{M}\mathbf{Z}_s \right\|_F . \tag{1}$$

The Frobenius norm is usually chosen because it allows the decoupling of the constrained minimization problem into n independent linear least-squares problems for each row of M:

$$\left\| \mathbf{I} - \mathbf{M}\mathbf{Z}_s \right\|_F^2 = \left\| \mathbf{I} - \mathbf{M}\mathbf{Z}_s^T \right\|_F^2 = \sum_{j=1}^{n} \left\| e_j - \mathbf{Z}_s m_j \right\|_2^2, \tag{2}$$

where e_j is the j th unit vector and m_j is the column vector representing the j th row of $\mathbf{M}$.

The main issue for the computation of the SAI preconditioner is the selection of the nonzero pattern of $\mathbf{M}$ that is the set of indices:

$$S = \{(i, j) \in [1, N^2] \text{ s.t.} m_{ij} \neq 0\}. \tag{3}$$

If the sparsity of $\mathbf{M}$ is known, the none zero structure for the j th column of $\mathbf{M}$ can be automatically determined and defined as

$$J = \{i \in [1, N] \text{ s.t.} (i, j) \in S\}. \tag{4}$$

The solution of (2) involves only the columns of $\mathbf{Z}_s$ indexed by J, which can be denoted by $\mathbf{Z}_s(:, J)$. Since $\mathbf{Z}_s$ is sparse, many rows in $\mathbf{Z}_s(:, J)$ are usually null, not affecting the solution of the least-square problems. Thus, if I is the set of indices corresponding to the nonzero rows in $\mathbf{Z}_s(:, J)$, and if we defined $\tilde{\mathbf{Z}} = \mathbf{Z}_s(I, J)$ by $\tilde{m}_j = m_j(J)$ and $\tilde{e}_j = e_j(J)$, the "reduced" least-square problems to solve are

$$\min \left\| \tilde{e}_j - \tilde{\mathbf{Z}}_s \tilde{m}_j \right\|_2^2, \qquad j = 1, \ldots N. \tag{5}$$

In general, the size of problems (5) is much smaller than problems (2). The above procedure is shown clearly in Figure 1.

As shown in Figure 1(a), "X" stands for none zero impedance matrix elements, and m_4 is chosen to be computed as an example. For row 4, since the none zero columns are 2, 4, 6, 8, the rows of 2, 4, 6, 8 in Figure 1(a) are chosen. Then, the submatrix in Figure 1(b) is obtained for constructing the preconditioner. Excluding the columns with null elements in the above submatrix, after which the final least matrix in Figure 1(c) will be obtained. It can be seen that the size of the "reduced" matrix in Figure 1(c) is much smaller than the original matrix in Figure 1(a). Although the null columns are excluded, the size of the "reduced" matrix in (5) is still very large for the targets with a large number of unknowns. The difficulty can be circumvented with a prior sparsity pattern selection strategy. In the code, a constant number K_{max} is set to select the most informative elements in each row of Zs for the construction of the preconditioner by checking the value of the elements [19, 20].

The core of PSAI preconditioner is to store the minimum near field impedance matrix in each processor. The PSAI preconditioner is constructed by three steps. First, the elements of the sparse near field impedance matrix are distributed evenly on the processors. Second, the required elements which are distributed on the other processors are appended on the present processor by the all-to-all communication of the rows and columns list and the value of the elements, and the process is shown in Figure 2 to Figure 4. Third, the least-squares

minimizations are solved independently on each processor as the construction of the SAI preconditioner described above.

	1	2	3	4	5	6	7	8
1	X	X			X			
2	X	X		X				X
3			X					
4		X		X		X		X
5	X							
6				X				X
7								
8		X		X		X		X

(a)

	1	2	3	4	5	6	7	8
2	X	X		X				X
4		X		X		X		X
6				X				X
8		X		X		X		X

(b)

	1	2	4	6	8
2	X	X	X		X
4		X	X	X	X
6			X		X
8		X	X	X	X

(c)

Fig. 1. The configuration of the SAI, (a) the original impedance matrix, (b) the selected rows of the matrix for construction of the SAI preconditioner, (c) the reduced impedance matrix for construction of the SAI preconditioner.

The above algorithm is shown in Figure 5 clearly. Considering the impedance matrix of the near field, the elements of the matrix $\mathbf{Z}_s$ in rows 1-4 and 5-8 are distributed in two processors respectively. m_4 is to be solved as discussed above. The elements of rows 2, 4, 6, 8 of the impedance matrix should be selected, while rows 6 and 8 are in the other processor; thus, the necessary inner-processor communications are implemented to append rows 6 and 8 to the first processor as shown in Figure 2(c). After the procedure of the all-to-all communication, all the processors store the minimum elements of the matrix $\mathbf{Z}_s$. It should be noted that the inner-processor communication in the construction of PSAI preconditioner is small since there is a trade-off for controlling the selected number of elements in each row of Zs. The flow chart of the PSAI preconditioned AIM is shown in Figure 6 clearly. As shown in Figure 6, there is inner-processor communication in the process to evaluate the near field, project the unknowns onto the regular grid. And there is inner-processor communication in the process of construction of the SAI preconditioner and the matrix vector multiplication.

```
for each z_ij ∈ Z_k^s
Do i = 1, n_k
    if j is not in the local rank, then
        P = findProcId(j)
        Append j into rowRecvList(P)
    endif
Endfor
```

Fig. 2. The process that finds and exchanges the rows list of the elements should be appended of each processor, where *rowSendList(P)*, *rowRecvList(P)*is the row list to be sent and received of processor *p*.

```
For i ∈ rowSendList, do
    Append column indices of row i to sendColIndices
Endfor
Send sendColIndices, receive recColIndices at the same time ! All-to-All communication
```

Fig. 3. The process that finds and exchanges the columns list of the elements should be appended of each processor, where *sendColIndices*, *recColIndices* is the column list to be sent and received.

For $i \in rowSendList$, do

Append the matrix element z_{ij} of row i to *sendColValues*

Endfor

Send *sendColValues*, receive *recvColValues* at the same time !

All-to-All communication

Fig. 4. The process that finds and exchanges the values of the elements to be sent and received by processor *p*, where *sendcolIndices*, *reccolIndices* is the value of the elements to be sent and received.

	1	2	3	4	5	6	7	8
1	X	X			X			
2	X	X		X				X
3			X					
4		X		X		X		X
5	X							
6				X				X
7								
8		X		X		X		X

(a)

	1	2	3	4	5	6	7	8
1	X	X			X			
2	X	X		X				X
3			X					
4		X		X		X		X

(b)

	1	2	3	4	5	6	7	8
1	X	X			X			
2	X	X		X				X
3			X					
4		X		X		X		X
6				X				X
8		X		X		X		X

(c)

Fig. 5. The configuration of the parallel SAI, (a) the original impedance matrix, (b) the rows of the impedance matrix stored in one processor, (c) the appended minimum impedance matrix been stored in one processor for construction of the PSAI preconditioner.

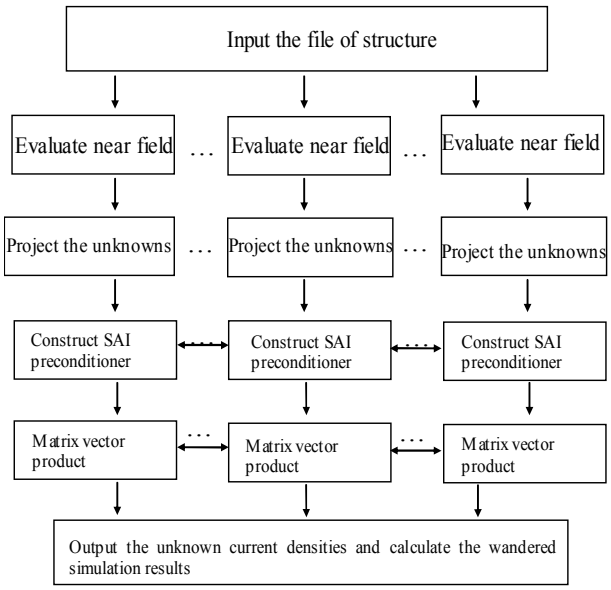

Fig. 6. The flow chart for the PSAI preconditioned AIM.

III. RESULTS AND DISCUSSIONS

In this section, some microstrip antennas are analyzed by the PSAI preconditioned AIM. The resultant linear systems are solved by the LGMRES solver [21] and its tolerance is 10^{-4}. The results presented here are all computed on 2-node clusters connected with an infiniband network. Each node includes a quad-core Intel processor and 8 GB of RAM.

First, an 8×8 microstrip corporate-fed planar antenna is considered, the parameters are depicted in Figure 6. It is discretized with 61, 345 RWG unknowns. As shown in Figure 7, the reflection coefficients versus frequency simulated by the proposed method and the Ansoft Designer® are plotted. It can be seen the results agree well which demonstrate the accuracy of the proposed method. The total simulation time of one frequency point for the PSAI preconditioned AIM is 2, 512 s, and the time for the Ansoft Designer® is 12, 560s. We, also, compare the H-plane far field pattern of the 8×8 microstrip antenna at the frequency of 9.42 GHz with the CGFFT approach [22] in Figure 8 to verify the proposed method, where reasonable agreements are observed. The time for constructing the PSAI preconditioner is 613 s and the solution time is 1, 576 s. Figure 9 shows the residual norm histories for the 8×8 microstrip corporate-fed planar antenna at 9.42 GHz

simulated by AIM with and without the PSAI preconditioner. The label "PSAI-0" represents the PSAI preconditioner constructed by Znear, and "PSAI-1" represents the PSAI preconditioner constructed by $\mathbf{Z}_s$. It is found that the LGMRES PSAI-0 and PSAI-1 have the similar iterative steps which can greatly improve the convergence by a factor of 3.8. In order to describe the proposed method clearly, the label "PSAI" shown below denotes the PSAI preconditioner constructed by $\mathbf{Z}_s$. The advantage of the PSAI preconditioner can be found significantly when solving large dense linear systems with multiple right-hand sides arising in monostatic RCS, since the PSAI preconditioner needs to be constructed only once.

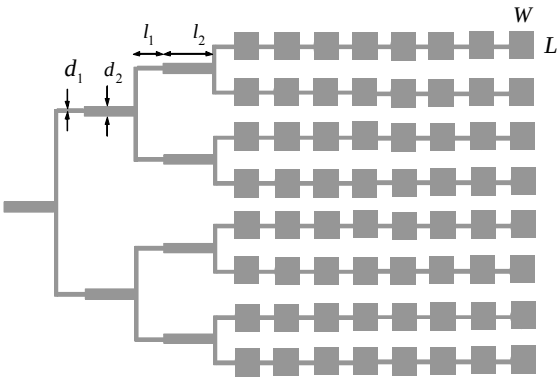

Fig. 7. The geometry of the 8×8 microstrip corporate-fed planar antenna, L_1=12.32mm, L_2 =18.48mm, W=10.08mm, L=11.79mm, d_1=1.3mm, d_2=3.93mm,the thickness of substrate h=1.59mm, $\varepsilon_r = 2.2$.

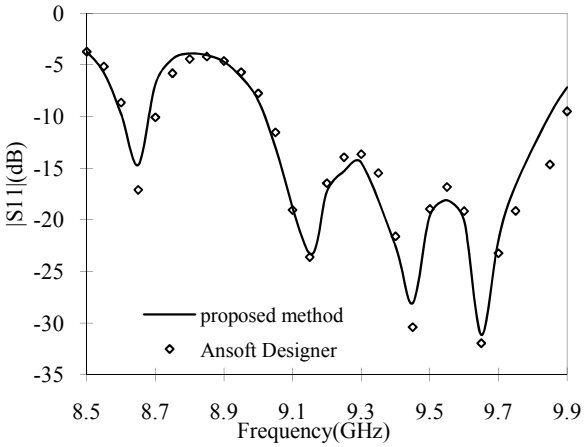

Fig. 8. The reflection coefficients versus frequency for the 8×8 corporate-fed planar antenna.

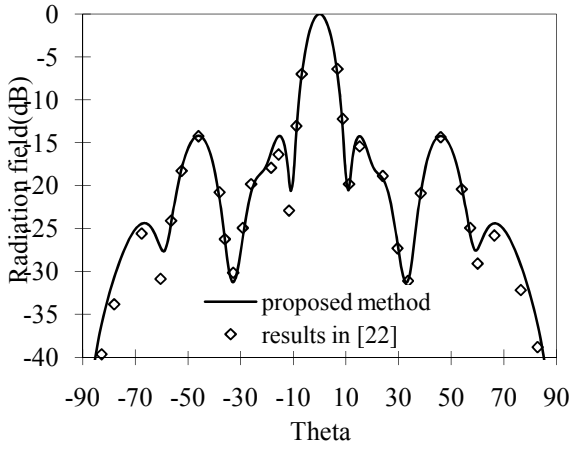

Fig. 9. The H-plane far field pattern of the 8×8 microstrip corporate-fed planar antenna compared with [22].

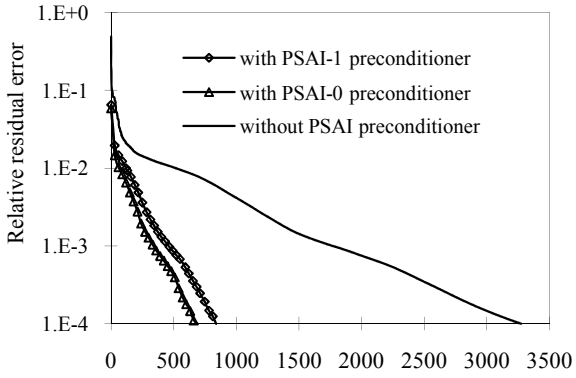

Fig. 10. Residual norm histories for the 8×8 microstrip corporate-fed planar antenna at 9.42 GHz simulated by LGMRES with and without the PSAI preconditioner.

To examine the parallel efficiency of the proposed method, the monostatic RCS of a series of microstrip antennas [23] are simulated. The layout of the microstrip antennas are shown in Figure 10, the configuration of the unit of the arrays is $L = 3.66\text{cm}$, $W = 2.60\text{cm}$, $a = b = 5.517\text{cm}$, the dielectric constant and the thickness of the substrates is $\varepsilon_r = 2.17$, $d = 0.158\text{cm}$. The microstrip antennas with 7×7, 20×20 arrays are simulated. The number of unknowns is 8, 428 and 84, 000, respectively. Table 1 and Table 2 list the CPU time of the above antennas simulated by AIM with and without the PSAI preconditioner at

the frequency of 3.7 GHz. The notations used in the tables are denoted below.

- *near* denotes the time used for filling the near field impedance matrix.
- *cof* denotes the time used for computing the expansion coefficients.
- *set* denotes the time used for constructing the PSAI preconditioner.
- *steps* denotes the average number of iterative steps of the LGMRES for $\varphi = 0^\circ$ and θ varying from 0° to 85°.
- *sol* denotes the time used for solving the liner systems.
- *tol* denotes the total CPU time for simulation.
- *mem* denotes the memory usage for one processor.
- *ef* denotes the efficiency of the parallelization which is defined as $\frac{T_{Total}}{nT_{nTotal}}$, where T_{Total} is the total CPU time computed by one processor, T_{nTotal} is the total CPU time computed by n processors.

As shown in Table 1, the time for filling near field matrix and solving the expansion coefficients in columns 3, 4 is almost a linear reduction with the increase of the number of processors. In column 5, little solving time of the linear system is saved when the number of unknowns is small (i.e. the 7×7 arrays), since the inner-processor communication takes the most of the CPU time. Much solving time of the linear systems is saved when the number of unknowns is large (i.e. the 20×20 arrays), since the computation takes the most of the CPU time. Similarly, as shown in Table 2, the time for filling the near field matrix, solving the expansion coefficients and construction of the preconditioner in columns 3, 4, and 5 is also linear reduction with the increase of the number of processors.

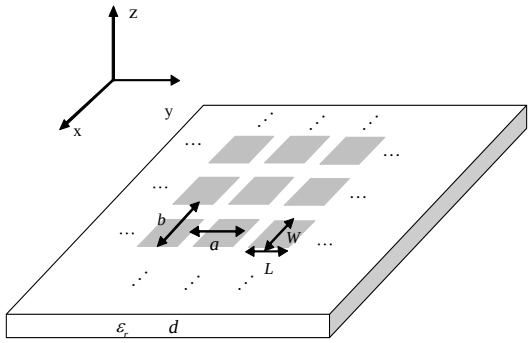

Fig. 11. The layout of the microstrip antenna.

Little solving time of the linear system in columns 6 is saved, when the number of unknowns is small (i.e. the 7×7), and much solving time of the linear systems is saved when the number of unknowns is large (i.e. the 20×20 arrays). Comparing the memory storage, the total solving time, and the parallel efficiency of Table 1 and Table 2, it can be found that by using the PSAI preconditioner only increases small memory usage while the total solving time and the parallel efficiency are improved significantly due to the decrease of the number of iterative steps of the LGMRES.

Finally, we verify the proposed method by a 30×30 microstrip antenna with 231, 300 RWG basis functions. The monostatic RCS computed by the AIM with and without PSAI preconditioner is plotted in Figure 11, where reasonable agreements are observed. The time for constructing the PSAI preconditioner and per iteration is 1, 304, and 5 seconds, respectively. Figure 12 shows the iterative steps of the LGMRES with and without a PSAI preconditioner for the 30×30 microstrip arrays. Where $\varphi = 0^\circ$ and θ is varying from 0° to 85°. It can be found that the PSAI preconditioning technique can greatly improve the convergence by at least a factor of 4.1 compared with no preconditioned LGMRES.

Table 1: The CPU time of the 7×7 and 20×20 arrays simulated by the AIM without PSAI preconditioner

	processors	near(sec)	cof(sec)	steps	sol(sec)	tol(sec)	mem(Mb)	ef
7×7	1	312	144	243	8, 319	8, 790	43	-
	4	78	36		8, 094	8, 215	30	26%
	8	39	18		7, 710	7, 770	25	14%
20×20	1	12, 724	5, 842	257	102, 017	120, 684	410	-
	4	3, 862	1, 367		47, 355	52, 685	171	57%
	8	1, 977	723		43, 771	46, 572	149	32%

Table 2: The CPU time of the 7×7 and 20×20 arrays simulated by the AIM with PSAI preconditioner

	Processors	near (sec)	cof(sec)	set(sec)	steps	sol(sec)	tol(sec)	mem(Mb)	ef
7×7	1	312	144	886	13	891	2, 241	69	-
	4	78	36	222		655	996	42	56%
	8	39	18	111		608	782	30	36%
20×20	1	12, 724	5, 842	10, 251	19	7, 413	36, 588	510	-
	4	3, 862	1, 367	2, 447		6, 314	11, 737	210	78%
	8	1, 977	723	1, 310		4, 830	8, 959	158	51%

IV. CONCLUSION

In this paper, the PSAI preconditioned AIM method is proposed for analyzing the large scale microstrip antennas. The parallel AIM is used to accelerate the matrix vector multiplication. The PSAI is used to improve the iterative convergence of the LGMRES. The PSAI is based on the parallelized Frobenius-norm minimization, and the construction time of the preconditioner is further saved by selecting the most informative elements of the sparse near field impedance matrix. Numerical results prove that by using the PSAI preconditioner, the parallel efficiency is significantly improved.

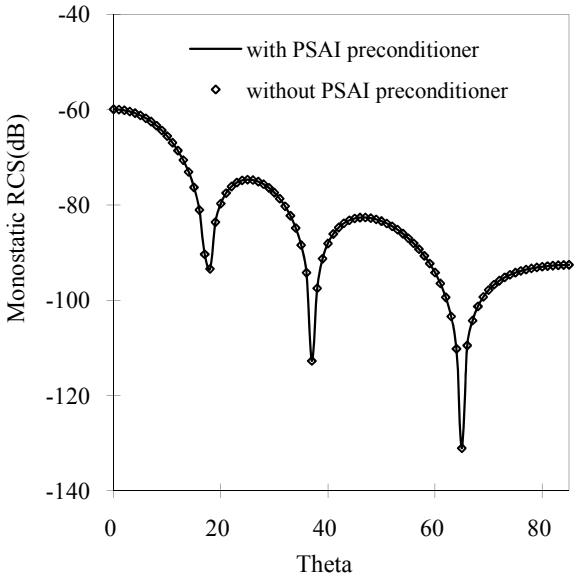

Fig. 12. The monostatic RCS of the 30×30 microstrip arrays simulated by the AIM with and without PSAI preconditioner, $\varphi = 0^\circ$ and θ is varying from 0° to 85°, and the frequency of the incident plane wave is 300MHz.

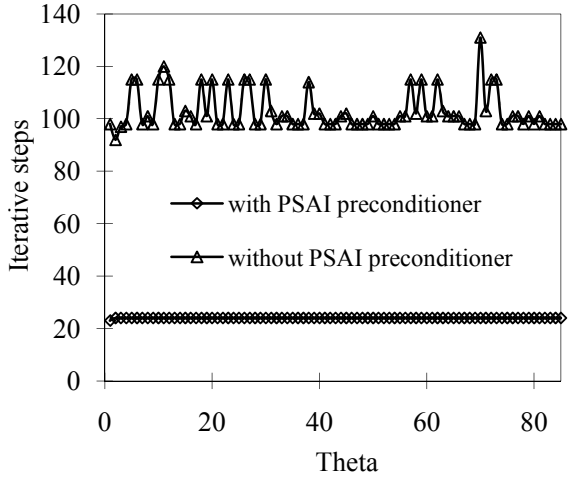

Fig. 13. The iterative steps of the LGMRES for the 30×30 microstrip arrays simulated by the AIM with and without PSAI preconditioner, $\varphi = 0^\circ$ and θ is varying from 0° to 85°, and the frequency of the incident plane wave is 300MHz. And the tolerance of LGMRES is 10^{-4}.

ACKNOWLEDGMENT

The author would like to thank the support of the Major State Basic Research Development Program of China (973 Program: 2009CB320201); Natural Science Foundation of 60871013, 60701005; Jiangsu Natural Science Foundation of BK2008048.

REFERENCES

[1] R. F. Harringlon, *Field computation by Moment Methods*, New York. MacMillan, 1968.

[2] F. Ling, C .F. Wang, and J. M. Jin, "An efficient algorithm for analyzing large-scale microstrip structures using adaptive integral method combined with discrete complex-image method,"

IEEE Trans. Antennas Propag., vol. 48, no.5, pp. 832 – 839, 2000.

[3] X. M. Pan, and X. Q. Sheng, "A high performance parallel MLFMA for scattering by extremely large targets," *Microwave Conference.*, pp. 16-20, 2008.

[4] Ö. Ergül and L. Gürel, "Efficient parallelization of the multilevel fast multipole algorithm for the solution of large-scale scattering problems," *IEEE Trans. Antennas Propag.*, vol. 56, no. 8, pp. 2335-2345, 2008.

[5] L. -W. Li, Y. J. Wang, and E.-P. Li, "Mpi-based parallelized precorrected FFT algorithm for analyzing scattering by arbitrary shaped three-dimensional objects," *Progress In Electromagnetic Research.*, PIER 42, pp. 247-259, 2003.

[6] D. Q. Ren, Park. T., Mirican. B., McFee. S., and Giannacopoulos. D. D, "A methodology for performance modeling and simulation validation of parallel 3-D finite element mesh refinement with tetrahedral," *IEEE Trans. Magn.*, vol. 44, no. 6, pp. 1406-1409, 2008.

[7] Y. Saad, *Iterative methods for sparse linear systems*, PWS Publishing Company: New York, 1996.

[8] W. -B. Ewe, L. -W .Li, Q. Wu, and M.-S. Leong, "Preconditioners for Adaptive Integral Method Implementation," *IEEE Trans. Antennas Propag.*, vol. 53, no. 7, pp. 2346-2350, July 2005.

[9] J. Lee, J. Zhang, and C. Lu, "Performance of Preconditioned Krylov Iterative Methods for Solving Hybrid Integral Equations in Electromagnetics," *ACES Journal*, vol. 18, no. 3, pp. 54-61, 2003.

[10] J. M. Song, C. C. Lu, and W. C. Chew, "Multilevel fast multipole algorithm for electromagnetic scattering by large complex objects," *IEEE Trans. Antennas Propag.*, Vol. 45, No. 10, pp. 1488-1493, 1997.

[11] K. Sertel and J. L. Volakis, "Incomplete LU preconditioner for FMM implementation," *Microw. Opt. Technol. Lett.*, vol. 26, no. 7, pp. 265–267, 2000.

[12] M. Zhang, T. S. Yeo, and L. -W .Li, "Threshold-based Incomplete LU Factorization Preconditioner for Adaptive Integral Method," *Proc of 2007 Asia-Pacific Microwave Conference*, Bangkok, Thailand, pp. 913-916, December 11-14, 2007.

[13] J. Q. Chen, Z. W. Liu, K. Xu, D. Z. Ding, Z. H. Fan, and R. S. Chen, "Shifted SSOR preconditioning technique for electromagnetic wave scattering problems," *Microw. Opt. Technol. Lett.*, vol. 51, no. 4, pp. 1035-1039, 2009.

[14] P. L. Rui, R. S. Chen, D.X. Wang, and E.K.N. Yung, "Spectral two-step preconditioning of multilevel fast multipole algorithm for the fast monostatic rcs calculation," *IEEE Trans. Antennas Propag.*, vol. 55, no. 8, pp. 2268-2275,2007.

[15] M. Tahir, G. Levent, "Accelerating the multilevel fast multipole algorithm with the sparse-approximate-inverse (SAI) preconditioning," *SIAM. J. Sci. Comput.*, Vol. 3, No. 3, pp. 1969-1984, 2009.

[16] T. Malas, Ö. Ergül, and L. Gürel, "Parallel preconditioners for solutions of dense linear systems with tens of millions of unknowns," *22nd International Symposium on Computer and Information Sciences (ISCIS 2007)*, 1-4, 2007.

[17] J.-S. Zhao, W. C. Chew, C.-C. Lu, E. Michielssen, and J. Song, " Thin-stratified medium fast-multipole algorithm for solving microstrip structures," *IEEE Trans. Microwave Theory Tech.*, vol. 46, no.4, pp. 395-403, Apr. 1998..

[18] D. Takahashi. Graduate School of Systems and Information Engineering University of Tsukuba. http://www.ffte.jp/s. 2004.

[19] P. L. Rui, R. S. Chen, "Sparse approximate inverse preconditioning of deflated block-GMRES algorithm for the fast monostatic RCS calculation," *International Journal of Numerical Modelling: Electronic Networks, Devices and Fields.*, vol. 21, pp. 297-307, 2008.

[20] D. Z. Ding, R. S. Chen and Z, H. Fan, "An efficient SAI preconditioning technique for higher order hierarchical MLFMM implementation," *Progress in Electromagnetics Research*, PIER 88, pp. 255-273, 2008.

[21] W. Zhuang, Z.H. Fan, and Y.Q. Hu, "Adaptive Integral Method (AIM) Combined with the Loose GMRES Algorithm for Planar Structures Analysis," *International Journal of RF and Microwave Computer-Aided Engineering.*, vol. 19, pp. 24-32, 2009.

[22] C. F. Wang, F. Ling, and J. M. Jin, "A fast full-wave analysis of scattering and radiation from large finite arrays of microstrip antennas," *IEEE Trans. Antennas Propagat.*, vol. 46, no.10, pp. 1467–1474, 1998.

[23] A. S. King and W. J. Bow, "Scattering from a finite array of microstrip patches," *IEEE Trans. Antennas Propagat .*, vol. 40, no. 2, pp. 770-774, 1992.

Meng-Meng Li was born in Jiangsu Province, the People's Republic of China in 1984. He received the B.S. degree in Physics from Huaiyin Normal College in 2007, and is currently working toward the Ph.D. degree at Nanjing University of Science and Technology. His research interests focus on fast solution of integral

equations, modeling of microwave integrated circuits, and UWB antennas.

Ming Chen was born in Jiangsu Province, the People's Republic of China in 1983. He received the B.S. degree in Physics from Anhui University in 2006, and is currently working toward the PH.D. degree at Nanjing University of Science and Technology. His research interests focus on fast solution of integral equations, electromagnetic scattering, and propagation.

Wei Zhuang was born in Jiangsu Province, the People's Republic of China in 1980. He received the Ph.D. degree at Nanjing University of Science and Technology in 2009. His research interests focus on fast solution of integral equations, electromagnetic scattering, and propagation.

Zhen-Hong Fan was born in Jiangsu, the People's Republic of China in 1978. He received the M.Sc. and Ph.D. degrees in Electromagnetic Field and Microwave Technique from Nanjing University of Science and Technology (NJUST), Nanjing, China, in 2003 and 2007, respectively. During 2006, he was with the Center of wireless Communication in the City University of Hong Kong, Kowloon, as a Research Assistant. He is currently an associated Professor with the Electronic Engineering of NJUST. He is the author or coauthor of over 20 technical papers. His current research interests include computational electromagnetics, electromagnetic scattering, and radiation.

Ru-Shan Chen (M'01) was born in Jiangsu, P. R. China. He received his B.Sc. and M.Sc. degrees from the Dept. of Radio Engineering, Southeast University, in 1987 and in 1990, respectively, and his Ph.D. from the Dept. of Electronic Engineering, City University of Hong Kong in 2001. He joined the Dept. of Electrical Engineering, Nanjing University of Science & Technology (NJUST), where he became a Teaching Assistant in 1990 and a Lecturer in 1992. Since September 1996, he has been a Visiting Scholar with the Department of Electronic Engineering, City University of Hong Kong, first as a Research Associate, then as a Senior Research Associate in July 1997, a Research Fellow in April 1998, and a Senior Research Fellow in 1999. From June to September 1999, he was also a Visiting Scholar at Montreal University, Canada. In September 1999, he was promoted to Full Professor and Associate Director of the Microwave & Communication Research Center in NJUST and in 2007, he was appointed Head of the Dept of Communication Engineering, Nanjing University of Science & Technology. His research interests mainly include microwave/millimeter-wave systems, measurements, antenna, RF-integrated circuits, and computational electromagnetics. He is a Senior Member of the Chinese Institute of Electronics (CIE). He received the 1992 third-class science and technology advance prize given by the National Military Industry Department of China, the 1993 third class science and technology advance prize given by the National Education Committee of China, the 1996 second-class science and technology advance prize given by the National Education Committee of China, and the 1999 first-class science and technology advance prize given by JiangSu Province as well as the 2001 second-class science and technology advance prize. At NUST, he was awarded the Excellent Honor Prize for academic achievement in 1994, 1996, 1997, 1999, 2000, 2001, 2002, and 2003. He has authored or co-authored more than 200 papers, including over 140 papers in international journals. He is the recipient of the Foundation for China Distinguished Young Investigators presented by the National Science Foundation (NSF) of China in 2003. In 2008, he became a Chang-Jiang Professor under the Cheung Kong Scholar Program awarded by the Ministry of Education, China.

Well-Conditioned CFIE for Scattering from Dielectric Coated Conducting Bodies above a Half-Space

Dazhi Ding, Jinmin Ge, and Rushan Chen

Department of Communication Engineering
Nanjing University of Science and Technology, Nanjing, 210094, China
dzding@mail.njust.edu.cn

Abstract ─ In this paper, a well-conditioned coupled combined-field integral equation called the electric and magnetic current combined-field integral equation (JCFIE-JMCFIE) is proposed for the analysis of electromagnetic scattering from coated targets above a lossy half-space. The half-space multilevel fast multipole algorithm (MLFMA) is used to reduce computational complexity. The inner-outer flexible generalized minimal residual method (FGMRES) was used as the iterative solver to further speed up the convergence rate. Numerical results were presented to demonstrate the accuracy and efficiency of the proposed method.

Index Terms ─ Electric and magnetic current combined-field integral equation (JMCFIE), flexible generalized minimal residual method (FGMRES), half-space, multilevel fast multipole algorithm (MLFMA).

I. INTRODUCTION

There is significant interest in scattering from conducting bodies coated with dielectric materials situated in the presence of a lossy half-space [1-5]. It has applications in many domains such as communications, target identification, and so on. One of the principal tools for the analysis of such scattering is the method of moments (MoM) [6]. The electromagnetic integral equation is first discretized into a matrix equation using the Galerkin-based MoM with subdomain basis functions such as Rao–Wilton–Glisson (RWG) functions [7] for triangular patches. When iterative solvers are used to solve the MoM matrix equation; the fast multipole algorithm (FMA) or multilevel fast multipole algorithm (MLFMA) [8-11] can be used to accelerate the calculation of matrix–vector products. The half-space MLFMA differs from the free-space MLFMA. In half-space MLFMA, the near interaction terms are evaluated efficiently via the discrete complex-image method (DCIM) [12, 13]. The far interaction terms are evaluated efficiently by employing the asymptotic form of the dyadic Green's function. Each component of the approximate Green's function is expressed in terms of the direct-radiation term plus radiation from an image source in real space [14]. The former accounts for the radiation of currents into the medium in which it resides, while the latter accounts for interactions with the half-space interface. The half-space MLFMA remains the same computational complexity of O(NlogN) both in RAM and computational requirement (per iteration) as free-space MLFMA.

Although the calculation complexity and memory will be decreased in MLFMA, the number of iterations needed to achieve desired precision cannot be reduced. Actually the number of iterations largely depends on the spectral properties of the integral operator or the distribution of the impedance matrix's eigenvalues. To effectively reduce the number of iterations, there are mainly two methods. One is to construct a new integral equation leading to a well-conditioned matrix equation. The other is to use fast iteration techniques and efficient preconditioning techniques to reduce the condition number of the operator equations. Researchers have investigated various integral equations for 3D coated conducting objects [15-17]. Employing the surface equivalence principle, the problem is formulated in terms of a set of coupled integral equations involving equivalent electric and magnetic surface currents which represent boundary fields. The most familiar formulation for

1054-4887 © 2010 ACES

this problem is the Poggio-Miller-Chang-Harrington-Wu-Tsai (PMCHWT) integral equation combined with electric field integral equation (EFIE) [18]. The PMCHWT formulation belongs to the integral equations of the first kind and it is found to be free of interior resonances and yields accurate and stable solutions; however, its iteration convergence rate is found to be slow [17]. To solve this problem, a new electric and magnetic current combined-field integral equation (JMCFIE) is developed leading to a well tested system with the RWG basis functions and Galerkin's method for scattering problems in free-space [16, 19-20]. Özgür Ergül and Levent Gürel have, also, applied the JMCFIE formulation with MLFMA for fast analysis of scattering from dielectric objects [19]. Researchers have, also, developed efficient iteration techniques and robust preconditioning techniques for the Krylov subspace iterative methods; among which, the GMRES (generalized minimal residual) method proposed in [21] is the most popular and efficient method for the iterative solution of sparse linear systems with an unsymmetric nonsingular matrix. For the GMRES algorithm, this can be easily accomplished with the help of a rather simple modification of the standard algorithm, referred to as the inner-outer flexible generalized minimum residual method (FGMRES) [21-24]. An important property of FGMRES is that it satisfies the residual norm minimization property over the preconditioned Krylov subspace just as in the standard GMRES algorithm.

The objective of this paper is to achieve a fast and accurate solution to the electromagnetic wave scattering from an arbitrary shaped coated conducting target situated in the presence of a lossy half-space. In this paper, we extended the JMCFIE method combined with MLFMA to efficiently analyze electromagnetic scattering from coated targets above a lossy half-space. This paper is outlined as follows. Section 2 gives an introduction of well-conditioned coupled surface integral equation. Numerical examples are given to demonstrate the accuracy and efficiency of the proposed method in radar cross section (RCS) calculations in Section 3. Section 4 gives some conclusions.

II. FORMULATION AND THEORY

As shown in Figure 1, the configuration of an arbitrarily shaped conducting body coated with dielectric materials in half-space. The dielectric parameters of space are $(\varepsilon_1, \mu_1, \sigma_1)$ and $(\varepsilon_{\text{half}}, \mu_{half}, \sigma_{half})$. As shown in Figure 1, the dielectric surface is S_d, and the metallic surface is S_c. The composite structure is illuminated by an incident plane wave (E^{inc}, H^{inc}). By invoking the equivalence principle [18], two equivalent problems are formulated, each valid for regions external and internal to the dielectric material as shown in Figure 1.

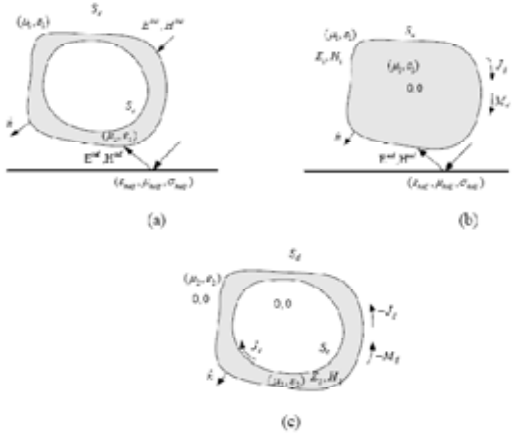

Fig. 1. Configuration of an arbitrarily shaped conducting body coated with dielectric materials (a) original problem (b) outer problem (c) inner problem.

In the equivalence problem for the external region, dielectric surface S_d is replaced by a fictitious mathematical surface. The entire space is filled with external medium $(\varepsilon_1, \mu_1, \sigma_1)$. The field inside the surface S_d is set to zero. Equivalent electric current $\mathbf{J}_d$ and equivalent magnetic current $\mathbf{M}_d$ are presented on S_d. The so-called T equations T-EFIE$_1$ and T-MFIE$_1$ for the exterior equivalent problem can be derived by taking the tangential boundary continuity conditions on the object's surface [18]:

$$\left(\mathbf{E}_1^{inc} + \mathbf{E}_1^{ref}\right)\Big|_{\tan} = \left[-\mathbf{E}_1^{s}\right]\Big|_{\tan} \tag{1}$$

$$\left(\mathbf{H}_1^{inc} + \mathbf{H}_1^{ref}\right)\Big|_{\tan} = \left[-\mathbf{H}_1^{s}\right]\Big|_{\tan} \tag{2}$$

$$\begin{aligned}\mathbf{E}_1^s = -(&j\omega\mu_1 \int_{T'} \bar{\bar{\mathbf{K}}}^A \cdot \mathbf{J}_d dS' - \frac{\nabla}{j\omega\varepsilon_1}\int_{T'} K^{\phi e}\nabla_s' \cdot \mathbf{J}_d dS' \\ &- \int_{T'} \bar{\bar{\mathbf{G}}}^{EM} \cdot \mathbf{M}_d dS' + \frac{1}{2}\mathbf{n}_1 \times \mathbf{M}_d)\end{aligned} \tag{3}$$

$$\mathbf{H}_1^s = -(j\omega\varepsilon_1\int_{T'}\bar{\bar{\mathbf{K}}}^F\cdot\mathbf{M}_d dS' - \frac{\nabla}{j\omega\mu_1}\int_{T'}K^{\phi m}\nabla_s'\cdot\mathbf{M}_d dS' - \int_{T'}\bar{\bar{\mathbf{G}}}^{HJ}\cdot\mathbf{J}_d dS' + \frac{1}{2}\mathbf{n}_1\times\mathbf{J}_d), \tag{4}$$

where the half-space Green's functions $\bar{\bar{\mathbf{K}}}^A$ $\bar{\bar{\mathbf{K}}}^F$ are for the vector potentials and $K^{\phi e}$ $K^{\phi m}$ are for the scalar potentials, meanwhile, $\bar{\bar{\mathbf{G}}}^{EM}$ is dyadic Green's function for electric field due to magnetic currents and $\bar{\bar{\mathbf{G}}}^{HJ}$ is for magnetic field due to electric current. For detailed spectral domain expressions of these half-space Green's functions please refer to [25]. In general, the spatial domain Green's functions are expressed in terms of Sommerfeld integrals. Due to the highly oscillatory nature of the integrand, numerical integration is very time consuming. In this paper, a two-level generalized pencil of function (GPOF) method is utilized to realize DCIM [13]. In the two-level GPOF, dense sampling is adopted to get full information in the quick variant area where k_ρ is relative small, while a sparse sampling in the slow variant area. In this way, high precision can be realized with fewer samples [13]. Then the spatial domain Green's functions can be obtained in closed forms from their spectral-domain counterparts via the Sommerfeld identity. By operating with $\hat{\mathrm{n}}_1\times$ to (1) and (2) on the object's surface the so-called N equations, N-EFIE$_1$ and N-MFIE$_1$, for the exterior equivalent problem can be derived

$$\mathbf{n}_1\times\left(\mathbf{E}_1^{inc}+\mathbf{E}_1^{ref}\right)=\mathbf{n}_1\times\left(-\mathbf{E}_1^s\right) \tag{5}$$

$$\mathbf{n}_1\times\left(\mathbf{H}_1^{inc}+\mathbf{H}_1^{ref}\right)=\mathbf{n}_1\times\left(-\mathbf{H}_1^s\right). \tag{6}$$

In the equivalence problem for the interior region in Figure 1(c), the medium outside is given the same material parameters $(\varepsilon_2,\mu_2,\sigma_2)$ as the coated dielectric medium. The conducting surfaces located inside the dielectric body are also replaced by fictitious mathematical surfaces. The equivalent electric current $-\mathbf{J}_d$ and equivalent magnetic current $-\mathbf{M}_d$ are presented on S_d. The equivalent current $\mathbf{J}_c$ is introduced on the conducting surface S_c. Based on the boundary conditions, T-EFIE$_2$ and T-MFIE$_2$ are presented:

On dielectric surface S_d:

$$\mathbf{E}_2^{inc}\big|_{\tan}=\left(-\mathbf{E}_2^s\right)\big|_{\tan} \tag{7}$$

$$\mathbf{H}_2^{inc}\big|_{\tan}=\left(-\mathbf{H}_2^s\right)\big|_{\tan}. \tag{8}$$

On metallic surface S_c:

$$\mathbf{E}_2^{inc}\big|_{\tan}=\left(-\mathbf{E}_2^s\right)\big|_{\tan} \tag{9}$$

$$\mathbf{E}_2^s=-\begin{pmatrix} j\omega\mu_2\int_{T'}g_2\cdot(-\mathbf{J}_d)dS'-\frac{\nabla}{j\omega\varepsilon_2}\int_{T'}g_2\nabla_s'\cdot(-\mathbf{J}_d)dS'+\int_{T'}\nabla g_2\times(-\mathbf{M}_d)dS' \\ +\frac{1}{2}\mathbf{n}_2\times(-\mathbf{M}_d)+j\omega\mu_2\int_{T'}g_2\cdot(\mathbf{J}_c)dS'-\frac{\nabla}{j\omega\varepsilon_2}\int_{T'}g_2\nabla_s'\cdot(\mathbf{J}_c)dS' \end{pmatrix} \tag{10}$$

$$\mathbf{H}_2^s=-\begin{pmatrix} j\omega\varepsilon_2\int_{T'}g_2\cdot(-\mathbf{M}_d)dS'-\frac{\nabla}{j\omega\mu_2}\int_{T'}g_2\nabla_s'\cdot(-\mathbf{M}_d)dS' \\ -\int_{T'}\nabla g_2\times(-\mathbf{J}_d)dS'-\frac{1}{2}\mathbf{n}_2\times(-\mathbf{J}_d)-\int_{T'}\nabla g_2\times(\mathbf{J}_c)dS'-\frac{1}{2}\mathbf{n}_2\times(\mathbf{J}_c) \end{pmatrix}, \tag{11}$$

where g_2 is the Green's function of infinity dielectric free-space. By operating with $\hat{\mathrm{n}}_2\times$ to (7), (8), and (9), N-EFIE$_2$ and N-MFIE$_2$ for the exterior equivalent problem can be derived:

On dielectric surface S_d:

$$\mathbf{n}_2\times\mathbf{E}_2^{inc}=\mathbf{n}_2\times\left(-\mathbf{E}_2^s\right) \tag{12}$$

$$\mathbf{n}_2\times\mathbf{H}_2^{inc}=\mathbf{n}_2\times\left(-\mathbf{H}_2^s\right). \tag{13}$$

On metallic surface S_c:

$$\mathbf{n}_2\times\mathbf{E}_2^{inc}=\mathbf{n}_2\times\left(-\mathbf{E}_2^s\right). \tag{14}$$

Note that $\hat{\mathrm{n}}_1=-\hat{\mathrm{n}}_2=\hat{\mathrm{n}}$. The negative sign is due to the direction of the unit normal vector pointing into the external medium.

A. EFIE-PMCHWT2 formulation for scattering problems in half-space

Using formulation (1)-(2), (7)-(9), the traditional PMCHWT combined with EFIE can be formed as follows:

$$\begin{cases}\text{T-EFIE}_2\\ \text{T-EFIE}_1-\text{T-EFIE}_2\\ \text{T-MFIE}_1-\text{T-MFIE}_2\end{cases}. \tag{15}$$

After it is expanded and tested with the RWG basis functions $\mathbf{f}_n$, a matrix equation will be:

$$\begin{bmatrix}\left[Z_{mn}^{J_cJ_c}\right] & \left[Z_{mn}^{J_cJ_d}\right] & \left[T_{mn}^{J_cM_d}\right]\\ \left[Z_{mn}^{J_dJ_c}\right] & \left[Z_{mn}^{J_dJ_d}\right] & \left[T_{mn}^{J_dM_d}\right]\\ \left[T_{mn}^{M_dJ_c}\right] & \left[T_{mn}^{M_dJ_d}\right] & \left[Y_{mn}^{M_dM_d}\right]\end{bmatrix}\begin{bmatrix}I_{cn}\\ I_{dn}\\ M_{dn}\end{bmatrix}=\begin{bmatrix}V_{cm}\\ V_{dm}\\ H_{dm}\end{bmatrix}. \tag{16}$$

In the equation, V_{cm}, V_{dm}, and H_{dm} is the incident field and reflect field summation. $\mathbf{J}_d=\sum_{n=1}^{N_d}I_{dn}\mathbf{f}_n$ 、

$\mathbf{J}_c = \sum_{n=1}^{N_c} I_{cn}\mathbf{f}_n$, $\mathbf{M}_d = \eta_0 \sum_{n=1}^{N_d} M_{dn}\mathbf{f}_n$, I_{dn}, I_{cn}, M_{dn} are the current coefficients needed to solve. To improve the condition number of the matrix, a coefficient adjustment is made to form the PMCHWT2 formulation:

$$\begin{bmatrix} \left[Z_{mn}^{J_cJ_c}\right] & \left[Z_{mn}^{J_cJ_d}\right] & \eta_1\left[T_{mn}^{J_cM_d}\right] \\ \left[Z_{mn}^{J_dJ_c}\right] & \left[Z_{mn}^{J_dJ_d}\right] & \eta_1\left[T_{mn}^{J_dM_d}\right] \\ \eta_1\left[T_{mn}^{M_dJ_c}\right] & \eta_1\left[T_{mn}^{M_dJ_d}\right] & \eta_1^2\left[Y_{mn}^{M_dM_d}\right] \end{bmatrix} \begin{bmatrix} I_{cn} \\ I_{dn} \\ M_{dn}/\eta_1 \end{bmatrix} = \begin{bmatrix} V_{cm} \\ V_{dm} \\ \eta_1 H_{dm} \end{bmatrix}, \tag{17}$$

where the $\eta_1 = \sqrt{\mu_1/\varepsilon_1}$.

B. JCFIE-JMCFIE formulation for scattering problems in half-space

In this paper, the novel integral equation JMCFIE [16] combined with JCFIE is extended to the half-space situation to realize accurate and fast solution of scattering from coated conducting targets. The JMCFIE formulation combined with JCFIE for half-space problems can be obtained by combining the T and N equations as the following form:

$$\begin{cases} -\dfrac{1}{\eta_2}\text{T-EFIE}_2 - \text{N-MFIE}_2 \\ \dfrac{1}{\eta_1}\text{T-EFIE}_1 - \dfrac{1}{\eta_2}\text{T-EFIE}_2 + \text{N-MFIE}_1 - \text{N-MFIE}_2 \\ \eta_1\text{T-MFIE}_1 - \eta_2\text{T-MFIE}_2 - \text{N-EFIE}_1 + \text{N-EFIE}_2 \end{cases}. \tag{18}$$

After expanding the unknowns $\mathbf{J}_c$, $\mathbf{J}_d$, and $\mathbf{M}_d$ in (18) with the RWG basis functions and using the Galerkin's method, a well-conditioned matrix equation will be:

$$\begin{bmatrix} \left[Z_{mn}^{J_cJ_c}\right] & \left[Z_{mn}^{J_cJ_d}\right] & \left[T_{mn}^{J_cM_d}\right] \\ \left[Z_{mn}^{J_dJ_c}\right] & \left[Z_{mn}^{J_dJ_d}\right] & \left[T_{mn}^{J_dM_d}\right] \\ \left[T_{mn}^{M_dJ_c}\right] & \left[T_{mn}^{M_dJ_d}\right] & \left[Y_{mn}^{M_dM_d}\right] \end{bmatrix} \begin{bmatrix} I_{cn} \\ I_{dn} \\ M_{dn} \end{bmatrix} = \begin{bmatrix} F_{ecm} \\ F_{edm} \\ F_{hdm} \end{bmatrix}. \tag{19}$$

$$\begin{aligned} Z_{mn}^{J_dJ_d} = {} & \frac{1}{\eta_1} j\omega\mu_1 \left\langle \int_{T'} \bar{\bar{\mathbf{K}}}^A \cdot \mathbf{f}_n dS', \mathbf{f}_m \right\rangle + \frac{1}{\eta_1 j\omega\varepsilon_1} \left\langle \int_{T'} K^{\phi e} \nabla_s' \cdot \mathbf{f}_n dS', \nabla \cdot \mathbf{f}_m \right\rangle \\ & - \left\langle \boldsymbol{n} \times \int_{T'} \bar{\bar{\mathbf{G}}}^{HJ} \cdot \mathbf{f}_n dS', \mathbf{f}_m \right\rangle + \frac{1}{2}\langle \mathbf{f}_n \cdot \mathbf{f}_m \rangle \\ & + \frac{1}{\eta_2} j\omega\mu_2 \left\langle \int_{T'} g_2 \cdot \mathbf{f}_n dS', \mathbf{f}_m \right\rangle + \frac{1}{\eta_2 j\omega\varepsilon_2} \left\langle \int_{T'} g_2 \nabla_s' \cdot \mathbf{f}_n dS', \nabla \cdot \mathbf{f}_m \right\rangle \\ & + \left\langle \boldsymbol{n} \times \int_{T'} \nabla g_2 \times \mathbf{f}_n dS', \mathbf{f}_m \right\rangle + \frac{1}{2}\langle \mathbf{f}_n \cdot \mathbf{f}_m \rangle \end{aligned} \tag{20}$$

$$\begin{aligned} Z_{mn}^{J_dJ_c} = {} & -\frac{1}{\eta_2} j\omega\mu_2 \left\langle \int_{T'} g_2 \cdot \mathbf{f}_n dS', \mathbf{f}_m \right\rangle - \frac{1}{\eta_2 j\omega\varepsilon_2} \left\langle \int_{T'} g_2 \nabla_s' \cdot \mathbf{f}_n dS', \nabla \cdot \mathbf{f}_m \right\rangle \\ & - \left\langle \boldsymbol{n} \times \int_{T'} \nabla g_2 \times \mathbf{f}_n dS', \mathbf{f}_m \right\rangle - \frac{1}{2}\langle \mathbf{f}_n \cdot \mathbf{f}_m \rangle \end{aligned} \tag{21}$$

$$\begin{aligned} T_{mn}^{J_dM_d} = {} & j\omega\varepsilon_1 \left\langle \boldsymbol{n} \times \int_{T'} \bar{\bar{\mathbf{K}}}^F \cdot \mathbf{f}_n dS', \mathbf{f}_m \right\rangle - \frac{1}{j\omega\mu_1} \left\langle \boldsymbol{n} \times \nabla \int_{T'} K^{\phi m} \nabla_s' \cdot \mathbf{f}_n dS', \mathbf{f}_m \right\rangle \\ & - \frac{1}{\eta_1} \left\langle \int_{T'} \bar{\bar{\mathbf{G}}}^{EM} \cdot \mathbf{f}_n dS', \mathbf{f}_m \right\rangle + \frac{1}{2\eta_1} \langle \mathbf{n} \times \mathbf{f}_n, \mathbf{f}_m \rangle \\ & - j\omega\varepsilon_2 \left\langle \boldsymbol{n} \times \int_{T'} g_2 \cdot \mathbf{f}_n dS', \mathbf{f}_m \right\rangle + \frac{1}{j\omega\mu_2} \left\langle \boldsymbol{n} \times \nabla \int_{T'} g_2 \nabla_s' \cdot \mathbf{f}_n dS', \mathbf{f}_m \right\rangle \\ & + \frac{1}{\eta_2} \left\langle \int_{T'} \nabla g_2 \times \mathbf{f}_n dS', \mathbf{f}_m \right\rangle - \frac{1}{2\eta_2} \langle \mathbf{n} \times \mathbf{f}_n, \mathbf{f}_m \rangle \end{aligned} \tag{22}$$

$$\begin{aligned} Z_{mn}^{J_cJ_d} = {} & \frac{1}{\eta_2} j\omega\mu_2 \left\langle \int_{T'} g_2 \cdot \mathbf{f}_n dS', \mathbf{f}_m \right\rangle + \frac{1}{\eta_2 j\omega\varepsilon_2} \left\langle \int_{T'} g_2 \nabla_s' \cdot \mathbf{f}_n dS', \nabla \cdot \mathbf{f}_m \right\rangle \\ & + \left\langle \boldsymbol{n} \times \int_{T'} \nabla g_2 \times \mathbf{f}_n dS', \mathbf{f}_m \right\rangle + \frac{1}{2} \langle \mathbf{f}_n \cdot \mathbf{f}_m \rangle \end{aligned} \tag{23}$$

$$\begin{aligned} Z_{mn}^{J_cJ_c} = {} & -\frac{1}{\eta_2} j\omega\mu_2 \left\langle \int_{T'} g_2 \cdot \mathbf{f}_n dS', \mathbf{f}_m \right\rangle - \frac{1}{\eta_2 j\omega\varepsilon_2} \left\langle \int_{T'} g_2 \nabla_s' \cdot \mathbf{f}_n dS', \nabla \cdot \mathbf{f}_m \right\rangle \\ & - \left\langle \boldsymbol{n} \times \int_{T'} \nabla g_2 \times \mathbf{f}_n dS', \mathbf{f}_m \right\rangle - \frac{1}{2} \langle \mathbf{f}_n \cdot \mathbf{f}_m \rangle \end{aligned} \tag{24}$$

$$\begin{aligned} T_{mn}^{J_cM_d} = {} & -j\omega\varepsilon_2 \left\langle \boldsymbol{n} \times \int_{T'} g_2 \cdot \mathbf{f}_n dS', \mathbf{f}_m \right\rangle + \frac{1}{j\omega\mu_2} \left\langle \boldsymbol{n} \times \nabla \int_{T'} g_2 \nabla_s' \cdot \mathbf{f}_n dS', \mathbf{f}_m \right\rangle \\ & + \frac{1}{\eta_2} \left\langle \int_{T'} \nabla g_2 \times \mathbf{f}_n dS', \mathbf{f}_m \right\rangle - \frac{1}{2\eta_2} \langle \mathbf{n} \times \mathbf{f}_n, \mathbf{f}_m \rangle \end{aligned} \tag{25}$$

$$\begin{aligned} T_{mn}^{M_dJ_d} = {} & -j\omega\mu_1 \left\langle \boldsymbol{n} \times \int_{T'} \bar{\bar{\mathbf{K}}}^A \cdot \mathbf{f}_n dS', \mathbf{f}_m \right\rangle + \frac{1}{j\omega\varepsilon_1} \left\langle \boldsymbol{n} \times \nabla \int_{T'} K^{\phi e} \nabla_s' \cdot \mathbf{f}_n dS', \mathbf{f}_m \right\rangle \\ & - \eta_1 \left\langle \int_{T'} \bar{\bar{\mathbf{G}}}^{HJ} \cdot \mathbf{f}_n dS', \mathbf{f}_m \right\rangle - \frac{\eta_1}{2} \langle \mathbf{n} \times \mathbf{f}_n, \mathbf{f}_m \rangle \\ & + j\omega\mu_2 \left\langle \boldsymbol{n} \times \int_{T'} g_2 \cdot \mathbf{f}_n dS', \mathbf{f}_m \right\rangle - \frac{1}{j\omega\varepsilon_2} \left\langle \boldsymbol{n} \times \nabla \int_{T'} g_2 \nabla_s' \cdot \mathbf{f}_n dS', \mathbf{f}_m \right\rangle \\ & - \eta_2 \left\langle \int_{T'} \nabla g_2 \times \mathbf{f}_n dS', \mathbf{f}_m \right\rangle + \frac{\eta_2}{2} \langle \mathbf{n} \times \mathbf{f}_n, \mathbf{f}_m \rangle \end{aligned} \tag{26}$$

$$\begin{aligned} T_{mn}^{M_dJ_c} = {} & -j\omega\mu_2 \left\langle \boldsymbol{n} \times \int_{T'} g_2 \cdot \mathbf{f}_n dS', \mathbf{f}_m \right\rangle + \frac{1}{j\omega\varepsilon_2} \left\langle \boldsymbol{n} \times \nabla \int_{T'} g_2 \nabla_s' \cdot \mathbf{f}_n dS', \mathbf{f}_m \right\rangle \\ & + \eta_2 \left\langle \int_{T'} \nabla g_2 \times \mathbf{f}_n dS', \mathbf{f}_m \right\rangle - \frac{\eta_2}{2} \langle \mathbf{n} \times \mathbf{f}_n, \mathbf{f}_m \rangle \end{aligned} \tag{27}$$

$$\begin{aligned} Y_{mn}^{M_dM_d} = {} & \eta_1 j\omega\varepsilon_1 \left\langle \int_{T'} \bar{\bar{\mathbf{K}}}^F \cdot \mathbf{f}_n dS', \mathbf{f}_m \right\rangle + \frac{\eta_1}{j\omega\mu_1} \left\langle \int_{T'} K^{\phi m} \nabla_s' \cdot \mathbf{f}_n dS', \nabla \cdot \mathbf{f}_m \right\rangle \\ & + \left\langle \boldsymbol{n} \times \int_{T'} \bar{\bar{\mathbf{G}}}^{EM} \cdot \mathbf{f}_n dS', \mathbf{f}_m \right\rangle + \frac{1}{2} \langle \mathbf{f}_n \cdot \mathbf{f}_m \rangle \\ & + \eta_2 j\omega\varepsilon_2 \left\langle \int_{T'} g_2 \cdot \mathbf{f}_n dS', \mathbf{f}_m \right\rangle + \frac{\eta_2}{j\omega\mu_2} \left\langle \int_{T'} g_2 \nabla_s' \cdot \mathbf{f}_n dS', \nabla \cdot \mathbf{f}_m \right\rangle \\ & + \left\langle \boldsymbol{n} \times \int_{T'} \nabla g_2 \times \mathbf{f}_n dS', \mathbf{f}_m \right\rangle + \frac{1}{2} \langle \mathbf{f}_n \cdot \mathbf{f}_m \rangle \end{aligned} \tag{28}$$

$$F_{ecm} = \left\langle \left(-\frac{1}{\eta_2}\mathbf{E}_2^{inc} + \hat{\mathrm{n}}\times\mathbf{H}_2^{inc} \right), \mathbf{f}_m \right\rangle \quad (29)$$

$$F_{edm} = \left\langle \left(\frac{1}{\eta_1}\mathbf{E}_1^{inc} - \frac{1}{\eta_2}\mathbf{E}_2^{inc} + \hat{\mathrm{n}}\times\mathbf{H}_1^{inc} + \hat{\mathrm{n}}\times\mathbf{H}_2^{inc} \right), \mathbf{f}_m \right\rangle \quad (30)$$

$$F_{hdm} = \left\langle \left(\eta_1\mathbf{H}_1^{inc} - \eta_2\mathbf{H}_2^{inc} - \hat{\mathrm{n}}\times\mathbf{E}_1^{inc} - \hat{\mathrm{n}}\times\mathbf{E}_2^{inc} \right), \mathbf{f}_m \right\rangle. \quad (31)$$

It's obvious that the JCFIE-JMCFIE formulation contains well-tested identity operators. The impedance matrix of JCFIE-JMCFIE is well-conditioned since the well-tested identity operators lead to diagonally-dominant matrices. This is an essential requirement for a formulation with a high convergence rate. This explains why the developed JCFIE-JMCFIE formulation leads to a better conditioned matrix equation than the traditional EFIE-PMCHWT formulations and hence gives more rapidly converging iterative solutions. Finally, the linear system of equations in (19) can be solved by the FGMRES method [21-24] using half-space MLFMA to accelerate the matrix-vector products [8].

III. NUMERICAL EXAMPLES

In this section, we show some numerical results for the electromagnetic characteristics of a conducting body coated with dielectric materials in half-space that illustrate the accuracy and effectiveness of the proposed JCFIE-JMCFIE formulation. The JCFIE-JMCFIE linear systems based on the RWG basis functions are solved with MLFMA accelerated Krylov iterative methods. All numerical experiments are performed on a Pentium 4 with 2.9 GHz CPU and 2GB RAM in single precision. In this paper, the inner-outer FGMRES [21-24] is used as the iterative solver for the JCFIE-JMCFIE and EFIE-PMCHWT2 formulation to accelerate the convergence rate compared with GMRES. In the flowing examples, the inner and outer restart numbers of FGMRES are both 10. The stop precision of restarted GMRES is denoted to be 1.E-4. In the FGMRES algorithm, the stop precision for the inner and outer iteration is 1.E-2, 1.E-4, respectively. Additional details and comments on the implementation are given as follows:

· Zero vector is taken as an initial approximate solution for all examples and all systems in each example.

· The iteration process is terminated when the normalized backward error is reduced by 10^{-4} for all the examples.

At first, the developed formulations are verified by the conducting body coated with dielectric materials in free-space. The first example is a metallic sphere covered with dielectric material in free-space as shown in Fig. 2(a). The metallic sphere's radius is $a_1 = 0.3423\lambda_0$ (λ_0 is the wavelength in free-space). The thickness of the coated dielectric is $a_2 = 0.1017\lambda_0$ and the relative permittivity is with $\varepsilon_r = 4$. The incident angles of plane wave are $\theta_i = 180^\circ$ and $\phi_i = 180^\circ$ at a frequency of $f = 300MHz$. Fig. 2(b) gives the $\theta\theta$ co-polarized bi-static RCS for the above free-space coated metallic sphere solved by the JCFIE-JMCFIE, EFIE-PMCHWT2, and Mie, respectively. The scattering angle is $0^\circ \le \theta_s \le 180^\circ, \phi_s = 0^\circ$. MLFMA with 2 levels is used to accelerate the matrix-vector products. The coated metallic sphere is discretized with 3240 triangular patches leading to 7720 unknowns. It can be found that the results using the JCFIE-JMCFIE, EFIE-PMCHWT2 method are in good agreement with the Mie series solution. Figure 3 shows the convergence rates of the JCFIE-JMCFIE and EFIE-PMCHWT2 formulations solved by GMRES method for the above example. From Fig. 3, it can be found that the EFIE-PMCHWT method does not reach convergence after 700 iteration steps. However, the JCFIE-JMCFIE can reach convergence in 100 iteration steps. It can be concluded that the condition number of the proposed JCFIE-JMCFIE is much better than the EFIE-PMCHWT2.

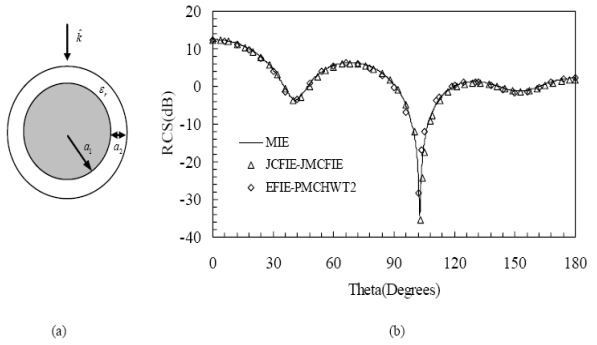

Fig. 2. (a) Geometry of a metallic sphere covered with dielectric material in free-space. (b) The co-

polarized bi-static RCS ($\theta\theta$) of a metallic sphere covered with dielectric material for $0^\circ \le \theta_s \le 180^\circ, \phi_s = 0^\circ$ at 300MHz.

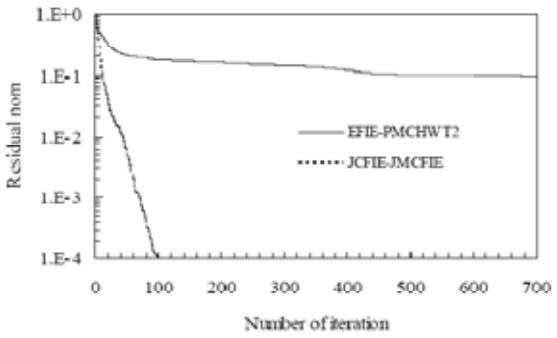

Fig. 3. The convergence history of JCFIE-JMCFIE, EFIE-PMCHWT2 solved with FGMRES for a metallic sphere covered with dielectric material in free-space at 300MHz.

Next, we extended the JCFIE-JMCFIE method to analyze the half-space problems to verify the accuracy and efficiency of the JCFIE-JMCFIE. As shown in Fig. 4(a), we consider a metallic sphere covered with spherical dielectric material situated 0.3577m above the lossy half space characterized by $\varepsilon_{half} = 5.0 - j0.2$ and $\mu_{half} = 1.0$. The metallic sphere's radius is $a_1 = 0.3423\lambda_0$. The thickness of the coated dielectric material is $a_2 = 0.1017\lambda_0$ and the relative permittivity is with $\varepsilon_r = 4$. The incident angles of plane wave are $\theta_i = 180^\circ$ and $\phi_i = 180^\circ$ at $f = 300MHz$. The metallic sphere coated with spherical dielectric is, also, discretized with 3240 triangular patches leading to 7720 unknowns. Figure 4(b) gives the bi-static RCS for the above half-space metallic sphere coated with spherical dielectric solved by the JCFIE-JMCFIE and EFIE-PMCHWT2, respectively. The scattering angle is $0^\circ \le \theta_s \le 90^\circ, \phi_s = 0^\circ$. The two levels MLFMA are used to accelerate the matrix-vector products. The simulated results obtained from the method of moment for bodies of revolution (BORMoM) and FEKO software are given to compare to them from JCFIE-JMCFIE and EFIE-PMCHWT2. In the BORMoM computation, the coated metallic sphere is discretized along the generating arc leading to 114 unknowns. The order of Fourier mode is 10 and the computation time is 2308.3 seconds in BORMoM. From Fig. 4(b), the results of JCFIE-JMCFIE and EFIE-PMCHWT2 agree well with the BORMoM and FEKO results. Furthermore, Fig. 5 gives the convergence rates of the JCFIE-JMCFIE and EFIE-PMCHWT2 formulations solved by the FGMRES method for the above half-space example. It is obvious that the application of the novel integral equation JCFIE-JMCFIE greatly accelerates the convergence rate compared with the EFIE-PMCHWT2 formulation.

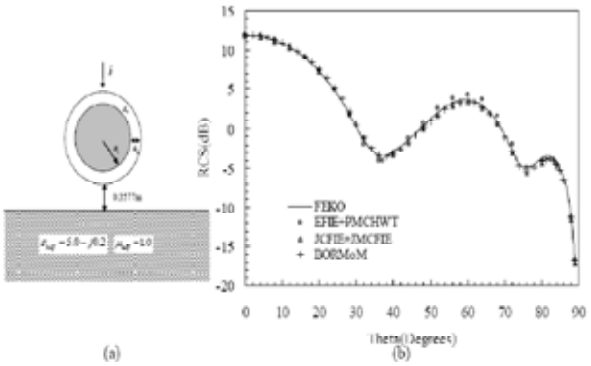

Fig. 4. (a) Geometry of a metallic sphere covered with spherical dielectric material situated above the lossy half space. (b) The co-polarized bi-static RCS ($\theta\theta$) of a metallic sphere covered with spherical dielectric material situated above the lossy half space for $0^\circ \le \theta_s \le 90^\circ, \phi_s = 0^\circ$ at 300MHz.

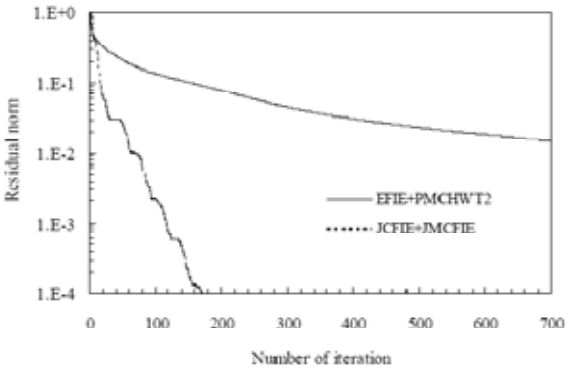

Fig. 5. The convergence history of JCFIE-JMCFIE, EFIE-PMCHWT2 solved with FGMRES for a metallic sphere covered with spherical dielectric material situated above the lossy half space at 300MHz.

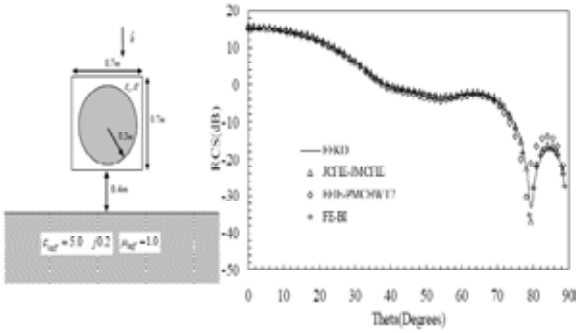

Fig. 6. (a) Geometry of a metallic sphere covered with cubic dielectric material situated above the lossy half space. (b) The co-polarized bi-static RCS ($\theta\theta$) of a metallic sphere covered with cubic dielectric material situated above the lossy half space for $0^\circ \le \theta_s \le 90^\circ, \phi_s = 0^\circ$ at 300MHz.

The another example shown in Fig. 6(a) is a metallic sphere covered with cubic dielectric situated 0.4 m above the lossy half space characterized by $\varepsilon_{half} = 5.0 - j0.2$ and $\mu_{half} = 1.0$. The metallic sphere's radius is 0.3m. The coated cubic dielectric is lossy. The conductivity and relative permittivity of dielectric are $\sigma = 0.001$s/m and $\varepsilon_r = 4$, respectively. The incident angles of plane wave are $\theta_i = 180^\circ$ and $\phi_i = 180^\circ$ at a frequency of $f = 300MHz$. The metallic sphere coated with spherical dielectric is also discretized with triangular patches leading to 10896 unknowns. Figure 6(b) gives the bi-static RCS for the above half-space metallic sphere coated with cubic dielectric solved by the JCFIE-JMCFIE, EFIE-PMCHWT2 finite element-boundary integral method (FE-BI) and FEKO software, respectively. The scattering angle is $0^\circ \le \theta_s \le 90^\circ, \phi_s = 0^\circ$. MLFMA with 2 levels is used to accelerate the matrix-vector products. In the FE-BI computation, the number of unknowns is 23651 and the computation time is 432.2 seconds. From Figure 6(b), it can be found that the results of JCFIE-JMCFIE are in good agreement with them obtained from EFIE-PMCHWT2, FE-BI and FEKO. Figure 7, also, shows the convergence rates of the JCFIE-JMCFIE and EFIE-PMCHWT2 formulations solved by FGMRES method for the last half-space example. It can be found that the proposed JCFIE-JMCFIE method only needs 139 iteration steps to reach convergence while the EFIE-PMCHWT2 method can not converge after 700 iteration steps.

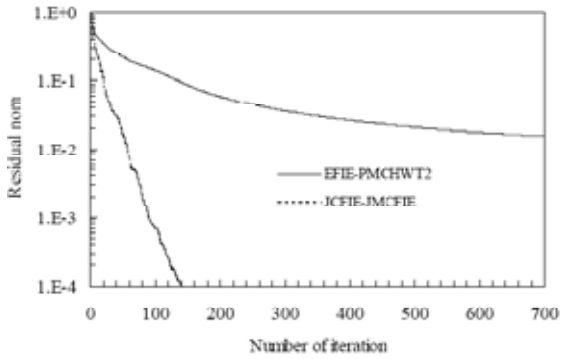

Fig. 7. The convergence history of JCFIE-JMCFIE, EFIE-PMCHWT2 solved with FGMRES for a metallic sphere covered with cubic dielectric material situated above the lossy half space at 300MHz.

In order to further investigate the performance of the proposed JCFIE-JMCFIE method, the above half-space metallic sphere coated with spherical dielectric material with the larger dielectric constants is considered. Figure 8 gives the co-polarized bi-static RCS of a metallic sphere covered with spherical dielectric material with $\varepsilon_r = 10$ and $\varepsilon_r = 12$ situated above the lossy half space solved by the JCFIE-JMCFIE. The simulated results obtained from BORMoM are given to compare to them from JCFIE-JMCFIE. In the BORMoM computation, the coated metallic spheres with $\varepsilon_r = 10$ and $\varepsilon_r = 12$ are both discretized along the generating arc leading to 114 unknowns. The order of Fourier mode is 20 and the computation time of BORMoM is 5128.3 seconds and 6340.1 seconds for $\varepsilon_r = 10$ and $\varepsilon_r = 12$ cases, respectively. The scattering angle is $0^\circ \le \theta_s \le 90^\circ, \phi_s = 0^\circ$. The two levels MLFMA is used to accelerate the matrix-vector products. Figure 9 and Fig. 10 give the convergence rates of the JCFIE-JMCFIE and EFIE-PMCHWT2 formulations solved by FGMRES method for the above half-space example with $\varepsilon_r = 10$ and $\varepsilon_r = 12$, respectively. It can be found that the JCFIE-JMCFIE method only needs 713 iteration steps to reach the convergence for the $\varepsilon_r = 10$ example, while the EFIE-PMCHWT2 method can only converge to the error of 0.1 after 2000 iteration.

For the $\varepsilon_r = 12$ example, the JCFIE-JMCFIE method can reach convergence after 5581 iteration steps, while the EFIE-PMCHWT2 method only converge to the error of 0.1 after 10000 iteration steps. This demonstrates the efficiency of the proposed JCFIE-JMCFIE method for the half-space metallic sphere coated with larger dielectric constants dielectric material.

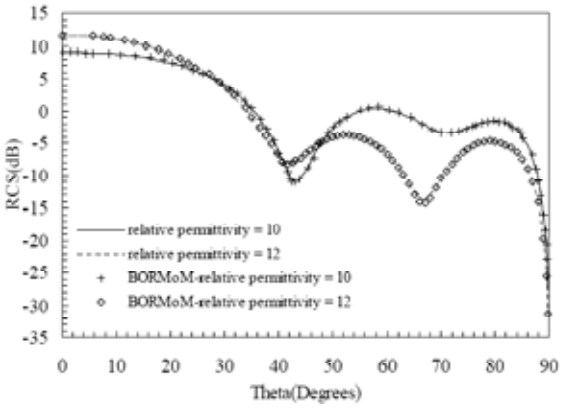

Fig. 8. The co-polarized bi-static RCS ($\theta\theta$) of a metallic sphere covered with spherical dielectric material with $\varepsilon_r = 10$ and $\varepsilon_r = 12$ situated above the lossy half space for $0^\circ \le \theta_s \le 90^\circ, \phi_s = 0^\circ$ at 300MHz.

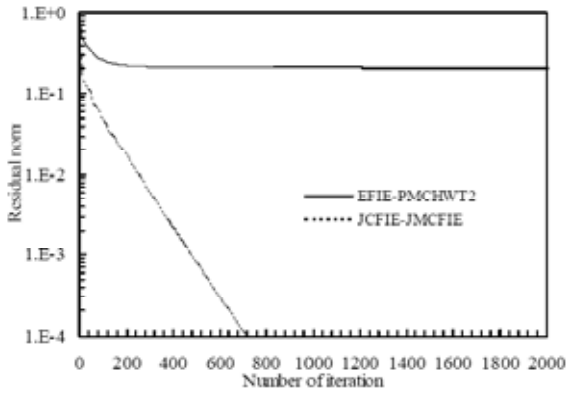

Fig. 9. The convergence history of JCFIE-JMCFIE, EFIE-PMCHWT2 solved with FGMRES for a metallic sphere covered with spherical dielectric material with $\varepsilon_r = 10$ situated above the lossy half space at 300MHz.

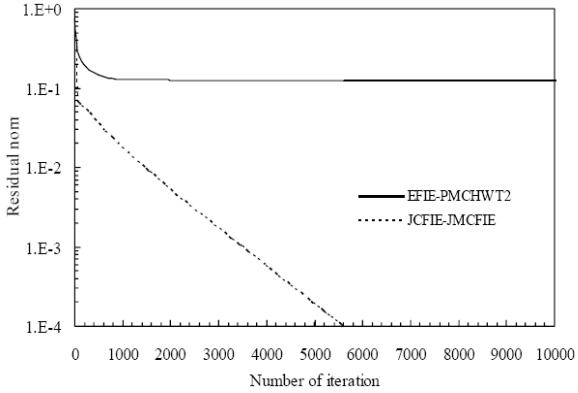

Fig. 10. The convergence history of JCFIE-JMCFIE, EFIE-PMCHWT2 solved with FGMRES for a metallic sphere covered with spherical dielectric material with $\varepsilon_r = 12$ situated above the lossy half space at 300MHz.

Figure 11 gives the convergence rates of the JCFIE-JMCFIE and EFIE-PMCHWT2 formulations solved by the FGMRES method for the above half-space metallic sphere covered with spherical dielectric material with $\varepsilon_r = 4$ in Figure 4(a). The metallic sphere coated with spherical dielectric is also discretized with triangular patches leading to 37302 unknowns. Due to the limit of computer memory (2GB RAM), larger problems (>40000) can not be computed. Furthermore, compared with the free-space MLFMA, aggregation and disaggregation for the image groups as well as calculations of the translation operator between image and observation group centers are additionally required during implementing half-space MLFMA in JCFIE-JMCFIE. As a result, the storage and CPU of half-space MLFMA are approximately twice that of a free-space MLFMA, due to the extra set of image clusters. From Figure 11, it can be found that the proposed JCFIE-JMCFIE method only needs 167 iteration steps to reach convergence while the EFIE-PMCHWT2 method can only converge to the error of 0.6 after 700 iteration steps.

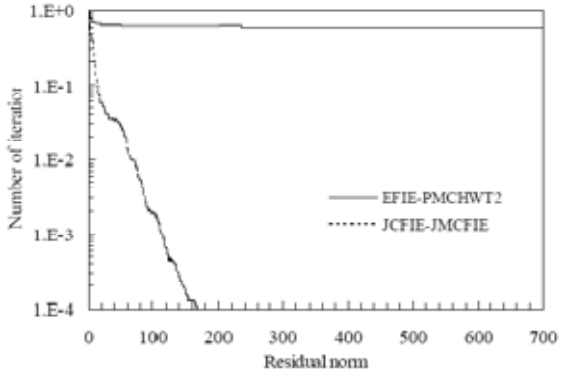

Fig. 11. The convergence history of JCFIE-JMCFIE, EFIE-PMCHWT2 solved with FGMRES for a metallic sphere covered with spherical dielectric material with situated above the lossy half space at 300MHz. The number of unknown is 37302.

Tables 1-3 list the iteration steps and computation time of the JCFIE-JMCFIE and EFIE+PMCHWT2 solved by FGMRES for above three examples where * refers to no convergence after maximum 20000 iterations. When compared in terms of solution time, the JCFIE-JMCFIE have a gain over the EFIE+PMCHWT2 by a factor of more than 160 on the first free-space example, 32.2 on the second half-space metallic sphere example coated with spherical dielectric, 61.9 on the third half-space metallic sphere example coated with cubic dielectric. It can be found that the JCFIE-JMCFIE reduces the computation time significantly while it maintains high accuracy when compared with the traditional EFIE+PMCHWT2.

IV. CONCLUSION

In this paper, a well-conditioned coupled surface integral equation called JCFIE-JMCFIE is proposed for the analysis of electromagnetic scattering from coated targets above a lossy half-space. The coupled formulation can lead to a well tested system with the RWG basis functions and Galerkin's method. To efficiently analyze electrically large scattering problems in half-space, the half-space MLFMA is implemented to reduce the computational complexity and memory requirement. The inner-outer FGMRES is used as the iterative solver to further enhance the convergence rate. Numerical results are demonstrated to validate the proposed method and show the accuracy and high efficiency compared with the traditional EFIE-PMCHWT2 method. Further investigations deserve to be undertaken to study the parallelization of the proposed JCFIE-JMCFIE with MLFMA.

Table 1: Comparison of the iteration steps and computation time of JCFIE-JMCFIE and EFIE-PMCHWT2 for the metallic sphere coated with spherical dielectric on free space

	Unknowns	Iteration steps	Computation time(s)
EFIE-PMCHWT2	7720	*	>20000
JCFIE-JMCFIE	7720	100	121.8

Table 2: Comparison of the iteration steps and computation time of JCFIE-JMCFIE and EFIE-PMCHWT2 for the metallic sphere coated with spherical dielectric situated 0.3577m above the lossy half space

	Unknowns	Iteration steps	Computation time(s)
EFIE-PMCHWT2	7720	9082	7054.16
JCFIE-JMCFIE	7720	173	219.28

Table 3: Comparison of the iteration steps and computation time of JCFIE-JMCFIE and EFIE-PMCHWT2 for the metallic sphere coated with cubic dielectric situated 0.4m above the lossy half space

	Unknowns	Iteration steps	Computation time(s)
EFIE-PMCHWT2	10896	16024	13559.17
JCFIE-JMCFIE	10896	139	219.28

ACKNOWLEDGMENT

The authors would like to thank the support of Natural Science Foundation of China under Contract Number 60701005, 60871013, Natural Science Foundation of Jangsu under Contact Number BK2009387, NUST Research Funding under Contract Number 2010ZYTS026, and the Research Fund for the Doctoral Program of Higher Education under Contract Number 20070288043.

REFERENCES

[1] N. Geng, A. Sullivan, and L. Carin, "Multilevel fastmultipole algorithm for scattering from conducting targets above or embedded in a lossy half space," *IEEE Trans. Geosci. Remote Sensing*, vol. 38, no. 4, pp. 1561-1573, July 2000.

[2] Z. J. Liu, J. Q. He, Y. J. Xie, A. Sullivan, and L. Carin, "Multi-level fast multipole algorithm for general targets on a half-space interface," *IEEE Trans. on Antenna and Propagation*, vol. 50, no. 12, pp. 1838-1849, Dec. 2002.

[3] L. Li, J. Q. He, Z. J. Liu, X. L. Dong, and L. Carin, "MLFMA analysis of scattering from multiple targets in the presence of a half-space," *IEEE Trans. on Antenna and Propagation*, vol. 51, no. 4, pp. 810-819, Apr. 2003.

[4] N. Geng, A. Sullivan, and L. Carin, "Fast multipole method for scattering from an arbitrary PEC target above or buried in a lossy half space," *IEEE Trans. on Antenna and Propagation*, vol. 49, no. 5, pp. 740-748, May 2001.

[5] D. Z. Ding, R. S. Chen, and Z. H. Fan, "Application of two-step spectral preconditioning technique for electromagnetic scattering in half-space," *Progress In Electromagnetics Research*, PIER 94, pp. 383-402, 2009.

[6] R. F. Harrington, *Field Computation by Moment Methods*, Malabar, Fla.: R. E. Krieger, 1968.

[7] S. M. Rao, D. R. Wilton, and A. W. Glisson, "Electromagnetic scattering by surfaces of arbitrary shape," *IEEE Trans. on Antenna and Propagation*, vol. 30, no. 3, pp. 409-418, 1982.

[8] W. C. Chew, J. M. Jin, E. Midielssen, and J. M. Song, *Fast and Efficient Algorithms in Computational Electromagnetics*. Boston, MA: Artech House, 2001.

[9] D. Z. Ding, R. S. Chen, and Z. H. Fan, "An Efficient SAI Preconditioning Technique For Higher Order Hierarchical MLFMM Implementation", *Progress In Electromagnetics Research*, PIER 88, pp. 255-273, 2008.

[10] D. Z. Ding, R. S. Chen, Z. H. Fan and P.L. Rui, "A Novel Hierarchical Two-level Spectral Preconditioning Technique for Multilevel Fast Multipole Analysis of Electromagnetic Wave Scattering," *IEEE Trans. on Antenna and Propagation*, vol. 56, no. 4, pp. 1122-1132, April 2008.

[11] Ö. Ergül, and L. Gürel, "Linear-linear Basis Functions for MLFMA Solutions of Magnetic-Field and Combined-Field Integral Equations," *IEEE Trans. on Antenna and Propagation*, vol. 55, no. 4, pp. 1103-1110, April 2007.

[12] R. M. Shubair, and Y. L. Chow, "A simple and accurate complex image interpretation of vertical antennas present in contiguous dielectric half-spaces," *IEEE Trans. on Antenna and Propagation*, vol. 41, pp. 806-812, June 1993.

[13] M. I. Aksun, "A robust approach for the derivation of closed-form Green's functions," *IEEE Trans. Microwave Theory and Technique*, vol. 44, pp. 651–658, May 1996.

[14] N. A. Geng, Sullivan, and L. Carin, "Fast multipole method for scattering from 3D PEC targets situated in a half-space environment," *Microw. Opt. Technol. Lett.*, vol. 21, pp. 399-405, June 1999.

[15] X. Q. Sheng, J. M. Jin, J. M. Song, W. C. Chew, and C. C. Lu, "Solution of Combined-Field Integral Equation Using Multilevel Fast Multipole Algorithm for Scattering by Homogeneous Bodies," *IEEE Trans. Antennas Propagat.*, vol. 46, no. 11, pp. 1718 -1726, November 1998.

[16] P. Ylä-Oijala and Matti Taskinen, "Application of Combined Field Integral Equation for Electromagnetic Scattering by Dielectric and Composite Objects," *IEEE Trans. Antennas Propagat.*, vol. 53, no. 3, pp. 1168–1173, March 2005.

[17] P. Ylä-Oijala, M. Taskinen, and S. Järvenpää, "Analysis of surface integral equations in electromagnetic scattering and radiation problems," *Engineering Analysis with Boundary Elements*, vol. 32, pp. 196-209, 2008.

[18] S. M. Rao, C. C. Cha, R. L. Cravey, and D. L. Wilkes, "Electromagnetic Scattering from Arbitrary Shaped Conducting Bodies Coated with Lossy Materials of Arbitrary Thickness," *IEEE Trans. Antennas Propagat.*, vol. 39, no. 5, pp. 627-631, May 1991.

[19] Ö. Ergül and L. Gürel, "Comparison of Integral-Equation Formulations the Fast and Accurate Solution of Scattering Problems Involving Dielectric Objects with the Multilevel Fast Multipole Algorithm," *IEEE Trans. Antennas Propagat.*, vol. 57, no. 1, pp. 176-187, Jan. 2009.

[20] Ö. Ergül and L. Gürel, "Discretization Error Due to the Identity Operator in Surface Integral Equations," *Computer Physics Communications,* vol. 180, pp. 1746 – 1752, 2009.

[21] Y. Saad, *Iterative methods for sparse linear systems*, PWS Publishing Company, 1996.

[22] Y. Saad and M. H. Schultz, "GMRES: A generalized minimal residual algorithm for solving nonsymmetric linear systems," *SIAM J Sci Statist Comput*, vol. 7, pp. 856 – 869, 1986.

[23] D. Z. Ding, R. S. Chen, Z. H. Fan, Edward K. N. Yung, and C.H. Chan, "Fast analysis of electromagnetic scattering of 3D dielectric bodies by use of the loose GMRES-FFT method," *International Journal of Electronics*, vol. 92, no. 7, pp. 401-415, July 2005.

[24] D. Z. Ding, R. S. Chen, D. X. Wang, W. Zhuang, and Edward K. N. Yung, "Application of the inner-outer flexible GMRES-FFT method to the analysis of scattering and radiation by cavity-backed patch antennas and arrays," *International Journal of Electronics*, vol. 92, no. 11, pp. 645-659, Nov. 2005.

[25] K. A. Michalski and D. Zheng, "Electromagnetic scattering and radiation by surfaces of arbitrary shape in layered media, Parts I and II," *IEEE Trans. on Antenna and Propagation*, vol. 38, pp. 335-352, Mar. 1990.

Dazhi Ding was born in Jiangsu, the People's Republic of China in 1979. He received the B.S. and Ph.D. degrees in Electromagnetic Field and Microwave Technique from Nanjing University of Science and Technology (NUST), Nanjing, China, in 2002 and 2007, respectively. During 2005, he was with the Center of Wireless Communication in the City University of Hong Kong, Kowloon, as a Research Assistant. He is currently an Associate Professor with the Electronic Engineering of NJUST. He is the author or coauthor of over 30 technical papers. His current research interests include computational electromagnetics, electromagnetic scattering, and radiation.

Jinmin Ge was born in Shandong Province, China, in 1987. She received the B.S. degree in Electrical Engineering from Huaiyin Normal University, Huaiyin, China, in 2007. She received the Master's degree in Nanjing University of Science and Technology (NUST), Nanjing, China, in 2009. Her current research interests include computational electromagnetics, antennas, and electromagnetic scattering, and propagation.

Rushan Chen was born in Jiangsu, China in 1965. He received the B.Sc. and M.Sc. degrees from Southeast University, Nanjing, China, in 1987 and 1990, respectively, and the Ph.D. degree in from Electronic Engineering from City University of Hong Kong, Kowloon, in 2001. In September 1999, he was promoted to Full Professor. His research interests mainly include microwave/millimeter-wave systems, measurements, antenna, RF-integrated circuits, and computational electromagnetics. He is the recipient of the Foundation for China Distinguished Young Investigators presented by the National Science Foundation (NSF) of China in 2003. In 2008, he became a Chang-Jiang Professor under the Cheung Kong Scholar Program awarded by the Ministry of Education, China.

Robust Beamforming Technique with Sidelobe Suppression Using Sparse Constraint on Beampattern

Ying Zhang [1], Huapeng Zhao [1], Joni Polili Lie [2], Boon Poh Ng [1], and Qun Wan [3]

[1] School of Electrical and Electronic Engineering
Nanyang Technological University, Singapore, 639798, Singapore
zhangy@ntu.edu.sg, zh0044ng@ntu.edu.sg, ebpng@ntu.edu.sg

[2] Temasek Laboratories@Nanyang Technological University
Nanyang Technological University, Singapore, 639798, Singapore
JoniLie@ntu.edu.sg

[3] Department of Electronic Engineering
University of Electronic Science and Technology of China, Chengdu, 610066, China
wanqun@uestc.edu.cn

Abstract ─ In this paper, we propose two beamforming algorithms which impose sparse constraint on beampattern to suppress the sidelobe level and enhance robustness of the beamformer against steering vector error. The sparse constraint is given by an l_p-norm, where $p \leq 2$ holds. It is shown that the proposed algorithms can be solved using iterative algorithm. Computer simulations show that the proposed algorithms not only yield lower sidelobe level than that of the conventional beamformer, but also show better robustness against steering vector error than the conventional beamformers.

Index Terms ─ Beamforming, robust, sidelobe, sparse, steering vector error.

I. INTRODUCTION

Adaptive beamforming is an important research topic in array signal processing. It is to enhance the source from the desired direction, while suppressing the background noise and all the interference from other directions. A representative beamformer is the minimum variance and distortionless response (MVDR) beamformer [1] which casts deep nulls in the directions of strong interferences and at the meantime guarantees the desired signal distortionless. One of the disadvantages of the MVDR beamformer is its high sidelobe level which results in significant performance degradation in case of unexpected interference or increase of the noise power [2]. In practice, look direction mismatch due to imperfect array occurs. In such case, the signal of interest (SOI) will be mistaken as interference and the performance of the MVDR beamformer is known to degrade dramatically [3].

There has been much effort dedicated to design robust beamforming algorithms against imperfect array [4]. To address the uncertainty of the steering vector and the direction-of-arrival (DOA) of SOI, a set of unity-gain constraints for neighboring directions of the nominal look direction can be imposed [5]. Besides, the derivative of the array output can be imposed to zero at the desired look angle, which is called the derivative mainbeam constraints [6-8]. Some regularization methods [9, 10] are also proposed to enhance the robustness of the MVDR beamformer against steering vector error [11]. Beamformers using eigenvalue thresholding methods to achieve robustness have also been discussed [12].

In this paper, we propose two new beamforming algorithms which are robust against look direction mismatch and steering vector error. Besides, the achieved beampatterns have lower sidelobe level compared with the MVDR beamformer. Sidelobe suppression is realized via imposing a sparse constraint on beampattern with

1054-4887 © 2010 ACES

respect to potential interference directions. Due to imperfect knowledge of the array, the presumed directions of SOI maybe vary from the real ones, thereby causes cancelation of SOI. To solve this problem, mainlobe control is considered. Instead of maintaining distortionless response on one look direction, the proposed algorithm attempts to maintain distortionless response on a wide angular range so that sources impinging on the array from nearby directions of look direction can be retained. The two algorithms may be solved iteratively. The validity and advantages of the new algorithms are verified via computer simulations.

II. ALGORITHM I: SIDELOBE SUPPRESSION WITH SPARSE CONSTRAINT ON BEAMPATTERN

The mathematical formulation of the MVDR beamformer is given by

$$\min_{\mathbf{w}} \mathbf{w}^H\mathbf{R}\mathbf{w}, \quad (1a)$$

$$\text{subject to } \mathbf{w}^H\mathbf{a}(\theta_0) = 1, \quad (1b)$$

where $\mathbf{R}$ is the covariance matrix of data, and $\mathbf{w}$ denotes the beamforming vector. From the perspective of beampattern, it is observed from (1b) that there is only an explicit constraint on the look direction, i.e. θ_0, while no constraint is imposed on the directions of interference. To repair this drawback, we propose the following optimization problem with an additional constraint on the sparsity of the beampattern with respect to potential interference directions:

$$\min_{\mathbf{w}} \mathbf{w}^H\mathbf{R}\mathbf{w}/2\,, \quad (2a)$$

$$\text{subject to } \mathbf{w}^H\mathbf{a}(\theta_0) = 1\,, \quad (2b)$$

$$\|\mathbf{w}^H\mathbf{A}\|_p^p < \varepsilon, \quad (2c)$$

where $\mathbf{A}$ is an $L \times N$ matrix which consists of steering vectors in the angular range which contains all the possible interference directions, L is the number of sensors, and N denotes the number of spatial samplings over the angular range with respect to the interference. It is noticed that we have imposed (2c) to the original formulation of the MVDR beamformer (1).

In (2c), $\|\mathbf{x}\|_p = (\sum_i |x_i|^p)^{1/p}$ is the l_p-norm of the vector $\mathbf{x}$. When p < 2, the l_p-norm can be defined as "dispersion" of the super-Gaussian distributions. When p≤1, the l_p-norm can be interpreted as the diversity measurement [13]. The smaller the value of $\|\mathbf{x}\|_p^p$, the sparser the $\mathbf{x}$ is, which means the number of trivial entries in $\mathbf{x}$ is larger. For beamforming, the smaller the value of $\|\mathbf{w}^H\mathbf{A}\|_p^p$, the lower the sidelobe level, since most of the entries in $\mathbf{w}^H\mathbf{A}$ are forced to some trivial values. For our sparse constraint, we require the value of p to be smaller than 2.

To derive the solution of (2), the Lagrange multiplier technique is used:

$$\mathrm{J}(\mathbf{w}) = \frac{\mathbf{w}^H\mathbf{R}\mathbf{w}}{2} + \lambda\|\mathbf{w}^H\mathbf{A}\|_p^p + \gamma(\mathbf{w}^H\mathbf{a}(\theta_0) - 1), \quad (3)$$

where λ and γ are Lagrange multipliers.

Define $\bar{\mathbf{A}} = [\mathbf{A}|\alpha\mathbf{a}(\theta_0)]$, $\mathbf{d}^T = [\mathbf{0}^T|\alpha\mathbf{1}]$, where $\alpha = \gamma/\lambda$. (3) is equivalent to

$$\mathrm{J}(\mathbf{w}) = \frac{\mathbf{w}^H\mathbf{R}\mathbf{w}}{2} + \lambda\|\,\bar{\mathbf{A}}^H\mathbf{w} - \mathbf{d}^*\|_p^p, \quad (4)$$

where * denotes complex conjugate.

Calculating the gradient of $\mathrm{J}(\mathbf{w})$ with respect to $\mathbf{w}$, we have

$$\nabla_{\mathbf{w}}\mathrm{J}(\mathbf{w}) = \mathbf{R}\mathbf{w} + \tilde{\lambda}\,\bar{\mathbf{A}}\boldsymbol{\Pi}(\boldsymbol{w})(\,\bar{\mathbf{A}}^H\mathbf{w} - \mathbf{d}^*), \quad (5)$$

where $\tilde{\lambda} = \lambda\mathrm{p}$, and $\boldsymbol{\Pi}(\boldsymbol{w})$ is given by $\boldsymbol{\Pi}(\boldsymbol{w}) = \mathrm{diag}\{|(\,\bar{\mathbf{A}}^H\mathbf{w} - \mathbf{d}^*)_1|^{p-2}, \ldots, |(\,\bar{\mathbf{A}}^H\mathbf{w} - \mathbf{d}^*)_N|^{p-2}\}$.

Equating (5) to zero, and using the gradient factorization approach [13], the update formula of $\mathbf{w}$ is given by

$$\mathbf{w}(i+1) = \tilde{\lambda}\left(\mathbf{R} + \tilde{\lambda}\,\bar{\mathbf{A}}\boldsymbol{\Pi}(\mathbf{w}(i))\,\bar{\mathbf{A}}^H\right)^{-1}\bar{\mathbf{A}}\boldsymbol{\Pi}(\mathbf{w}(i))\mathbf{d}^*, \quad (6)$$

where i denotes the iteration index.

III. ALGORITHM II: SIDELOBE SUPPRESSION WITH ROBUSTNESS CONSIDERATION

Notice that the above formulation is proposed under the assumption that the real steering vector is known. When the presumed steering vector is used instead of the real steering vector, the above formulation may break down when $\mathbf{A}$ contains the real steering vector of SOI. This happens when the presumed look direction is erroneous.

To amend this drawback, we generalize the above formulation by mainlobe control. The direction of SOI is assumed to be contained within a spatial sector instead of a particular direction. Let $\boldsymbol{\theta}_s$ denote the spatial sector where the directions of SOI is assumed to be contained. The extension of the optimization problem (2) is given as follows:

$$\min_{\mathbf{w}} \mathbf{w}^H\mathbf{R}\mathbf{w}/2\,, \quad (7a)$$

$$\text{subject to } \mathbf{A}_s{}^H\mathbf{w} = 1\,, \quad (7b)$$

$$\|\mathbf{w}^H\mathbf{A}\|_p^p < \varepsilon, \quad (7c)$$

where $\mathbf{A}_s = \left[\mathbf{a}\left(\theta_{s,1}\right), \ldots, \mathbf{a}\left(\theta_{s,N_s}\right)\right]$ consists of possible steering vectors of SOI within the spatial sector $\boldsymbol{\theta}_s$.

The solution to the above optimization can be derived in a similar way as the derivation presented in Section II. Firstly, we combine the constraints (7b) and (7c):

$$\min_{\mathbf{w}} \mathbf{w}^H\mathbf{R}\mathbf{w}/2 \quad (8a)$$

$$\text{subject to } \| \boldsymbol{\Gamma}^H\mathbf{w} - \mathbf{d}^*\|_p^p, \quad (8b)$$

where $\boldsymbol{\Gamma} = [\mathbf{A}|\alpha\mathbf{A}_s]$. Next, we formulate the Lagrange function and equate its gradient to zero. Finally, the weight vector update equation is obtained as follows:

$\mathbf{w}(i+1)=$

$$\tilde{\lambda}\left(\mathbf{R} + \tilde{\lambda}\boldsymbol{\Gamma}\boldsymbol{\Pi}\left(\mathbf{w}(i)\right)\boldsymbol{\Gamma}^H\right)^{-1}\boldsymbol{\Gamma}\boldsymbol{\Pi}\left(\mathbf{w}(i)\right)\mathbf{d}^*, \quad (9)$$

where $\boldsymbol{\Pi}(\boldsymbol{w})$ is given by $\boldsymbol{\Pi}(\boldsymbol{w}) = \text{diag}\{|(\boldsymbol{\Gamma}^H\mathbf{w} - \mathbf{d}^*)_1|^{p-2}, \ldots, |(\boldsymbol{\Gamma}^H\mathbf{w} - \mathbf{d}^*)_N|^{p-2}\}$.

It is worth mentioning that the matrix $\boldsymbol{\Gamma}$ can be implemented by considering only a few directions representing the directions of the SOI within the spatial sector $\boldsymbol{\theta}_s$. In fact, the number of directions within $\boldsymbol{\theta}_s$ can be as small as two, i.e. $N_s = 2$. To do so, the first direction $\theta_{s,1}$ is taken at the left boundary while the other $\theta_{s,2}$ is taken at the right boundary. It is demonstrated by computer simulations that the optimization problem (7), compared to optimization problem (2), has several advantages: 1) better robustness against look direction mismatch; 2) smaller value of N to generate $\mathbf{A}$ with respect to interference directions; 3) better performance when the real interference directions are not precisely located at the sampling directions of $\mathbf{A}$.

IV. IMPLEMENTATION OF THE PROPOSED ALGORITHMS

From (7) and (10), it is observed that there are three parameters: p, λ, and γ, impacting the performance of the proposed beamformers. The parameter p determines the sparsity of the beampattern. The smaller the value of p, the sparser the derived beampattern (or equivalently, the lower the sidelobe level). The parameter λ determines the effectiveness of the sparse constraint. Using a large λ emphasizes the impact of the sparse constraint and will result in a trivial solution $\mathbf{w}$ ($\mathbf{w} = \mathbf{0}$ gives the smallest value of $\|\mathbf{w}^H\mathbf{A}\|_p^p$), since the constraint on distortionless response in (2b) and (7b) will be neglected in this situation. Similarly, using a large γ emphasizes the impact of the distortionless response constraint and will attenuate the effect of the sparse constraint. Therefore, these parameters should be chosen properly in order to have good compromise between suppression of interferences and maintenance of the desired source.

In order to appropriately choose λ, we compute the gradient of (3) with respect to λ, and equating it to zero yields

$$\| \bar{\mathbf{A}}^H\mathbf{w} - \mathbf{d}^*\|_p^p = 0. \quad (10)$$

Left multiplying (5) with $\mathbf{w}^H$ yields

$$\mathbf{w}^H\mathbf{R}\mathbf{w} + \tilde{\lambda}\bar{\mathbf{A}}\boldsymbol{\Pi}(\boldsymbol{w})(\bar{\mathbf{A}}^H\mathbf{w} - \mathbf{d}^*) = 0. \quad (11)$$

With the definition of $\bar{\mathbf{A}}$ and $\mathbf{d}$, we may equivalently express (10) as

$$\| \mathbf{A}^H\mathbf{w}\|_p^p + \alpha^p|\mathbf{w}^H\mathbf{a}(\theta_0) - 1|^p = 0. \quad (12)$$

Also, (11) is equivalent to

$$\mathbf{w}^H\mathbf{R}\mathbf{w} + \| \mathbf{A}^H\mathbf{w}\|_p^p + \alpha^p\mathbf{w}^H\mathbf{a}(\theta_0) |\mathbf{w}^H\mathbf{a}(\theta_0) - 1|^{p-2}(\mathbf{w}^H\mathbf{a}(\theta_0) - 1) = 0, \quad (13)$$

which can be written as

$$\mathbf{w}^H\mathbf{R}\mathbf{w} + \| \mathbf{A}^H\mathbf{w}\|_p^p + \alpha^p|\mathbf{w}^H\mathbf{a}(\theta_0) - 1|^p + \alpha^p|\mathbf{w}^H\mathbf{a}(\theta_0) - 1|^{p-2}(\mathbf{w}^H\mathbf{a}(\theta_0) - 1) = 0. \quad (14)$$

With (12), (14) can be simplified as

$$\mathbf{w}^H\mathbf{R}\mathbf{w} + \alpha^p|\mathbf{w}^H\mathbf{a}(\theta_0) - 1|^{p-2} (\mathbf{w}^H\mathbf{a}(\theta_0) - 1) = 0. \quad (15)$$

Solving (15) gives the solution of λ as

$$\lambda = \gamma\left(\frac{\mathbf{w}^H\mathbf{R}\mathbf{w}}{|\mathbf{w}^H\mathbf{a}(\theta_0) - 1|^{p-2}(\mathbf{w}^H\mathbf{a}(\theta_0) - 1)}\right)^{1-p}. \quad (16)$$

When implementing the algorithm, we may alternatively update $\mathbf{w}(i)$ and $\lambda(i)$ or $\gamma(i)$ using (6) and (16), respectively. For the second algorithm, the relationship between λ and γ is the same as (16) by replacing $\bar{\mathbf{A}}$ with $\boldsymbol{\Gamma}$, and setting the denominator as $\|\mathbf{A}_s^H\mathbf{w} - \mathbf{d}\|^{p-1}$.

Because we have deduced the relationship between λ and γ, we may properly determine one of them and compute the other one using (16). Based on the existing literature, when p is fixed, some principles of choosing a proper λ, such as the L-curve [13], have been introduced. Therefore, when implementing the algorithm, we may firstly choose a proper value of p. Then, we use existing principles to determine λ. When λ is derived, we use (16) to compute γ. It should be emphasized that how to precisely choose λ is still an open issue. Current algorithms do not guarantee the optimal results. Fortunately, from our computer simulations, we see that the proposed algorithms are not sensitive to the choice of λ and γ. Therefore, they can be chosen empirically. When doing so, we should keep in mind that if a large λ

or a small p is used, the value of γ should not be too small so that a trivial **w** can be avoided.

We summarize the proposed algorithms in Table 1.

Table 1: Summary of the proposed algorithms

Step 1: Parameter setting: 1) Set up p, λ and γ (λ and γ can be chosen empirically); 2) Generate $\bar{\mathbf{A}}$ according to the presumed look direction and sidelobe sector;
Step 2: Initialize: i=0, **w**(0);
Step 3: Iterations: 1) Compute $\boldsymbol{\Pi}(\mathbf{w}(\mathrm{i}))$; 2) Update **w**(i) using (6) or (9); 3) If λ is not chosen empirically, using the L-curve principle to determine λ; 4) Compute γ using (16); 5) i=i+1;
Step 4: Terminate the algorithm if the stopping criterion is satisfied, otherwise go to *Step 3*.

The stopping criterion can be chosen as $i>N_{iter}$, where N_{iter} is a preset number. The other usually adopted stopping rule is to evaluate the value of $\|\mathbf{w}(i+1)-\mathbf{w}(i)\|_2^2/\|\mathbf{w}(i)\|_2^2$. If it is smaller than a preset threshold, terminate the algorithm.

V. COMPUTER SIMULATIONS

In this section, computer simulations are conducted to verify validity and advantages of the proposed algorithms. In all the simulations, the beampattern is computed by $20\log_{10}|\mathbf{w}^H\mathbf{a}(\theta)|$ for $\theta\in[-90^o,90^o]$.

A. Implementation of algorithm I to array synthesis

It is observed that the proposed algorithms can also be applied to the array synthesis algorithm [14] with **R**=**I** in (2). The sparse constraint (2c) plays a role to suppress the assigned sidelobe sector. To verify this, we conduct the following simulations. A uniform linear array (ULA) with 32 half-wavelength spaced sensors is assumed.

Firstly, we assume sidelobe suppression sector as$[-90^o,-1^o]\cup[1^o,90^o]$. The array beampattern obtained using the proposed algorithm is shown in Fig. 1.

One can see from Fig. 1 that the proposed algorithm reduces the sidelobe level several decibels from the original beampattern. Also, it is noticed that the smaller the value of p, the greater the sidelobe suppression. This coincides with our previous analysis that p controls the sparsity of the beampattern.

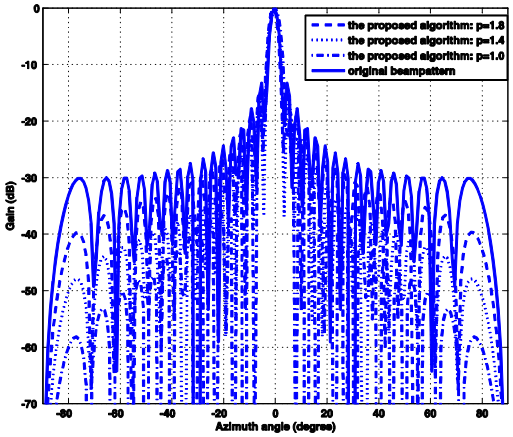

Fig. 1. Array beampatterns for a 32-sensor ULA with sidelobe suppression sector $[-90^o,-1^o]\cup[1^o,90^o]$.

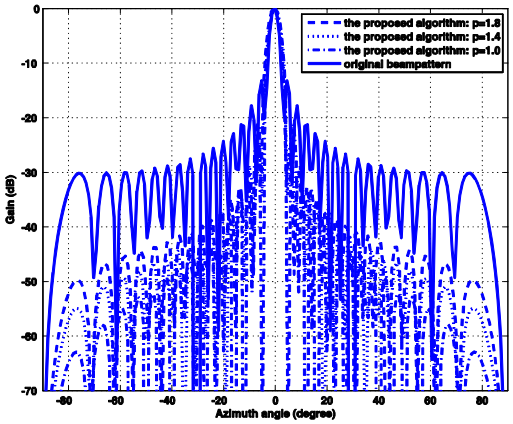

Fig. 2. Array beampatterns for a 32-sensor ULA with sidelobe suppression sector $[-90^o,-5^o]\cup[5^o,90^o]$.

In certain applications, one may like to maintain the mainlobe of the array response at a certain width to ensure that the signal coming from the desired look direction will be received by the array with sufficient array gain. In Fig. 2, the proposed algorithm is used in the design of array pattern under this situation. The sidelobe suppression sector is chosen to be $[-90^o,-5^o]\cup[5^o,90^o]$.

It is seen that compared with the original beampattern, the beamwidth is increased slightly, while the sidelobe level is improved by the order of tens of decibels. The sidelobes beside the mainlobe is significantly improved by more than 5 dB.

B. Evaluation of algorithm I on narrowband beamforming

In this section, a ULA with eight half-wavelength inter-element spaced sensors is used. The DOA of the desired signal is supposed to be 0^o, and the DOAs of three interferences are set to -30^o, 30^o and 70^o. The signal-to-noise ratio (SNR) is set to 10 dB, and the signal-to-interference ratio (SIR) is -20 dB. 100 snapshots are used to compute the covariance matrix **R**. The regularization parameter λ is set to 0.2 in all the simulations. The matrix A consists of array steering vectors in the angular range from $[-90^o, -1^o] \cup [1^o, 90^o]$ with 1^o sampling interval. In this case, all the potential interferences are contained in **A** and the sidelobe level of the whole angular range is under control.

In the first simulation, we assume mismatch does not occur. The proposed method is compared with the MVDR beamformer. With different p and α, the derived beampatterns are shown in Fig. 3.

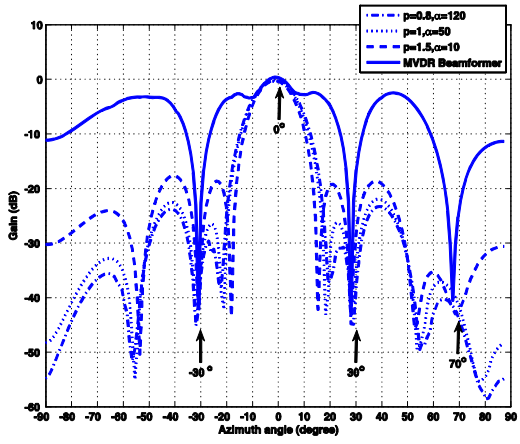

Fig. 3. Array beampatterns for SNR=10 dB in the no mismatch case (Algorithm I).

It is observed that all of the beamformers cast deep nulls in directions of interference and generate distortionless response at the look direction. However, the sidelobe level of the MVDR beamformer is much higher than that of the proposed algorithm. For the proposed beamformer, the sidelobe level decreases as p decreases. This is because the smaller the p, the smaller the values of the beampattern are. This simulation result coincides with our previous analysis.

Figure 4 shows the plots of output SINR versus SNR with 1000 independent trials. The output signal to interference plus noise ratio (SINR) is calculated via

$$SINR_{output} = \frac{\sigma_s^2 \mathbf{w}^H \mathbf{a}(\theta_0)\mathbf{a}^H(\theta_0)\mathbf{w}}{\mathbf{w}^H \left(\sum_{j=1}^{J} \sigma_j^2 \mathbf{a}(\theta_j)\mathbf{a}^H(\theta_j) + \sigma_n^2 \mathbf{I}\right)\mathbf{w}}, \quad (17)$$

where J denotes the number of interferences.

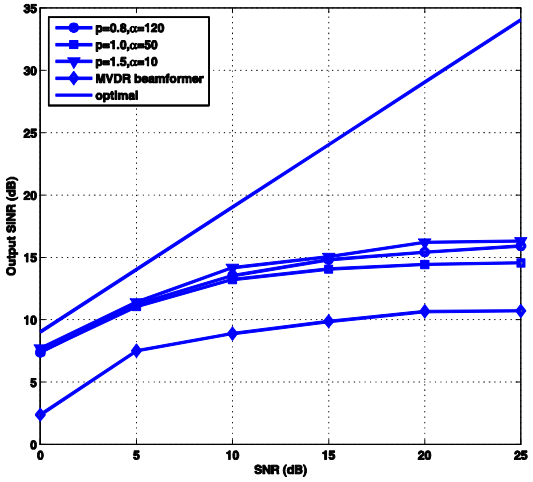

Fig. 4. Plots of output SINR versus SNR in the no mismatch case (Algorithm I).

It is noted that the proposed beamformer can achieve an output SINR approximately 6 dB larger than that of MVDR beamformer for all of the SNRs. For different p and α, the proposed algorithm shows similar performance results.

In the second simulation, we assume there is a 3^o mismatch in the look direction. The desired signal impinges the array from broadside, while the look direction of the beamformer is assumed to be 3^o. Figure 5 shows the obtained beampatterns of different algorithms.

It is observed from Fig. 5 that the MVDR beamformer introduced a deep null at 0^o, which means the desired source is suppressed due to imprecise knowledge of the look direction. In contrast, the proposed beamformer only slightly

shifts its maximum point of the beampattern, and is still capable of generating a distortionless response at the direction of SOI. At interference directions, all the algorithms are able to cast deep nulls.

Figure 6 plots the output SINR versus SNR with 1000 independent trials. From the figure, we see that the performance of MVDR beamformer and the proposed one differ a lot. It is observed that the proposed algorithm gives an output SINR about 10 dB, while the MVDR beamformer fails to work in all the cases. Similar to Figure 4, for different p and α, the proposed algorithm has very similar performance.

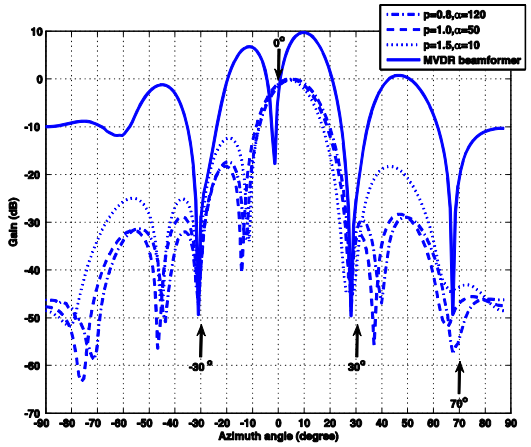

Fig. 5. Array beampatterns for SNR=10 dB with 3° mismatch (Algorithm I).

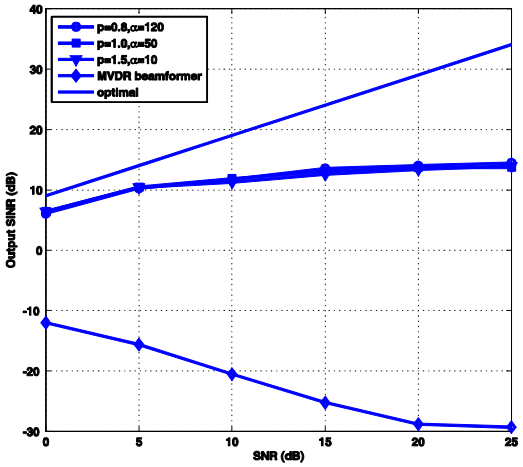

Fig. 6. Plots of output SINR versus SNR with 3° mismatch (Algorithm I).

C. Evaluation of algorithm II on narrowband beamforming

In this section, we evaluate the performance of the proposed Algorithm II when directions of interferences and the SOI are not precisely known. An ULA with ten half-wavelength inter-element spaced sensors is used. The actual source DOA is supposed to be 0°, and the DOAs of four interference signals are set to -30°, -10°, 20° and 45°. The SIR is assumed to be -20 dB, and the SNR is assumed to be 10 dB. The matrix $\mathbf{A}$ consists of array steering vectors in the DOA range $[-90^o,-4^o) \cup (4^o,90^o]$with 10° sampling interval, while the matrix $\mathbf{A}_s$ consists of only two array steering vectors that is defined at -3° and 3°.

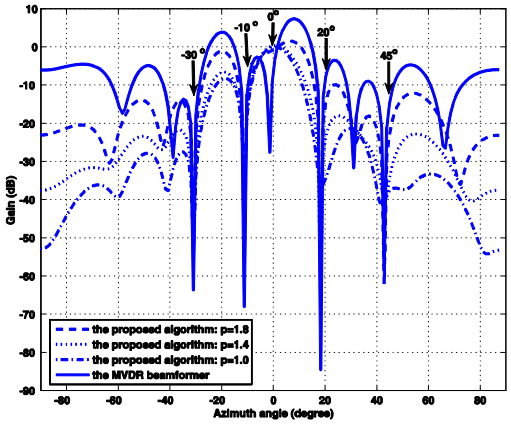

Fig. 7. Array beampatterns for SNR=10 dB with 3° mismatch (Algorithm II).

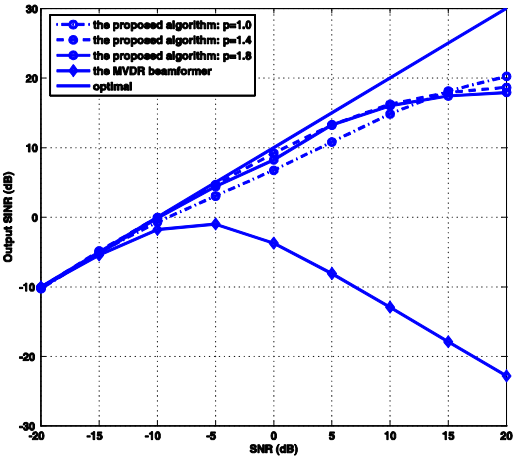

Fig. 8. Plots of output SINR versus SNR with 3° mismatch (Algorithm II).

Note that unlike the simulation settings in the previous section, we greatly relax our interferences constraints by using a 10^o sampling interval. Also, the interference from 45^o is not located on the spatial sampling grid.

In the first simulation, we assume a 3^o look mismatch, i.e., the SOI impinges the array from broadside direction, while we assume it comes from 3^o. Figure 7 shows the derived beampatterns using different algorithms.

It is observed from Fig. 7 that the MVDR castsa deep null at 0^o, while the proposed algorithm still performs satisfactorily in this case. For interference directions, the algorithm casts deep nulls.

Figure 8 plots the output SINR versus SNR for 1000 independent trials. We see that the proposed algorithm outperforms the MVDR beamformer. The MVDR beamformer almost fails to work in all the cases. The proposed algorithms with different values of p again achieve similar performance to each other.

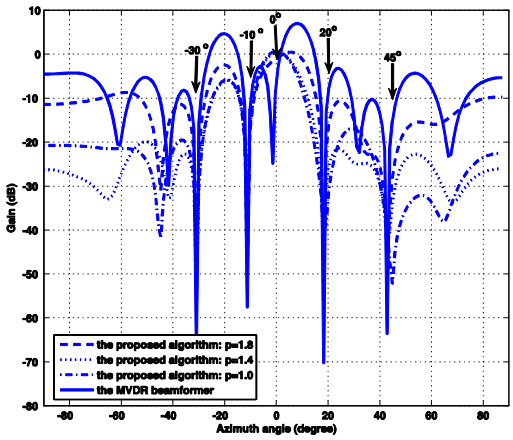

Fig. 9. Array beampatterns for SNR=10 dB with 3^o mismatch and sensor position error (Algorithm II).

In the second simulation, besides the look direction mismatch, we further assume sensor position error which is a Gaussian variable with zero mean and standard deviation 0.1 times the sensor spacing appears in the steering vector. Figure 9 depicts the obtained beampatterns using different algorithms. Figure 10 shows the output SINR versus SNR for 1000 independent trials.

From Fig. 9, we see that the proposed algorithm is capable of maintaining distortionless response at the direction of the SOI, while the MVDR beamformer suppresses the SOI about 25 dB in order to yield a distortionless response at the look direction. Figure 10 clearly demonstrates that the proposed algorithm is robust against look direction error and sensor position error, while the MVDR beamformer is very sensitive to these errors.

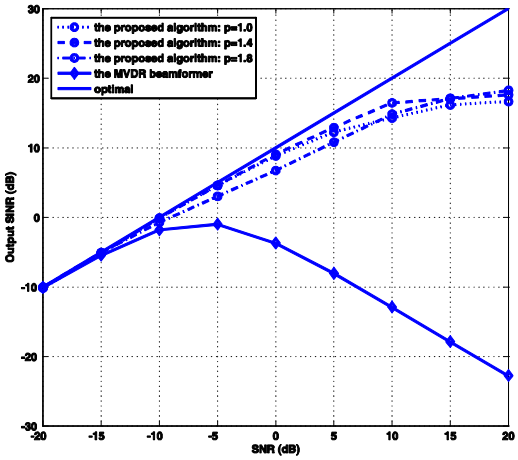

Fig. 10. Plots of output SINR versus SNR with 3^o mismatch and sensor position error (Algorithm II).

VI. CONCLUSIONS

In this paper, we propose two beamforming algorithms which use sparse constraint to suppress a sidelobe level of beampattern. Taking imperfect array into account, we also add robust constraint on the new beamformers. All these algorithms are easy to implement. Computer simulations demonstrate that these algorithms work satisfactorily in the presence of steering vector error. Furthermore, the proposed algorithms are not very sensitive to the values of parameters used in the algorithms.

ACKNOWLEDGMENT

The authors would like to express their gratitude to all the anonymous reviewers for their comments and suggestions to improve the quality of the paper.

REFERENCES

[1] J. Capon, "High resolution frequency wavenumber spectrum analysis," *Proceedings*

of the IEEE, vol. 57, no. 8, pp. 1408-1418, August 1969.

[2] M. Wax and Y. Anu, "Performance analysis of the minimum variance beamformer," *IEEE Transactions on Signal Processing*, vol. 44, no. 4, pp. 928-937, April 1996.

[3] H. Cox, "Resolving power and sensitivity to mismatch of optimum array processors," *Journal of the Acoustic Society of America*, vol. 54, no. 3, pp. 771-785, September 1973.

[4] J. Li and P. Stoica, *Robust Adaptive Beamforming*, New York: Wiley, 2006.

[5] J. L. Krolik, "The performance of matched-field beamformers with mediterranean vertical array data," *IEEE Transactions on Signal Processing*, vol. 44, no. 10, pp. 2605-2611, 1996.

[6] K. Buckley, and L. Griffths, "An adaptive generalized sidelobe canceller with derivative constraints," *IEEE Transactions on Antennas and Propagations*, vol. 34, no. 3, pp. 311-319, March 1986.

[7] A. K. Steele, "Comparison of directional and derivative constraints for beamformers subject to multiple linear constraints," *IEE Proceedings F Communications, Radar and Signal Processing*, vol. 130, no. 1, pp. 41-45, 1983.

[8] M. H. Er, B. P. Ng, and A. Cantoni, "A new set of constraints for derivative-constrained broad-band beamformers," *Journal of Electrical and Electronics Engineering*, vol. 11, no. 2, pp. 87-101, June 1991.

[9] J. Li, P. Stoica, and Z. Wang, "Doubly constrained robust capon beamformer," *IEEE Transactions on Signal Processing*, vol. 52, no. 9, pp. 2407-2423, September 2004.

[10] A. N. Tikhonov, and Y. V. Arsenin, *Solution of Ill-posed Problems*, V. H. Winston and Sons, 1977.

[11] A. B. Gershman, "Robust adaptive beamforming in sensor arrays," *AEU-International Journal of Electronics and Communications*, vol. 53, no. 6, pp. 305-314, June 1999.

[12] K. Harmanci, "Relationships between adaptive minimum variance beamforming and optimal source localization," *IEEE Transactions on Signal Processing*, vol. 48, no. 1, pp. 1-13, 2000.

[13] B. D. Rao, K. Engan, S. F. Cotter, and J. Palmer, and K. K. Delgado, "Subset selection in noise based on diversity measure minimization," *IEEE Transactions on Signal Processing*, vol. 51, no. 3, pp. 760-770, March 2003.

[14] L. J. Griffths and K. M. Buckley, "Quiescent pattern control in lineary constrained adpatively arrays," *IEEE Transactions on Acoustics, Speech and Signal Processing*, vol. 35, no. 7, pp. 917-926, July 1987.

Ying Zhang received the B.Eng. degree and Ph.D. degree in Electronics Engineering (EE) from the University of Electronic Science and Technology of China (UESTC) and Nanyang Technological University (NTU) in 2004 and 2010, respectively. Since 2010, she has been a research fellow at the School of Electrical & Electronic School (EEE), NTU. Her research interests include array signal processing, sparse signal representation, and wireless communication.

Huapeng Zhao received the B.Eng. degree and M.Sc. degree in EE from UESTC in 2004 and 2007, respectively. Since 2008, he has been working towards his Ph.D. degree in NTU. His research interests include computational electromagnetics, statistical electromagnetics, signal processing techniques in electromagnetics, and measurements in electromagnetic reverberation chamber.

Joni Polili Lie received the Ph.D. degree in EE from NTU in 2009. He is currently a research scientist in Temasek Labs@NTU. His research interests include array signal processing and wireless communications.

Boon Poh Ng received the B.Eng. degree in Electrical Engineering from Nanyang Technological Institute, Singapore, in 1987, the D.I.C. and M.Sc. degrees in Communications and Signal Processing from Imperial College, University of London, London, U.K., in 1991, and the Ph.D. degree from NTU, Singapore, in 1995.

He is currently an Associate Professor at the School of EEE, NTU. His research interests include array synthesis, adaptive array processing, spectral estimation, and digital signal processing in general.

Qun Wan received the B.Sc. degree in Applied Physics from Nanjing University, China, in 1993. He received the M.Sc. and Ph.D. degrees in EE from UESTC, China, in 1996 and 2000, respectively. From 2001 to 2003, he was a post-doctor with Department of EE, Tinghua Univeristy, China.

He is currently a professor at the College of EE, UESTC. His research interests include mobile localization, spectral estimation, sparse signal processing, and array signal processing.

A Frequency-Dependent Hybrid Implicit-Explicit FDTD Scheme for Dispersive Materials

Juan Chen and Anxue Zhang

School of Electronic and Information Engineering
Xi'an Jiaotong University, Xi'an 710049, China
anxuezhang@mail.xjtu.edu.cn

Abstract- A frequency-dependent hybrid implicit-explicit finite-difference time-domain (HIE-FDTD) method for dispersive materials is presented. This method has higher computation efficiency than the conventional FDTD method, because the time step in this method is only determined by two space discretizations. The accuracy of this method is demonstrated by computing the incident at a planar air-water interface over a wide frequency band including the effects of the frequency-dependent permittivity of water.

Index Terms- Dispersive materials, HIE-FDTD method, weakly conditional stability.

I. INTRODUCTION

The finite-difference time-domain (FDTD) method [1] has been proven to be an effective scheme that provides accurate predictions of field behaviors for varieties of electromagnetic interaction problems. However, as it is based on an explicit finite-difference algorithm, the Courant–Friedrich–Levy (CFL) condition [2] must be satisfied when this method is used. Therefore, a maximum time-step size is limited by the minimum cell size in a computational domain, which makes this method inefficient for the problems where fine scale structures are involved.

To overcome the CFL constraint on the time step size of the FDTD method, some unconditionally stable methods [3-7] and weakly conditionally stable [8-17] schemes have been studied, among which, the hybrid implicit-explicit finite-difference time-domain (HIE-FDTD) method, has been applied extensively [13-17]. In the HIE-FDTD method, the time step size is only determined by two space discretizations, which is useful for problems with very fine structures in one direction. The accuracy and computational efficiency of the HIE-FDTD method have been well validated in [13-15] and [17].

In this paper, the HIE-FDTD method will be extended to frequency-dependent materials. The formulations of HIE-FDTD for a frequency-dependent complex permittivity are presented and an example of calculation of a wave incident at a planar air-water interface over a wide frequency band is showed. The extension of the HIE-FDTD method to frequency-dependent permeability is similar.

II. FORMULATION

For this paper, we will assume that our materials are linear and isotropic, and only the permittivity is frequency-dependent. Extension to nonlinear or anisotropic dispersive materials should be possible.

The displacement vector D is related to the electric field E in the time domain by the following equation:

$$D(t) = \varepsilon_\infty \varepsilon_0 E(t) + \varepsilon_0 \int_0^t E(t-\tau)\chi(\tau)\, d\tau. \tag{1}$$

ε_0 is permittivity of free space, $\chi(\tau)$ is the electric susceptibility, and ε_∞ is the infinite frequency relative permittivity.

Using Yee's notation, we let $t = n\Delta t$ in (1), and each vector component of D and E can be written as:

$$D(t) \approx D(n\Delta t) = D^n = \varepsilon_\infty \varepsilon_0 E^n + \varepsilon_0 \int_0^{n\Delta t} E(n\Delta t - \tau)\chi(\tau) d\tau. \tag{2}$$

1054-4887 © 2010 ACES

All field components are assumed to be constant over each time interval Δt. Therefore, we have, assuming $D(t)$ and $E(t)$ are zero for $t<0$:

$$D^n = \varepsilon_\infty \varepsilon_0 E^n + \varepsilon_0 \sum_{m=0}^{n-1} E^{n-m} \int_{m\Delta t}^{(m+1)\Delta t} \chi(\tau) d\tau. \tag{3}$$

$$D^{n+1} = \varepsilon_\infty \varepsilon_0 E^{n+1} + \varepsilon_0 \sum_{m=0}^{n} E^{n+1-m} \int_{m\Delta t}^{(m+1)\Delta t} \chi(\tau) d\tau. \tag{4}$$

When (3) is substituted in (4), we find:

$$\begin{aligned} D^{n+1} - D^n &= \varepsilon_\infty \varepsilon_0 \left[E^{n+1} - E^n \right] \\ &+ \varepsilon_0 E^{n+1} \int_0^{\Delta t} \chi(\tau) d\tau \\ &+ \varepsilon_0 \sum_{m=0}^{n-1} E^{n-m} \left\{ \begin{array}{l} \int_{(m+1)\Delta t}^{(m+2)\Delta t} \chi(\tau) d\tau \\ -\int_{m\Delta t}^{(m+1)\Delta t} \chi(\tau) d\tau \end{array} \right\}. \end{aligned} \tag{5}$$

For simplicity, we let:

$$\chi_m = \int_{m\Delta t}^{(m+1)\Delta t} \chi(\tau) d\tau. \tag{6}$$

$$\Delta\chi_m = \chi_m - \chi_{m+1}. \tag{7}$$

Then, we have:

$$\begin{aligned} E^{n+1} &= \frac{\varepsilon_\infty}{(\varepsilon_\infty + \chi_0)} E^n \\ &+ \frac{1}{(\varepsilon_\infty + \chi_0)} \sum_{m=0}^{n-1} E^{n-m} \Delta\chi_m \\ &+ \frac{D^{n+1} - D^n}{(\varepsilon_\infty \varepsilon_0 + \varepsilon_0 \chi_0)}. \end{aligned} \tag{8}$$

The three HIE-FDTD scalar equations that relate the components of the electric field E to the components of the magnetic field H can be readily obtained from (8) by using the discretized Maxwell-Ampere equation to replace $D^{n+1} - D^n$ in (8) with the curl of the H field,

$$\begin{aligned} E_y^{n+\frac{1}{2}}\left(i, j+\frac{1}{2}, k\right) &= \frac{\varepsilon_\infty}{(\varepsilon_\infty + \chi_0)} E_y^{n-\frac{1}{2}}\left(i, j+\frac{1}{2}, k\right) \\ &+ \frac{1}{(\varepsilon_\infty + \chi_0)} \sum_{m=0}^{n-\frac{3}{2}} E_y^{n-\frac{1}{2}-m}\left(i, j+\frac{1}{2}, k\right) \Delta\chi_m \\ &+ \frac{\Delta t}{(\varepsilon_\infty \varepsilon_0 + \varepsilon_0 \chi_0)\Delta z} \left[\begin{array}{l} H_x^n\left(i, j+\frac{1}{2}, k+\frac{1}{2}\right) \\ -H_x^n\left(i, j+\frac{1}{2}, k-\frac{1}{2}\right) \end{array} \right] \\ &- \frac{\Delta t}{(\varepsilon_\infty \varepsilon_0 + \varepsilon_0 \chi_0)\Delta x} \left[\begin{array}{l} H_z^n\left(i+\frac{1}{2}, j+\frac{1}{2}, k\right) \\ -H_z^n\left(i-\frac{1}{2}, j+\frac{1}{2}, k\right) \end{array} \right]. \end{aligned} \tag{9}$$

$$\begin{aligned} E_x^{n+1}\left(i+\frac{1}{2}, j, k\right) &= \frac{\varepsilon_\infty}{(\varepsilon_\infty + \chi_0)} E_x^n\left(i+\frac{1}{2}, j, k\right) \\ &+ \frac{1}{(\varepsilon_\infty + \chi_0)} \sum_{m=0}^{n-1} E_x^{n-m}\left(i+\frac{1}{2}, j, k\right) \Delta\chi_m \\ &- \frac{\Delta t}{(\varepsilon_\infty \varepsilon_0 + \varepsilon_0 \chi_0)} \frac{1}{\Delta z} \left[\begin{array}{l} H_y^{n+\frac{1}{2}}\left(i+\frac{1}{2}, j, k+\frac{1}{2}\right) \\ -H_y^{n+\frac{1}{2}}\left(i+\frac{1}{2}, j, k-\frac{1}{2}\right) \end{array} \right] \\ &+ \frac{\Delta t}{(\varepsilon_\infty \varepsilon_0 + \varepsilon_0 \chi_0)} \frac{1}{2\Delta y} \left[\begin{array}{l} H_z^{n+1}\left(i+\frac{1}{2}, j+\frac{1}{2}, k\right) \\ -H_z^{n+1}\left(i+\frac{1}{2}, j-\frac{1}{2}, k\right) \end{array} \right] \\ &+ \frac{\Delta t}{(\varepsilon_\infty \varepsilon_0 + \varepsilon_0 \chi_0)} \frac{1}{2\Delta y} \left[\begin{array}{l} H_z^{n}\left(i+\frac{1}{2}, j+\frac{1}{2}, k\right) \\ -H_z^{n}\left(i+\frac{1}{2}, j-\frac{1}{2}, k\right) \end{array} \right]. \end{aligned} \tag{10}$$

$$E_z^{n+1}\left(i,j,k+\frac{1}{2}\right)=\frac{\varepsilon_\infty}{\left(\varepsilon_\infty+\chi_0\right)}E_z^n\left(i,j,k+\frac{1}{2}\right)$$
$$+\frac{1}{\left(\varepsilon_\infty+\chi_0\right)}\sum_{m=0}^{n-1}E_z^{n-m}\left(i,j,k+\frac{1}{2}\right)\Delta\chi_m$$
$$+\frac{\Delta t}{\left(\varepsilon_\infty\varepsilon_0+\varepsilon_0\chi_0\right)\Delta x}\left[\begin{array}{l}H_y^{n+\frac{1}{2}}\left(i+\frac{1}{2},j,k+\frac{1}{2}\right)\\-H_y^{n+\frac{1}{2}}\left(i-\frac{1}{2},j,k+\frac{1}{2}\right)\end{array}\right]$$
$$-\frac{\Delta t}{2\left(\varepsilon_\infty\varepsilon_0+\varepsilon_0\chi_0\right)\Delta y}\left[\begin{array}{l}H_x^{n+1}\left(i,j+\frac{1}{2},k+\frac{1}{2}\right)\\-H_x^{n+1}\left(i,j-\frac{1}{2},k+\frac{1}{2}\right)\end{array}\right]$$
$$-\frac{\Delta t}{2\left(\varepsilon_\infty\varepsilon_0+\varepsilon_0\chi_0\right)\Delta y}\left[\begin{array}{l}H_x^{n}\left(i,j+\frac{1}{2},k+\frac{1}{2}\right)\\-H_x^{n}\left(i,j-\frac{1}{2},k+\frac{1}{2}\right)\end{array}\right].$$

(11)

It can be seen from these equations that the eqs. (10) and (11) can't be used for direct numerical calculation, because they all include the unknown components defined at the same time, thus, modified equations are derived from the original equations.

Updating of E_x^{n+1} component, as shown in eq. (10), needs the unknown H_z^{n+1} component at the same time. In the nonmagnetic media, the updating for H component is unchanged. The equation of the H_z^{n+1} component in the HIE-FDTD method is as follows:

$$H_z^{n+1}\left(i+\frac{1}{2},j+\frac{1}{2},k\right)=H_z^{n}\left(i+\frac{1}{2},j+\frac{1}{2},k\right)$$
$$+\frac{\Delta t}{2\mu\Delta y}\left[\begin{array}{l}E_x^{n+1}\left(i+\frac{1}{2},j+1,k\right)-E_x^{n+1}\left(i+\frac{1}{2},j,k\right)\\+E_x^{n}\left(i+\frac{1}{2},j+1,k\right)-E_x^{n}\left(i+\frac{1}{2},j,k\right)\end{array}\right]$$
$$-\frac{\Delta t}{\mu\Delta x}\left[E_y^{n+\frac{1}{2}}\left(i+1,j+\frac{1}{2},k\right)-E_y^{n+\frac{1}{2}}\left(i,j+\frac{1}{2},k\right)\right].$$

(12)

Thus, the E_x^{n+1} component has to be updated implicitly. Substituting eq. (12) into eq. (10), the equation for E_x^{n+1} field is given as,

$$\left[1+\frac{\Delta t^2}{2\varepsilon\mu\Delta y^2}\eta\right]E_x^{n+1}\left(i+\frac{1}{2},j,k\right)$$
$$-\frac{\Delta t^2}{4\varepsilon\mu\Delta y^2}\eta\left[E_x^{n+1}\left(i+\frac{1}{2},j+1,k\right)+E_x^{n+1}\left(i+\frac{1}{2},j-1,k\right)\right]$$
$$=\eta\varepsilon_\infty E_x^n\left(i+\frac{1}{2},j,k\right)+\eta\sum_{m=0}^{n-1}E_x^{n-m}\left(i+\frac{1}{2},j,k\right)\Delta\chi_m$$
$$+\eta\frac{\Delta t}{\varepsilon\Delta y}\left[H_z^n\left(i+\frac{1}{2},j+\frac{1}{2},k\right)-H_z^n\left(i+\frac{1}{2},j-\frac{1}{2},k\right)\right]$$
$$-\eta\frac{\Delta t^2}{2\mu\varepsilon\Delta x\Delta y}\left[E_y^{n+\frac{1}{2}}\left(i+1,j+\frac{1}{2},k\right)-E_y^{n+\frac{1}{2}}\left(i,j+\frac{1}{2},k\right)\right]$$
$$+\eta\frac{\Delta t^2}{2\mu\varepsilon\Delta x\Delta y}\left[E_y^{n+\frac{1}{2}}\left(i+1,j-\frac{1}{2},k\right)-E_y^{n+\frac{1}{2}}\left(i,j-\frac{1}{2},k\right)\right]$$
$$+\eta\frac{\Delta t^2}{4\varepsilon\mu\Delta y^2}\left[E_x^n\left(i+\frac{1}{2},j+1,k\right)-E_x^n\left(i+\frac{1}{2},j,k\right)\right]$$
$$+\eta\frac{\Delta t^2}{4\varepsilon\mu\Delta y^2}\left[E_x^n\left(i+\frac{1}{2},j-1,k\right)-E_x^n\left(i+\frac{1}{2},j,k\right)\right]$$
$$-\eta\frac{\Delta t}{\varepsilon\Delta z}\left[H_y^{n+\frac{1}{2}}\left(i+\frac{1}{2},j,k+\frac{1}{2}\right)-H_y^{n+\frac{1}{2}}\left(i+\frac{1}{2},j,k-\frac{1}{2}\right)\right].$$

(13)

here, $\eta=1/\left(\varepsilon_\infty+\chi_0\right)$.

The updating equation of E_z^{n+1} is similarly derived and calculated in the same way as eq.(13).

Note that if we assume the relative permittivity is independent of frequency, namely, $\chi(\tau)=0$, $\varepsilon_\infty=\varepsilon_r$, $\chi_m=0$ for all m, then, the above equations reduce to the standard HIE-FDTD formulations [13].

The above formulation is valid for electrically dispersive media. The extension to magnetically dispersive media would be similar.

In [15], the weakly conditional stability of the HIE-FDTD method is well validated. The time

step of the HIE-FDTD method is only determined by two spatial increments Δx and Δz, namely:

$$\Delta t \le 1\Big/\left(c\sqrt{\left(1/\Delta x\right)^2+\left(1/\Delta z\right)^2}\right). \qquad (14)$$

$c=1/\sqrt{\varepsilon\mu}$ is the speed of light in the medium. This is especially useful when the simulated structure has fine-scale dimensions in one direction, which will be validated in next section.

III. SIMULATION RESULTS

In order to demonstrate the validity and accuracy of the above formulation, a small current source above an incident at a planar air-water interface is presented here. The geometric configuration of the numerical simulation is shown in Fig.1. The dimensions of the perfect-electric-conductor box are 15cm $\times$15cm $\times$3cm. The box is filled with water up to height 7.5cm. A small current source applied along *y* direction is placed at the upper part of the box. The time dependence of the excitation function is:

$$g(t)=\exp[-4\pi(t-t_0)^2/t_1^2], \qquad (15)$$

where t_0 and t_1 are constants, and both equal to 0.6×10^{-9}. The observation point B is set in the water, and 2 cm far from the source point A.

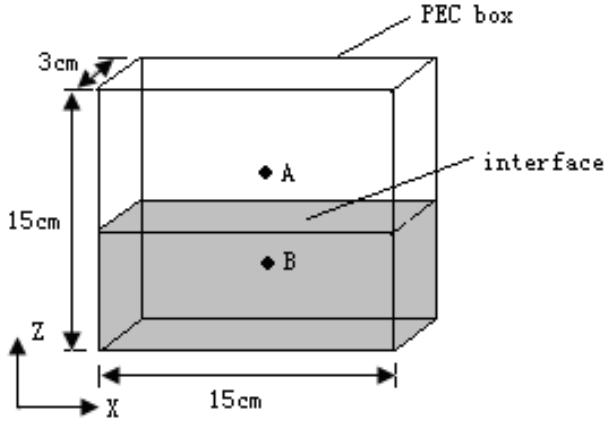

Fig. 1. Geometric configuration of the numerical simulation.

Applying the FDTD method to compute the time domain electric field component E_y at the observation point B, the cell size is chosen as $5\Delta y=\Delta x=\Delta z=$ 0.5cm, so that the computational domain is 30 $\times$30 $\times$30 cells. To satisfy the stability condition of the FDTD algorithm, the time-step size for conventional FDTD [18, 19] is $\Delta t \le$ 3.20ps. Here, the conventional FDTD is the FDTD method using recursive convolutional (RC) method to implement the dispersive media. For the HIE-FDTD scheme, the maximum time increment is only related to the space increments Δx and Δz, that is, $\Delta t \le$ 11.78ps. The HIE-FDTD method is using the recursive convolutional method with Debye model to implement the dispersive properties of the media.

For water, the complex permittivity $\varepsilon^*(\omega)$ can be described as

$$\varepsilon^*(\omega)=\varepsilon_0\left[\varepsilon_\infty+\left(\varepsilon_s-\varepsilon_\infty\right)/\left(1+j\omega\tau_0\right)\right], \qquad (16)$$

where ε_s is the "static" permittivity, and τ_0 is the "relaxation time" constant. The water parameters used here are ε_s =81, ε_∞ =1.8, and $\tau_0=9.4\times10^{-12}$.

The summation (convolution) term of eq.(8) can be updated recursively by utilizing the equation (20) in [18], because the susceptibility function is an exponential. So, it doesn't require storing a large number of past time values E^n, and the computational time is saved. Only one additional number needs to be stored for each electric field component at each spatial index.

First, we validate the numerical stability condition (14). Figure 2 shows the electric field component E_y at observation point B calculated by using the HIE-FDTD methods with the time-step size Δt =11.78ps for a long time history. No instability problem is observed even for 5,000 steps, which validates the weakly conditional stability of the HIE-FDTD method numerically.

To demonstrate the high computational efficiency of HIE-FDTD method, we perform the numerical simulations for an 8 ns time history by using the conventional FDTD, and HIE-FDTD methods, and compare the CPU times taken by using these two methods. In the conventional FDTD method, the time-step size keeps a constant of 3.20 ps; while in the HIE-FDTD method, the time step size is 11.78ps.

Figure 3 shows the electric field component E_y at observation point B calculated by using the conventional FDTD and HIE-FDTD methods. It can be seen from this figure that the result calculated by the HIE-FDTD method agrees with

the result calculated by the conventional FDTD method. The HIE-FDTD method has almost the same accuracy as that of the conventional FDTD method. To validate this further, the divergence between these two methods are presented, as

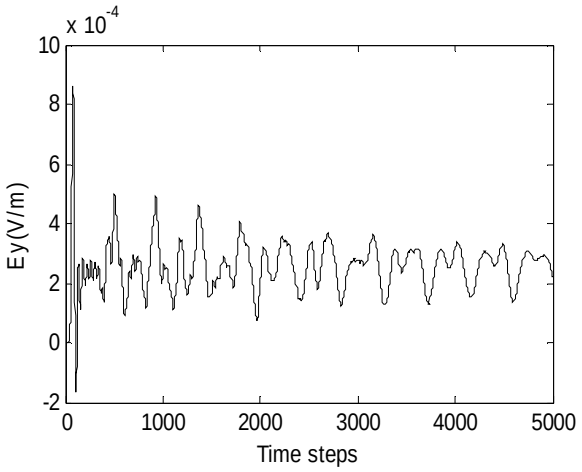

Fig. 2. The electric field component E_y at observation point B calculated by using the HIE-FDTD method with the time-step size Δt =11.78ps for a long time story.

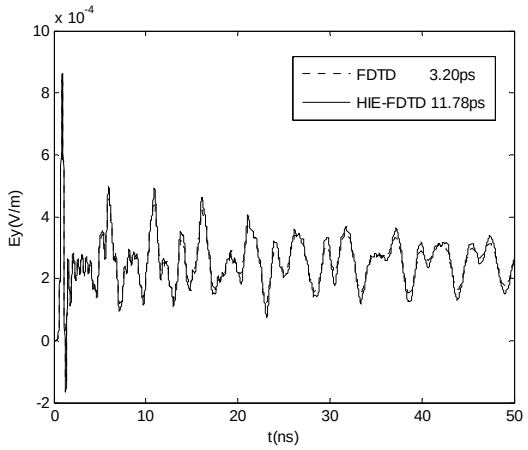

Fig. 3. The electric field component E_y at observation point B calculated by using the conventional FDTD (Δt =3.20ps), and HIE-FDTD methods (Δt =11.78ps).

shown in Fig.4. It can be seen from this figure that the error curve is limited and it doesn't increase as the addition of the computational time. It should be noted that the simulation takes 364 s for the conventional FDTD method and 121 s for the HIE-FDTD method. The time cost for the HIE-FDTD simulation is 1/3 times as that for the conventional FDTD simulation. So, we can conclude that the HIE-FDTD has higher efficiency than the conventional FDTD method, due to larger time step size used.

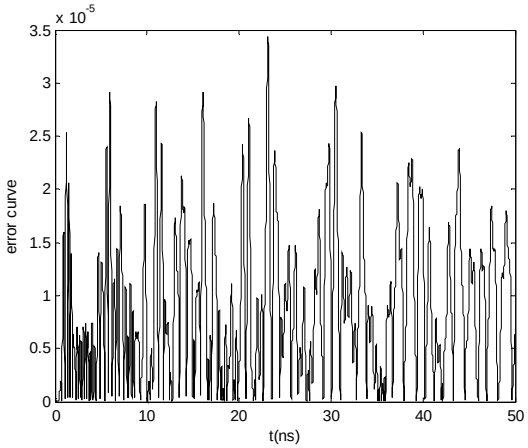

Fig. 4. The divergence between conventional FDTD (Δt =3.20ps), and HIE-FDTD methods (Δt =11.78ps).

IV. CONCLUSION

A frequency-dependent HIE-FDTD method for dispersive materials is presented. It is found that the technique is weakly conditionally stable and supports time steps greater than the CFL limit. A numerical example demonstrates that computation efficiency of the HIE-FDTD method is higher than the conventional FDTD method, and the accuracy of the HIE-FDTD is almost the same as that of the conventional FDTD method.

ACKNOWLEDGMENT

This work was supported by National Natural Science Foundations of China (No. 61001039 and 60501004), and also supported by the Research Fund for the Doctoral Program of Higher Education of China (20090201120030).

REFERENCES

[1] K. S. Yee, "Numerical Solution of Initial Boundary Value Problems Involving Maxwell's Equations in Isotropic Media," IEEE Trans. Antennas Propagat., vol. 14, pp. 302-307, May 1966.

[2] A. Taflove, *Computational Electrodynamics*,

Norwood, MA: Artech House, 1995.

[3] T. Namiki, "3-D ADI-FDTD method-unconditionally stable time-domain algorithm for solving full vector Maxwell's equations," IEEE Trans. Microw. Theory Tech., vol. 48, pp. 1743–1748, Oct. 2000.

[4] F. Zheng, Z. Chen, and J. Zhang, "A finite-difference time-domain method without the Courant stability conditions," IEEE Microw. Guided Wave Lett., vol. 9, pp. 441–443, Nov. 1999.

[5] G. Sun and C. W. Trueman, "Some fundamental characteristics of the one-dimensional alternate-direction-implicit finite-difference time-domain method," IEEE Trans. Microw. Theory Tech., vol. 52, pp. 46-52, Jan. 2004.

[6] S. G. García, T.-W. Lee, and S. C. Hagness, "On the accuracy of the ADI-FDTD method," IEEE Antennas Wireless Propag. Lett., vol. 1, pp. 31–34, 2002.

[7] I. Ahmed and Z. Chen, "Error reduced ADI-FDTD methods," IEEE Antennas Wireless Propagat. Lett., vol. 4, pp. 323-325, 2005.

[8] B. Huang, G. Wang, Y. S. Jiang, and W. B. Wang, "A hybrid implicit-explicit FDTD scheme with weakly conditional stability," Microwave Opt. Technol. Lett., vol. 39, pp. 97-101, Mar. 2003.

[9] J. Chen and J. G. Wang, "Weakly conditionally stability FDTD scheme with reduced split error," Electron. Lett., vol. 42, pp. 1017-1019, Aug. 2006.

[10] J. Chen and J. G. Wang, "3-D FDTD Method with Weakly Conditional Stability," Electron. Lett., vol. 43, pp. 2-3, Jan. 2007.

[11] J. Chen and J. Wang, "A novel WCS-FDTD method with weakly conditional stability," IEEE Trans. Electromagn. Compat., vol. 49, pp. 419-426, May 2007.

[12] J. Chen and J. Wang, "Using WCS-FDTD method to simulate various small aperture-coupled metallic enclosures," Microwave Opt. Technol. Lett., vol.49, pp. 1852-1858, Aug. 2007.

[13] J. Chen and J. Wang, "A 3-D hybrid implicit-explicit FDTD scheme with weakly conditional stability," Microw. Opt. Tech. Lett., vol. 48, pp. 2291-2294, Apr. 2006.

[14] J. Chen and J. Wang, "Comparison between HIE-FDTD method and ADI-FDTD method," Microw. Opt. Tech. Lett., vol. 49, pp. 1001-1005, 2007.

[15] J. Chen and J. Wang, "A three-dimensional semi-implicit FDTD scheme for calculation of shielding effectiveness of enclosure with thin slots," IEEE Trans. Electromagn. Compat., vol. 49, pp. 419-426, May. 2007.

[16] I. Ahmed and E. Li, "Conventional perfectly matched layer for weakly conditionally stable hybrid implicit and explicit-FDTD method," Microwave Opt. Technol. Lett., vol. 49, pp. 3106-3109, Dec. 2007.

[17] J. Chen and J. Wang, "Numerical simulation using HIE–FDTD method to estimate various antennas with fine scale structures," IEEE Trans. Antennas Propagat., vol. 55, pp. 3603-3612, Dec. 2007.

[18] R. Luebbers, F. P. Hunsberger, K. S. Kunz, R. B. Standler, and M. Schneider, "A frequency-dependent finite-difference time-domain formulation for dispersive materials," IEEE Trans. Electromagn. Compat., vol. 32, pp. 222-227, Aug.1990.

[19] J. H. Beggs, "Validation and demonstration of frequency approximation methods for modeling dispersive media in FDTD," Appl. Comput. Electronm., vol. 14, pp. 52-58, Feb.1999.

Adaptive Mixed-Form Fast Multipole Method for the Analysis of Electromagnetic Scattering

H. Chen, Z. H. Fan, R. S. Chen, Z. N. Jiang, and M. M. Li

Department of Communication Engineering
Nanjing University of Science and Technology, Nanjing, China, 210094
eechenrs@mail.njust.edu.cn

Abstract- To analyze an electrically large object with local fine structures, the conventional mixed form fast multipole algorithm requires that the boxes of the finest level are all with the same size, which belongs to the low-frequency region. This scheme is deficient since the mesh size is limited by the box size of the finest level, which is related to the finest parts of the object. In this paper, an efficient adaptive grouping scheme is introduced into a mixed-form fast multipole algorithm. In an adaptive mixed-form fast multipole algorithm, the number of unknowns in each non-empty box of the finest level is almost the same which results in the box of the finest level may be in a different frequency regime with a different size. Hence multipole expansions are employed, if the boxes located in the low frequency regime while the plane wave expansions are employed if the boxes located in the mid-frequency regime. Numerical results are given to show that the proposed approach is efficient to analyze the objects with many fine structures.

Index Terms- Adaptive grouping scheme, electromagnetic scattering, mixed-form fast multipole algorithm, multilevel fast multipole algorithm (MLFMA).

I. INTRODUCTION

The integral equation formulation is one of the most commonly used methods for solving the Maxwell's equations in electromagnetic scattering problems. Due to the fast increasing capability of computers, computational electromagnetics has developed to be more and more powerful. As a result, a number of algorithms have been presented for the fast computation of the large linear matrix equation systems resulting from the discretization of integral equations for electromagnetic scattering, such as conjugate gradient fast Fourier transform (CG-FFT) [1], adaptive integral method (AIM) [2], multilevel fast multipole algorithm (MLFMA) [3], etc.

Although many methods can simulate EM field accurately of electrically large objects, it remains to be difficult to simulate the EM field accurately where the size of the subscatterers is a small fraction of a wavelength. Many traditional methods suffer from a so-called "low frequency breakdown", such as method of moments (MoM), finite element method (FEM) and so on [3]. In order to capture the fine details of the structure accurately, e.g., in circuit components such as inductors and capacitors, this problem becomes more and more important and poses a pressing to simulate EM phenomena in circuits and antennas. Therefore, it becomes a popular topic for researchers in this field to overcome the low-frequency breakdown problem. Some fast methods have been proposed to cover the regime from low frequency to mid frequency, such as loop and tree basis decomposition introduced for EFIE [15, 16], the plane wave methods based on the generalized Gaussian quadrature rules proposed by Greengard [4], and the low-frequency fast inhomogeneous plane wave algorithm (LF-FIPWA) for wide-band fast computations [5, 6]. However, much memory is required for LF-FIPWA, since evanescent waves are highly direction dependent.

The fast multipole algorithm is numerically unstable due to the oscillatory characteristic of the spherical Hankel function for small arguments. As an attempt for a possible remedy, the mixed-form fast multipole algorithm (MF-FMA) [3, 7] is proposed to cover a wide band from the

1054-4887 © 2010 ACES

low-frequency to mid-frequency. However, it is noticed that the MF-FMA need to construct multipole expansions for each nonempty boxes at the low frequency regime [3, 7]. As a result, the finest level boxes' size will all be less than 0.2λ ("λ" stands for wavelength). This results in a source distribution of high-density for the whole object. However, AMF-FMA just applies MF-FMA for some part of the object which belongs to the low frequency regime and the rest of the object which belongs to the mid frequency regime is still analyzed by MLFMA. Hence for an object containing fine structure, AMF-FMA takes advantage of adaptive grouping scheme [8, 13] to set the finest level box size smaller than 0.2λ for fine structure while for the rest of the object, the finest level box size is larger than 0.2λ. This frees MLFMA from low-frequency breakdown. As a result, the characteristics of both long-wavelength and short-wavelength are considered simultaneously for the object. In this way, the proposed algorithm is memory efficient since the adaptive grouping scheme is used.

This paper is organized as follows. Section II gives a brief introduction to the processing of near interaction of MF-FMA and the EFIE formulation in electromagnetic wave scattering. Section III describes the theory and implementation of the adaptive MF-FMA in more details. Numerical experiments with a few electromagnetic wave scattering problems are presented to demonstrate the efficiency of the AMF-FMA in Section IV. Section V gives some conclusions and comments.

II. EFIE FORMULATION

The EFIE formulation of electromagnetic wave scattering problems using planar Rao-Wilton-Glisson (RWG) basis functions for surface modeling is presented in [13]. The resulting linear systems from EFIE formulation after Galerkin's testing are briefly outlined as follows:

$$\sum_{n=1}^{N} Z_{mn} a_n = V_m, \qquad \mathrm{m} = 1, 2, ..., N, \qquad (1)$$

where

$$Z_{mn} = \frac{jk\eta}{4\pi} \iint_s \mathbf{f}_m(\mathbf{r}) \cdot \iint_s G(\mathbf{r}, \mathbf{r}') \mathbf{f}_n(\mathbf{r}') dS' dS$$

$$- \frac{j\eta}{4\pi k} \iint_s \nabla \bullet \mathbf{f}_m(\mathbf{r}) \cdot \iint_s G(\mathbf{r}, \mathbf{r}') \nabla \bullet \mathbf{f}_n(\mathbf{r}') dS' dS,$$

and

$$V_m = \int_s \mathbf{f}_m(\mathbf{r}) \cdot \mathbf{E}^i(\mathbf{r}) ds, \quad G(\mathbf{r}, \mathbf{r}') = \frac{e^{-jk|\mathbf{r}-\mathbf{r}'|}}{4\pi |\mathbf{r}-\mathbf{r}'|}.$$

Here, $G(\mathbf{r}, \mathbf{r}')$ refers to the Green's function in free space and $\{a_n\}$ is the column vector containing the unknown coefficients of the surface current expansion with RWG basis functions. Also, as usual, $\mathbf{r}$ and $\mathbf{r}'$ denote the observation and source point locations. $\mathbf{E}^i(\mathbf{r})$ is the incident excitation plane wave, and η and k denote the free space impendence and wave number, respectively. Once the matrix equation (1) is solved by numerical matrix equation solvers, the expansion coefficients $\{a_n\}$ can be used to calculate the scattered field and RCS. In the following, we use $\mathbf{A}$ to denote the coefficient matrix in equation (1), $\mathbf{x} = \{a_n\}$, and $\mathbf{b} = \{V_m\}$ for simplicity. Then, the EFIE matrix equation (1) can be symbolically rewritten as:

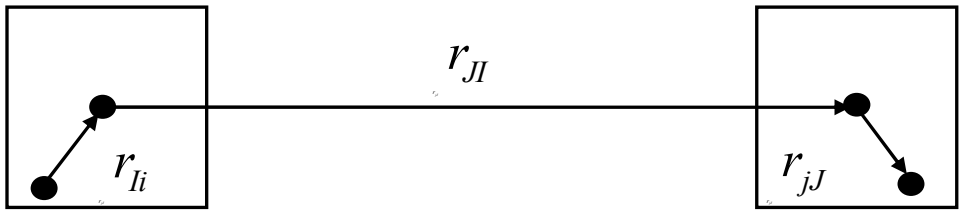

Fig. 1. The general translation used for LF-FMA.

$$\mathbf{Ax} = \mathbf{b}. \qquad (2)$$

To solve the above matrix equation by an iterative method, the matrix-vector products are

needed at each iteration. Physically, a matrix-vector product corresponds to one cycle of interactions between the basis functions. The basic idea of the mixed-form FMA (MF-FMA) is to combine the LF-FMA with the MLFMA into one uniform expression and convert the interaction of element-to-element to the interaction of group-to-group. Here, a group includes the elements residing in a spatial box. The mathematical foundation of the mixed-form FMA is, also, the addition theorem for the scalar Green's function in free space. Using the MF-FMA, the matrix-vector product $\mathbf{Ax}$ can be written as:

$$\mathbf{Ax} = \mathbf{A}_N\mathbf{x} + \mathbf{A}_F\mathbf{x}.$$

Here, $\mathbf{A}_N$ is the near part of $\mathbf{A}$ and $\mathbf{A}_F$ is the far part of $\mathbf{A}$.

In the MF-FMA, the calculation of matrix elements in $\mathbf{A}_N$ remains the same as in the MoM procedure. However, those elements in $\mathbf{A}_F$ are not explicitly computed and stored. Hence, they are not numerically available in the MF-FMA.

III. ADAPTIVE MIXED-FORM FAST MULTIPOLE ALGORITHM

It is well known that the diagonalized translation matrix of the 3-D MLFMA can greatly decrease the memory requirements and expedite the matrix-vector multiplication. However, it can not avoid low-frequency breakdown [3, 4]. In order to overcome the low-frequency breakdown, the low-frequency fast multipole algorithm (LF-FMA) is developed [12] and it bridges the gap from static to electrodynamic.

A. Low-frequency fast multipole algorithm

As shown in Fig. 1, $\boldsymbol{r}_{ji} = \boldsymbol{r}_{jJ} + \boldsymbol{r}_{JI} + \boldsymbol{r}_{Ii}$ and the addition theorem [3, 9, 10] is utilized for LF-FMA. The general translation equation is obtained as follows:

$$\alpha_{LL'}\left(\mathbf{r}_{ji}\right) = \sum_{L_1}\sum_{L_2}\beta_{LL_1}\left(\mathbf{r}_{jJ}\right)\alpha_{L_1L_2}\left(\mathbf{r}_{JI}\right)\beta_{L_2L'}\left(\mathbf{r}_{Ii}\right) \tag{3}$$

The above equation is a recursive equation and $L = (l, m), 0 \le l \le \mathrm{P}, -l \le m \le l$, P is truncation number of multipoles. Here, L_1, L_2 and L' have similar definitions as L. L and L' are used as the subscripts for the α operator and the β operator. $\alpha_{LL'}$ and $\beta_{LL'}$ are defined as

$$\alpha_{L',L}\left(\mathbf{r}\right) = \sum_{L''} 4\pi(-j)^{(l'+l''-l)}\Psi_{L''}\left(k,\mathbf{r}\right)A_{L,L',L''} \tag{4}$$

$$\beta_{L',L}\left(\mathbf{r}\right) = \sum_{L''} 4\pi(-j)^{(l'+l''-l)}\Re_g\Psi_{L''}\left(k,\mathbf{r}\right)A_{L,L',L''}, \tag{5}$$

where

$$\begin{aligned}\Psi_L\left(k,\mathbf{r}\right) &= h_l^{(2)}\left(kr\right)Y_l^m\left(\theta,\phi\right)\\ \Re_g\Psi_L\left(k,\mathbf{r}\right) &= j_l\left(kr\right)Y_l^m\left(\theta,\phi\right).\end{aligned} \tag{6}$$

$A_{L,L',L''}$ is the Gaunt coefficient, $h_l^{(2)}\left(x\right)$ is the spherical Hankel function of the second kind, $Y_l^m\left(\theta,\phi\right)$ is the spherical harmonic function [10, 11].

$G(\boldsymbol{r}_j, \boldsymbol{r}_i)$ is free space green's function and corresponds to $\alpha_{00}(\boldsymbol{r}_{ji})$

$$G\left(\mathbf{r}_j,\mathbf{r}_i\right) = -jk\alpha_{00}\left(\mathbf{r}_{ji}\right). \tag{7}$$

B. Adaptive mixed-form fast multipole algorithm

LF-MLFMA is developed for very low-frequency problems based on the non-diagonalized form of the fast multipole translator and the multipoles are efficient in grouping and translating waves among much smaller objects or boxes [3, 7]. However, LF-MLFMA will lose its accuracy and efficiency when the box size is above 0.2λ. Multipoles and plane waves are combined into one octree browsing process to form the MF-FMA for the efficient analysis in both low frequency and mid-frequency bands. When the frequency is low, or the MLFMA box sizes are small compared to wavelength, the non-diagonalized form of the fast multipole translator is used. When the box sizes are comparable to wavelength, the diagonalized form of the fast multipole (plane wave) translator is used for translation. In this manner, the

multilevel algorithm can efficiently work for box sizes to be a small fraction of a wavelength and the whole simulation objects can be electrically large enough when compared to wavelength.

The fast multipole translator $\alpha_{LL'}$ is always in the form of dense matrix and can be diagonalized into the plane wave integrations (8) and (9).

Inserting (9) into (3), the Mixed-form translation containing two-level multipoles translation and two-level diagonal translation in the form of matrix is obtained in (10) below, where S_i is a sample number of propagating waves over a unit sphere at a level for diagonal translations, [$\boldsymbol{I}$] is the interpolation matrix and [$\boldsymbol{I}$]$^{\mathrm{T}}$ denotes the transpose of matrix [$\boldsymbol{I}$]. J_i and I_i denote the different boxes in "i" level. "Diag" is short for the diagonal translation matrix. [$\boldsymbol{D}$]$_{S\times L}$ is transformer from multipoles to plane waves, and $\left[\boldsymbol{D}\right]^{\dagger}_{S\times L}$ is transformer from plane waves to multipoles [7].

$$\alpha_{LL'}\left(\mathbf{r}_{ji}\right)=\int d\Omega_k\,(-j)^{l}\,Y_L^{*}\left(\Omega_k\right)e^{-j\mathbf{k}\cdot\mathbf{r}_{JJ}}\,\tilde{T}_{JI}\left(\Omega_k,\boldsymbol{r}_{JI}\right)(-j)^{-l'}\,Y_{L'}\left(\Omega_k\right)e^{-j\mathbf{k}\cdot\mathbf{r}_{Ii}} \tag{8}$$

$$\tilde{T}_{JI}\left(\Omega_k,\Omega'_k\right)=\sum_{l=0}^{L_{\max}}(-j)^{l}\,(2l+1)\,h_{l''}^{(2)}\left(kr_{JI}\right)P_l\left(\hat{k}\bullet\hat{\boldsymbol{r}}_{\boldsymbol{JI}}\right) \tag{9}$$

$$\begin{aligned}\left[\alpha_{LL'}\left(\mathbf{r}_{ji}\right)\right]_{L\times L'}=&\left[\beta_{LL_1}\left(\mathbf{r}_{jJ_1}\right)\right]_{L\times L_1}\cdot\left[\beta_{L_1L_2}\left(\mathbf{r}_{J_1J_2}\right)\right]_{L_1\times L_2}\\&\cdot\left[\boldsymbol{D}\right]^{\dagger}_{S_3\times L_2}\cdot diag\left[e^{-j\mathbf{k}\cdot\mathbf{r}_{J_2J_3}}\right]_{S_3\times S_3}\cdot\left[\boldsymbol{I}\right]^{\mathrm{T}}_{S_4\times S_3}\cdot diag\left[e^{-j\mathbf{k}\cdot\mathbf{r}_{J_3J_4}}\right]_{S_4\times S_4}\\&\cdot diag\left[\tilde{T}\left(\Omega_{s4},\boldsymbol{r}_{J_4I_4}\right)\omega_{S_4}\right]_{S_4\times S_4}\\&\cdot diag\left[e^{-j\mathbf{k}\cdot\mathbf{r}_{I_4I_3}}\right]_{S_4\times S_4}\cdot\left[\boldsymbol{I}\right]_{S_4\times S_3}\cdot diag\left[e^{-j\mathbf{k}\cdot\mathbf{r}_{I_3I_2}}\right]_{S_3\times S_3}\cdot\left[\boldsymbol{D}\right]_{S_3\times L_2}\\&\cdot\left[\beta_{L_2L_1}\left(\mathbf{r}_{I_2I_1}\right)\right]_{L_2\times L_1}\cdot\left[\beta_{L_1L'}\left(\mathbf{r}_{I_1i}\right)\right]_{L_1\times L'}\end{aligned} \tag{10}$$

$$\begin{aligned}\frac{e^{-jkr_{ji}}}{r_{ji}}&=-jk\alpha_{00}\left(\mathbf{r}_{ji}\right)\\&=-jk\left[\beta_{0L_1}\left(\mathbf{r}_{jJ_1}\right)\right]_{1\times L_1}\cdot\left[\beta_{L_1L_2}\left(\mathbf{r}_{J_1J_2}\right)\right]_{L_1\times L_2}\\&\cdot\left[\boldsymbol{D}\right]^{\dagger}_{S_3\times L_2}\cdot diag\left[e^{-j\mathbf{k}\cdot\mathbf{r}_{J_2J_3}}\right]_{S_3\times S_3}\cdot\left[\boldsymbol{I}\right]^{\mathrm{T}}_{S_4\times S_3}\cdot diag\left[e^{-j\mathbf{k}\cdot\mathbf{r}_{J_3J_4}}\right]_{S_4\times S_4}\\&\cdot diag\left[\tilde{T}\left(\Omega_{S_4},\boldsymbol{r}_{J_4I_4}\right)\omega_{S_4}\right]_{S_4\times S_4}\\&\cdot diag\left[e^{-j\mathbf{k}\cdot\mathbf{r}_{I_4I_3}}\right]_{S_4\times S_4}\cdot\left[\boldsymbol{I}\right]_{S_4\times S_3}\cdot diag\left[e^{-j\mathbf{k}\cdot\mathbf{r}_{I_3I_2}}\right]_{S_3\times S_3}\cdot\left[\boldsymbol{D}\right]_{S_3\times L_2}\\&\cdot\left[\beta_{L_2L_1}\left(\mathbf{r}_{I_2I_1}\right)\right]_{L_2\times L_1}\cdot\left[\beta_{L_10}\left(\mathbf{r}_{I_1i}\right)\right]_{L_1\times 1}\end{aligned} \tag{11}$$

$$\frac{e^{-jkr_{ji}}}{r_{ji}} = diag\left[e^{-j\mathbf{k}\cdot\mathbf{r}_{J_jJ_3}}\right]_{S_3\times S_3}\cdot\left[\boldsymbol{I}\right]^{\mathrm{T}}_{S_4\times S_3}\cdot\ diag\left[e^{-j\mathbf{k}\cdot\mathbf{r}_{J_3J_4}}\right]_{S_4\times S_4}$$
$$\cdot\ diag\left[\tilde{T}\left(\Omega_{S_4},\mathbf{r}_{J_4I_4}\right)\omega_{S_4}\right]_{S_4\times S_4} \tag{12}$$
$$\cdot\ diag\left[e^{-j\mathbf{k}\cdot\mathbf{r}_{I_4J_3}}\right]_{S_4\times S_4}\cdot\left[\boldsymbol{I}\right]_{S_4\times S_3}\cdot\ diag\left[e^{-j\mathbf{k}\cdot\mathbf{r}_{I_3j}}\right]_{S_3\times S_3}.$$

The free space Green's function is expanded by mixed-form translation through equation (10) as (11) above, and the free space Green's function is expanded by plane wave translation for MLFMA as (10) above.

It can be found from the above equations that both the LF-MLFMA and the MF-FMA uses the same grouping structure as MLFMA. Therefore, the simulated object is first enclosed by the smallest possible box, called root boxes. Then the root box is divided into eight equal boxes and each of the child boxes is recursively subdivided into eight smaller boxes until we reach the finest level. For MF-FMA, when the multipole expansion is applied for each nonempty box in the finest level, it is inevitable to produce a large number of unknowns because of the source distribution for the whole object is high-density at the low-frequency regime and the number of the finest level box is consequentially larger than

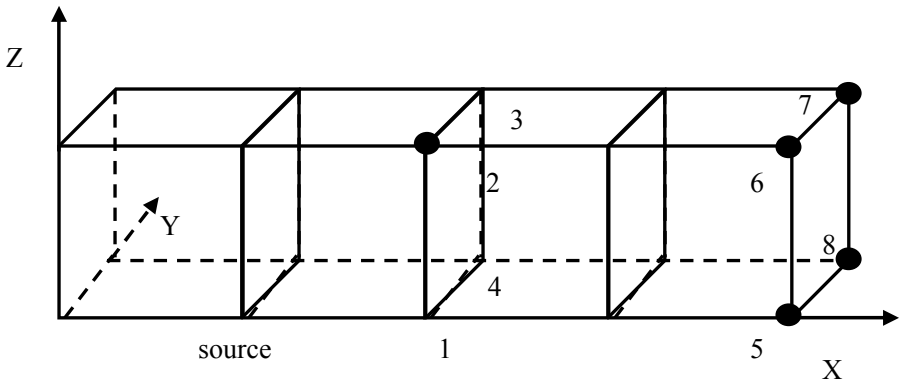

Fig. 2. Point positions.

MLFMA. Therefore, the MF-FMA is not necessary for the whole object but only used for the fine structures connected with the electrically large object.

In the conventional grouping scheme described above, the parent boxes are divided regardless of the number of sources inside them [9]. However, for some fraction of the object, the source distribution is high-density and it is in fact a low-frequency problem. As a result, the uniform partitioning often leads to the whole object divided with the same resolution and the simulation result is not accurate. When MF-FMA is used for the object, the box size of finest level can be smaller than 0.2λ, but source distribution is high-density for the whole object. To improve the efficiency of the method, the MF-FMA is applied for fine structures of the object which is considered at the low-frequency regime and the conventional MLFMA is used for the rest of the object which is considered in the mid-frequency regime. As MF-FMA and MLFMA is used at the same time, the size of leafy groups is not always the same. Therefore, a new grouping scheme has to be developed.

Different from the method described in [12], if a box doesn't contain sources in the low-frequency regime, it will be considered as a leaf box and the subdivision is terminated for that box, otherwise it will continue to be divided until satisfying the low-frequency grouping requirement. The following text gives a tree

structure where the leaf boxes can be in any of the refinement levels. The pseudocode of the adaptive tree construction is given as follows:

Algorithm I: Adaptive tree structure

Step 1: Enclose the sources in the smallest possible box (computational domain)

Step 2: Decompose the computational domain to eight equal child boxes

Step 3: For each child box k, **do** k = 1 to 8

Step 4: **If** it contains no source, **then** eliminate it,

Step 5: **If** it contains sources that belong to the mid-frequency regime and the box size is 0.2λ, **then**

Step 6: The box is considered a mid-frequency leaf box and is not further divided

Step 7: **end if**

Step 8: **else**

Step 9: Divide it into its 8 child boxes

Step 10: **end if**

Step 11: **end do**

Step 12: Repeat until the boxes at the finest level agree with the low-frequency requirement.

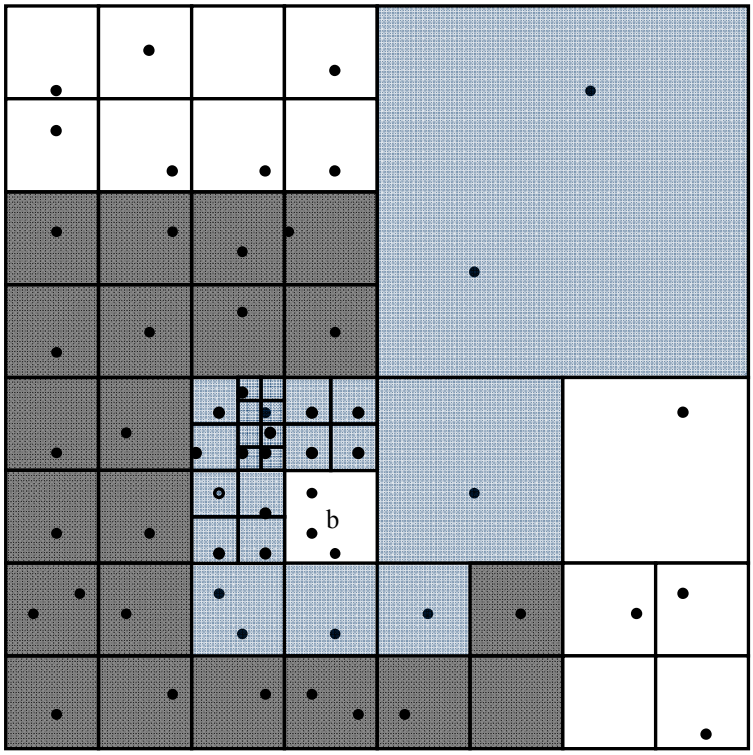

Fig. 3. Adaptive grouping.

In the adaptive scheme, the interaction sublists for the boxes are formed similar to the traditional fast multipole algorithm. As the leaf boxes can be in any of the refinement levels, the construction of the near list is more involved. To define the near list, we consider a box i at level l. The descents of box i are boxes in levels l_d, $l_d < l$, that are contained in box i. These include the children, grandchildren etc. of box i. The ancestors of box i are boxes in levels l_a, $l_a > l$, that contain box i.

For each leaf box b, we define the following sets of boxes:

1. The leaf boxes which are descents of box b's near neighbors, which is denoted by the set N_d.
2. The leaf boxes which are near neighbors of box b's ancestors, which is denoted by the set N_a.
3. The leaf boxes which are near neighbors of box b, denoted by the set N_n . The near list of a leaf box b consists of boxes b_n, where b_n belongs to $\{ N_n \cup N_a \cup N_d \}$.

As is shown in Fig. 3, the adaptive partitioning of the computational domain for a nonuniform distribution of sources is shown in two

dimensions. Consider a leaf box b, the boxes in the near list are lightly shaded, and the boxes in deep color are b's far groups.

Usually, the mesh density for the small cylinder is higher than the cubic for the object shown in Fig. 5. As a result, if the box size is set 0.2λ for the finest level, it will contain many elements in a box which results in large memory consumption for the near interaction matrix. To alleviate the press of near interaction, according to the adaptive grouping scheme in [8, 12] and making some modification as the above description, MF-FMA is applied for in the purple small cylinder and MLFMA is applied for in the cubic at the bottom. Thus, the finest level box size for the MF-FMA can be set smaller than 0.2λ while the finest level box size is at least 0.2λ for MLFMA.

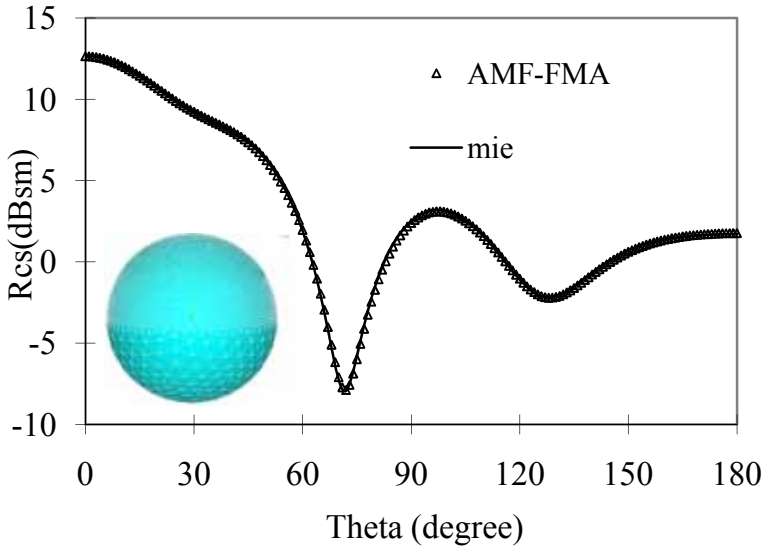

Fig. 4. Bistatic RCS of a PEC sphere working at 0.18 GHz simulated by Mie series and adaptive mixed-form FMA.

IV. NUMERICAL RESULTS

In this section, several numerical examples are presented to demonstrate the efficiency of adaptive MF-FMA (AMF-FMA) for fast analysis of electromagnetic scattering. All experiments are performed on a Core-2 6300 with 1.86 GHz CPU and 1.96GB RAM in single precision. The iteration process is terminated when the normalized backward error is reduced by 10^{-3} for all examples.

In the implementation of the MF-FMA, the adaptive grouping method is used to reduce the memory consumption and captures the fine details of the structure. The incident wave is considered to be a plane wave at $\theta = 0.0$, $\varphi = 0.0$. All geometries are modeled by plane triangles panels. As shown in Fig. 4, the numerical results of bistatic RCS for vertical polarization are given to illustrate the performance of our AMF-FMA. It consists of a sphere with radius 1m at 180MHz, and the average element size is 0.048 for the top half sphere with 3042 unknowns while the average element size is 0.06 for the bottom half sphere with 843 unknowns. The MF-FMA and MLFMA are applied to the top half sphere and the bottom, respectively. The numerical result of AMF-FMA is compared with the Mie series and we can see the result agrees with the Mie series vigorously.

In Fig. 6, the geometry is a cube connected with a small cylinder with 11862 unknowns. The size of the cube is 1m × 1m× 1m with a small cylinder whose radius is 0.03m and the height is 1m. The average element size is 0.03 for the small cylinder with 826 unknowns and the cubic is 0.043 at 300MHz. The numerical results of the

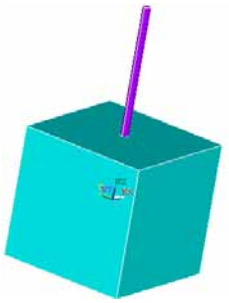

Fig. 5. A cubic with a small cylinder.

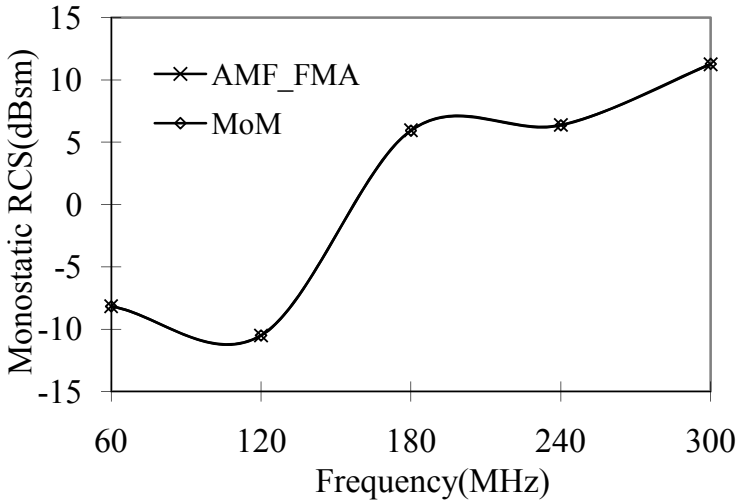

Fig. 6. Monostatic RCS of the cube-cylinder simulated by MoM and adaptive mixed-form FMA.

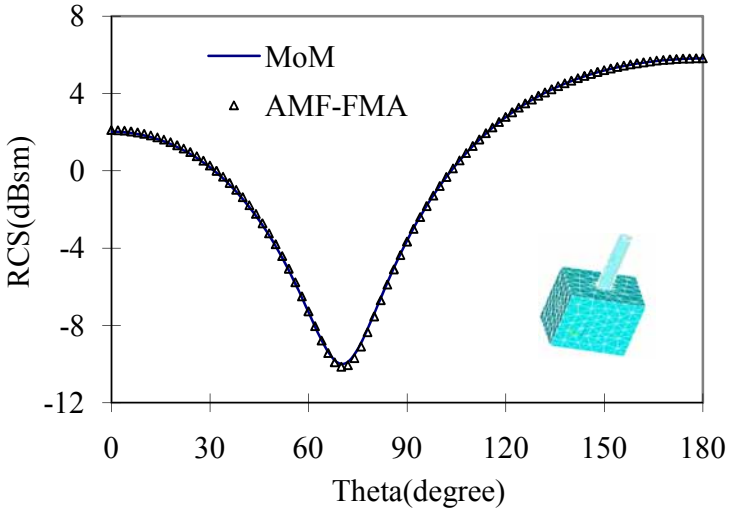

Fig.7. Bistatic RCS of the cube-cylinder working at 60MHz simulated by MoM and adaptive mixed-form FMA.

monostatic RCS for vertical polarization are given to illustrate the performance of our AMF-FMA at 60 MHz, 120 MHz, 180 MHz, 240 MHz, and 300MHz. The finest level box size corresponding to the frequencies is 0.05λ, 0.05λ, 0.15λ, 0.1λ, and 0.125λ.

Two levels LF-FMA is applied for the whole object at 60 MHz. Mixed-form translation containing two levels multipoles translation and one level diagonal translation is utilized for the small cylinder and the cubic is analyzed by one level MLFMA at 120 MHz. For 180 MHz and 240 MHz, mixed-form translation containing one level multipoles translation and one level diagonal translation is used for the small cylinder and the cubic is analyzed by one level MLFMA. At 300MHz, mixed-form translation containing one level multipoles translation and two levels diagonal translation is used for the small cylinder while the cubic is analyzed by two levels MLFMA.

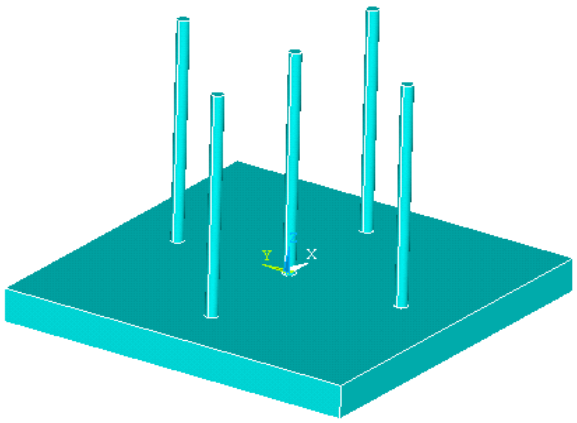

Fig. 8. A cuboid with many fine structures.

At 60 MHz, the electrical size of the cube-cylinder is 0.4λ and the average element size is 0.006 for the small cylinder and 0.0086 for the cubic. AMF-FMA degenerates to two levels LF-FMA with the finest level box size is 0.05λ. It is shown in Fig. 7 that the result has a good agreement with MoM.

When the proportion of fine structures in an object goes up as shown in Fig. 8, the total memory consumption for MLFMA and AMF-FMA is described in Fig. 9. The cuboid of the object in Fig. 8 is of the size 3m×3m×0.5m and the small cylinders are all in the same size with radius 0.05m and the height 2m. The average element size for the cuboid is around 0.093 and set the average element size for all cylinders varies from 0.033 to 0.01, corresponding with the unknowns from 8490 to 49011.The box size at the finest level for MLFMA is set 0.25λ. The finest level box sizes of AMF-FMA are 0.05λ for fine structures and 0.2λ for the rest of the object at 200 MHz. Using AMF-FMA for the object, MF-FMA is applied for the cylinders and MLFMA is for the cuboid. With the total number of unknowns increasing, it can be seen from Fig. 9(a) that the memory consumption of storage near part matrix

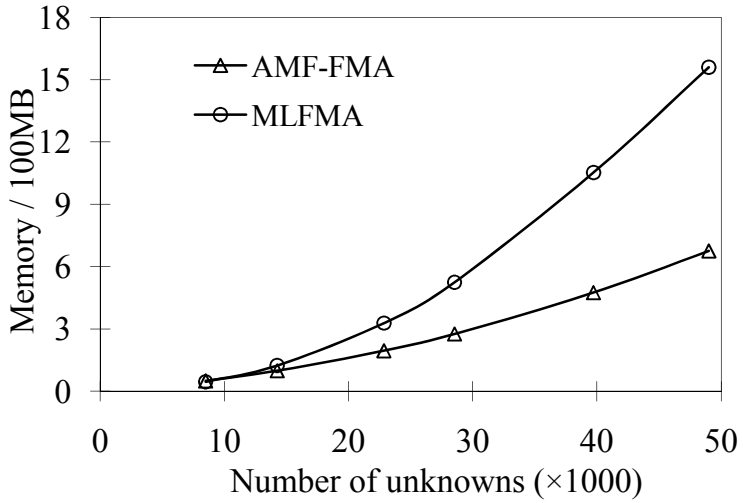

(a)

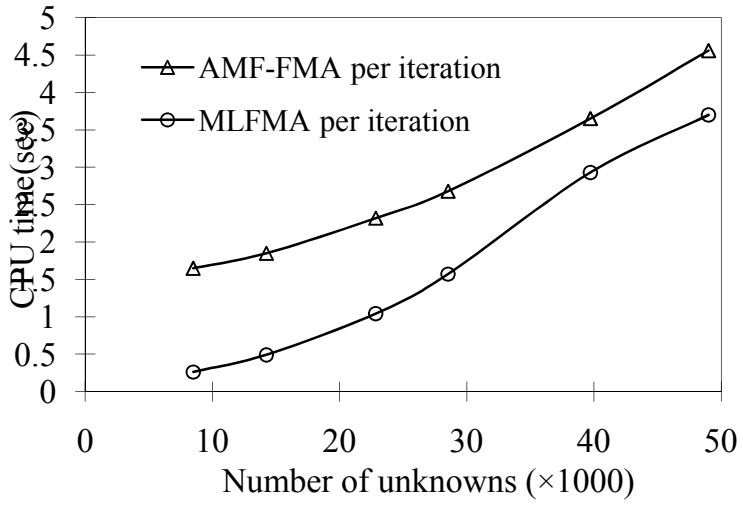

(b)

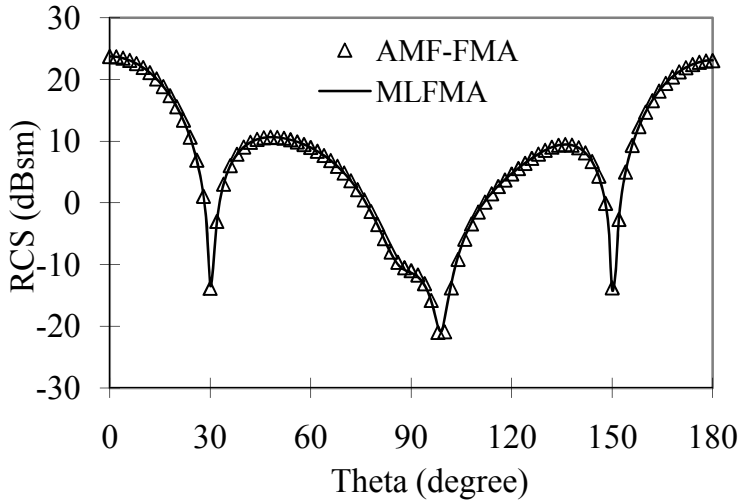

(c)

Fig. 9. (a) The memory consumption of the object shown in Fig. 8 between AMF-FMA and MLFMA, (b) CPU times for one matrix-vector operation versus the number of unknowns for the object shown in Fig. 8, and (c) bistatic RCS of the object shown in Fig. 8 simulated by MLFMA and AMF-FMA at 200MHz.

elements of $\mathbf{A}_N$ is large for MLFMA when leaf box size is 0.25λ. In other words, the more unknowns for the fine structures, the less memory requirement for AMF-FMA compared with MLFMA. In Fig. 9(b), it can be seen that the CPU time of AMF-FMA for one matrix-vector operation is more than MLFMA, but the CPU time consumption of AMF-FMA is close to MLFMA with the increasing of the unknowns for the fine structures. In Fig. 9(c), the bistatic RCS of the object in Fig. 8 for vertical polarization is given at 200 MHz with the unknowns 8490.

It can be seen from the figure that the result of AMF-FMA agrees with MLFMA vigorously.

Table 1: Test the LF-FMA translator

Source point	Field point	Green's function	Multipoles expansion
(0, 0, 0.)	(1.0, 0, 0.)	(0.9980267,-6.2790520E-02)	(0.9917871,-6.2790506E-02)
(0, 0, 0.)	(1.0,0.5,0.)	(0.8922212,-6.2780187E-02)	(0.8950982,-6.2780164E-02)
(0, 0, 0.)	(1.0,0.5,0.5)	(0.8140802,-6.2769860E-02)	(0.8088611,-6.2769853E-02)
(0, 0, 0.)	(1.0,0.,0.5)	(0.8922212,-6.2780187E-02)	(0.8950983,-6.2780179E-02)

Table 2: Test the MF-FMA translator

Source point	Field point	Green's function	Multipole expansion
(0.25,0,0)	(1,0.1,0)	(-0.4293182,-1.249964)	(-0.4293646,-1.249869)
(0.25,0,0)	(1,0.24,0.24)	(-0.5804493,-1.067079)	(-0.5811364,-1.066991)
(0.25,0,0)	(1.24,0.24,0.24)	(-0.8333122,-0.4675281)	(-0.8338917,-0.4674568)
(0.25,0,0)	(1.24,0,0.25)	(-0.8216858,-0.5328912)	(-0.8221112,-0.5328190)

In Tables 1 and 2, we test the accuracy of equation (6) and equation (10). In Table 1, we choose the leafy box size is 0.5m and the source point is located at (0, 0, 0.). We take field point at 1, 2, 3, 4, as shown in Fig. 2, the frequency is 0.003GHz. In Table 2, we choose the leafy box is 0.25m and the frequency is 0.12GHz. The source point is fixed at (0.25, 0, 0.) and the field points are selected at random. From the two tables, we can conclude that the error of the results is no more than 1%.

V. CONCLUSIONS

In this paper, we have described an adaptive grouping scheme combined with MF-FMA (AMF-FMA) for solving electromagnetic wave scattering problems. One advantage of our presented AMF-FMA is that it can cover a wide band from low frequency to mid-frequency without low-frequency breakdown. Another improvement is that for the object with fine structures, combined with adaptive grouping method, MF-FMA and MLFMA can be used flexibly for different parts of the object simultaneously. MF-FMA is applied for capturing the fine details of the structure accurately, and MLFMA is implemented for the rest of the object. As a result, the memory consumption is greatly reduced compared with MLFMA. Numerical results are performed and compared to verify the AMF-FMA is flexible and efficient.

ACKNOWLEDGMENT

We would like to thank the support of Major State Basic Research Development Program of China (973 Program: 2009CB320201); Natural Science Foundation of 60871013, 60701004, 60928002; Jiangsu Natural Science Foundation of BK2008048.

REFERENCES

[1] S. M. Rao, D. R. Wilton, and A. W. Glisson, "ELectromagnetic scattering by surfaces of arbitrary shape," *IEEE Transactions on Antennas and Propagation.*, vol. 30, no. 3, pp. 409-418, May 1982.

[2] J. M. Jin, *The Finite Element Method in Electromagnetics,* 2nd ed., John Wiley & Sons, Inc., 2002.

[3] W. C. Chew, J. M. Jin, Eric Michielssen, and J. M. Song, *Fast and Efficient Algorithms in Computational*

Electromagnetics, Artech House Publishers, 2001.

[4] L. Greengard, J. F. Huang, V. Rokhlin, and S. Wandzura, "Accelerating fast multipole methods for the Helmholtz equation at low frequencies," *IEEE Comput. Sci. Eng.*, vol. 5, no. 3, pp. 32-38, Jul.-Sep. 1998.

[5] L. J. Jiang and W. C. Chew, "Broad-band fast computational electromagnetics algorithm- MFIPWA," *Proc. 19th Annual Review of Progress in Applied Computational Electromagetics*, pp. 36-41, Mar. 2003.

[6] L. J. Jiang and W. C. Chew, "Low-frequency fast inhomogeneous plane-wave algorithm (LF-FIPWA)," *Microw. Opt. Technol. Lett.*, vol. 40, no. 2, pp. 117-122, Jan. 20, 2004.

[7] L. J. Jiang and W. C. Chew, "A Mixed-Form Fast Multipole Algorithm," *IEEE Transactions on Antennas and Propagation,* vol. 53, no. 12, pp. 4145- 4156, Dec.2005.

[8] H. Cheng, L. Greengard, and V. Rokhlin, "A fast Adaptive multipole algorithm in three dimensions," *J. Comput. Phys.*, vol. 155, pp. 468-498, 1999.

[9] L. Greengard and V. Rokhlin, "A fast algorithm for particle simulation," *J. Comput. Phys.*, vol. 73, pp. 325-348, 1987.

[10] J. S. Zhao and W. C. Chew, "Three dimensional multilevel fast multipole algorithm from static to electrodynamic," *Micro. Opt. Technol. Lett.*, vol. 26, no. 1, pp. 43-48, 2000.

[11] J. S. Zhao and W. C. Chew, "A succinct way to diagonalize the translation matrix in three dimensions," *Micro. Opt. Technol. Lett.*, vol. 15, no. 3, pp. 144-147, 1997.

[12] S. Ayatollahi and M. Safayi Naeini, "Adaptive plane-wave expansion algorithm for efficient computation of electromagnetic fields in low-frequency problems," *Microwaves, Antennas and Propagation, IEE Proceedings*, no. 3, pp.182-190, 2006.

[13] L. J. Jiang, *Studies on low frequency fast multipole algorithms,* Ph.D. Dissertation, University of Illinois, Urbana, 2004.

[14] D. R. Wilton and A. W. Glisson, "On improving the electric field integral equation at low frequencies," *1981 Spring URSI Radio Science Meeting Digest*, pp. 24, June 1981.

[15] J. R. Mautz and R. F. Harrington, "An E-field solution for a conducting surface small or comparable to the wavelength," *IEEE Transactions on Antennas and Propagation.*, vol. 32, no. 4, pp. 330-339, April 1984.

Hua Chen was born in Anhui Province, China. She received the B.S. degree in Electronic Information Engineering from Anhui University, China, in 2005, and is currently working toward the Ph.D. degree at Nanjing University of Science and Technology (NJUST), Nanjing, China. Her current research interests include computational electromagnetics, antennas and electromagnetic scattering and propagation, electromagnetic modeling of microwave integrated circuits.

Zhen-Hong Fan was born in Jiangsu, the People's Republic of China in 1978. He received the M.Sc. and Ph.D. degrees in Electromagnetic Field and Microwave Technique from Nanjing University of Science and Technology (NJUST), Nanjing, China, in 2003 and 2007, respectively. During 2006, he was with the Center of Wireless Communication in the City University of Hong Kong, Kowloon, as a Research Assistant. He is currently an Associated Professor with the Electronic Engineering of NJUST. He is the author or coauthor of over 20 technical papers. His current research interests include computational electromagnetics, electromagnetic scattering, and radiation.

Ru-Shan Chen (M'01) was born in Jiangsu, P. R. China. He received his B.Sc. and M.Sc. degrees from the Dept. of Radio Engineering, Southeast University, in 1987 and in 1990,

respectively, and his Ph.D. from the Dept. of Electronic Engineering, City University of Hong Kong in 2001. He joined the Dept. of Electrical Engineering, Nanjing University of Science & Technology (NJUST), where he became a Teaching Assistant in 1990 and a Lecturer in 1992. Since September 1996, he has been a Visiting Scholar with the Department of Electronic Engineering, City University of Hong Kong, first as Research Associate, then as a Senior Research Associate in July 1997, a Research Fellow in April 1998, and a Senior Research Fellow in 1999. From June to September 1999, he was also a Visiting Scholar at Montreal University, Canada. In September 1999, he was promoted to Full Professor and Associate Director of the Microwave & Communication Research Center in NJUST and in 2007, he was appointed Head of the Dept of Communication Engineering, Nanjing University of Science & Technology. His research interests mainly include microwave/millimeter-wave systems, measurements, antenna, RF-integrated circuits, and computational electromagnetics. He is a Senior Member of the Chinese Institute of Electronics (CIE).

Zhao-Neng Jiang was born in Jiangsu Province, the People's Republic of China in 1985. He received the B.S. degree in Physics from Huaiyin Normal College in 2007, and is currently working toward the Ph.D. degree at Nanjing University of Science and Technology. His research interests focus on fast solution of integral equations, electromagnetic scattering, and propagation.

Meng-Meng Li was born in Jiangsu Province, the People's Republic of China in 1984. He received the B.S. degree in Physics from Huaiyin Normal College in 2007, and is currently working toward the Ph.D. degree at Nanjing University of Science and Technology. His research interests focus on fast solution of integral equations, modeling of microwave integrated circuits, and UWB antennas.

Improved Microstrip Folded Tri-Section Stepped Impedance Resonator Bandpass Filter using Defected Ground Structure

Nima Molaei Garmjani and Nader Komjani

Department of Electrical Engineering
Iran University of Science & Technology (IUST), Tehran, Iran
nima_molaei@yahoo.com, n_komjni@iust.ac.ir

Abstract ─ In this paper, a study of a microwave microstrip bandpass filter (BPF), based on folded tri-section stepped impedance resonator (FTSIR) and defected ground structure (DGS) is presented. Based on the resonance characteristics of a stepped impedance resonator (SIR), the first spurious resonant frequency can be tuned over a wide range by adjusting its structure parameters. The SIR bandpass filter is designed to have a quasi-elliptic function response and a wide upper stopband. Furthermore, five ground slots (DGS) are used in order to omit the first spurious resonant frequency. Compared to similar microstrip filter without defected ground, the simulated performances of this novel structure indicate some functional advantages. To validate the design and analysis, a prototype of the bandpass filter with DGS was fabricated and measured. It is shown that the measured and simulated performances are in a good agreement.

Index Terms ─ Defected ground structure (DGS), folded tri-section stepped impedance resonator (FTSIR), microstrip bandpass filter.

I. INTRODUCTION

By using a SIR the first and second spurious response can be pushed far beyond $2f_0$ and $3f_0$, respectively (where f_0 is the fundamental resonant frequency); this is achieved by properly choosing the impedance ratio. In addition, bandpass filters based on stepped impedance resonators usually have high selectivity and low internal losses in pass band width. For this reason, these filters are extensively used in a most of the communication applications nowadays. Stepped impedance resonators are use in circuits like duplexers and mixers because they have smaller dimensions, relative to conventional resonators, and high quality factor.

There are many types of transfer functions for filters (Butterworth, Chebyshev, Elliptic, Quasi-elliptic, etc.). Among these different types, filters with quasi-elliptic transfer function have higher selectiveness, because of having the same ripples in pass band and high slope nearby transmission zeros. In addition, the ability to create transfer zeros in nearby of pass band causes to improve the slope of reject band. So, quasi-elliptic filters are extensively used in modern applications.

Poles degree of the filter and consequently the quantity of resonators must be increased in order to obtain higher selectiveness, but internal losses increase because resonators are not ideal. Here, in the design process of SIR filters, we have used quasi-elliptic four-pole cross-coupled resonators (reciprocal coupling between nonadjacent resonators) in order to obtain high selectiveness and decrease the internal loss. Whereas the first spurious resonant frequency is near to pass band in this structure, we have to consider an approach to eliminate it. The selected approach to eliminate the first spurious resonant frequency is etching defects in the ground plane of the structure.

In [1], a FTSIR bandpass filter is designed, but here we will use a different structure and designing method; also, we will discuss the DGS design process in detail.

II. QUASI-ELLIPTIC BANDPASS FILTER BASED ON SIR

We used folded tri-section stepped impedance resonators to design a four-pole quasi-elliptic bandpass filter. The basic structure of tri-section SIR is shown in Fig. 1(a). The folded SIR is also shown in Fig. 1(c). These resonators not only have

1054-4887 © 2010 ACES

smaller dimensions but also have wider rejection bandwidth comparing to other popular resonators.

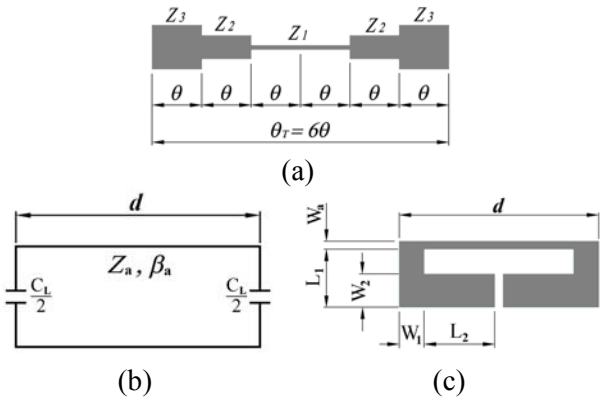

Fig. 1. (a) Basic structure of tri-section SIR resonator. (b) An equivalent circuit of proposed SIR resonator. (c) Proposed folded SIR resonator.

At first, let us consider a capacitively loaded lossless transmission line resonator of Fig. 1(b). C_L, Z_a, β_a, and d represent the loaded capacitance, the characteristic impedance, the propagation constant, and the length of the unloaded line, respectively. Thus, the electric length is $\theta_a = \beta_a d$. The related equations of folded SIR are derived in [1] and [2], such that:

$$\begin{cases} \theta_{a0} = 2\tan^{-1}\left(\dfrac{1}{\pi f_0 Z_a C_L}\right) \\ \theta_{a1} = 2\pi - 2\tan^{-1}\left(\pi f_1 Z_a C_L\right) \end{cases} . \qquad (1)$$

The fundamental resonant frequency and the first spurious resonant frequency are f_0 and f_1, respectively. If C_L equals to zero in the above equation, then θ_{a0} and θ_{a1} equals to π and 2π, respectively. If $C_L \neq 0$, the resonant frequencies shift down as the loaded capacitance increases.

Here, we have assumed $Z_a = 50\ \Omega$, $d = 18.15\ mm$, $W_a = 0.71\ mm$, $V_{Pa} = 1.149 \times 10^8\ m/s$ and V_{Pa} is associated phase velocity. We considered a Rogers RT/duroid 3010 substrate to design our filter; the substrate has a relative dielectric constant of 10.2, a thickness of 0.635 mm and a loss tangent of 0.0035.

The resonator of Fig. 1(c), which is composed of a microstrip line with both ends loaded with folded open-stubs, is used. The folded arms of open-stubs are applied for increasing the loading capacitance to ground for the purpose of cross coupling.

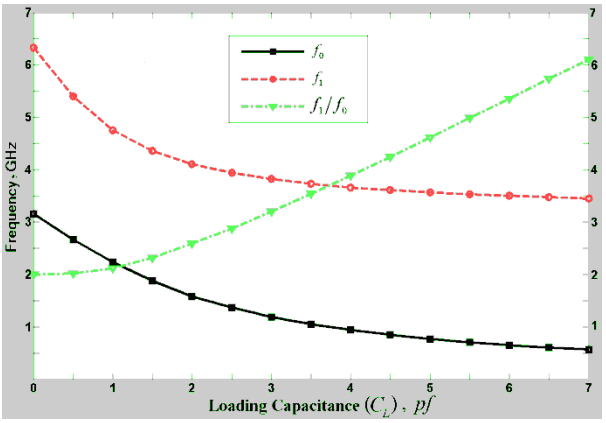

Fig. 2. The fundamental, first spurious resonant frequencies and their ratio versus the loading capacitances.

According to (1), Fig. 2 plots the calculated resonant frequencies, as well as their ratio for different capacitance loading with the above mentioned values. As can be seen when the loading capacitance is increased, in addition to the decrease of both resonant frequencies, the ratio of the first spurious resonant frequency to the fundamental one is increased.

Shown in Fig. 2 are the fundamental and first spurious resonant frequencies as well as their ratio against the loading capacitances, obtained using a full-wave advanced design system (ADS) simulator. According to this Fig, the ratio of the first spurious resonant frequency to the main resonant frequency has direct relation to the loading capacitance. Increasing of the loading capacitance will increase the ratio of the first spurious resonant frequency to the main resonant frequency but the main and the first spurious resonant frequencies will decrease. It is possible to increase the distance between the first spurious and the main resonant frequencies by increasing the loading capacitance. This improves the filter characteristics in rejection band.

Figure 3 shows the fundamental and spurious resonant frequencies together with their ratio versus the length of folded open-stubs. The length of folded open-stubs (L) is obtained from [2]:

$$\begin{cases} L = L_1 & for \quad L \le 6.5\ mm \\ L = 6.5 + L_2 & for \quad L > 6.5\ mm \end{cases} . \qquad (2)$$

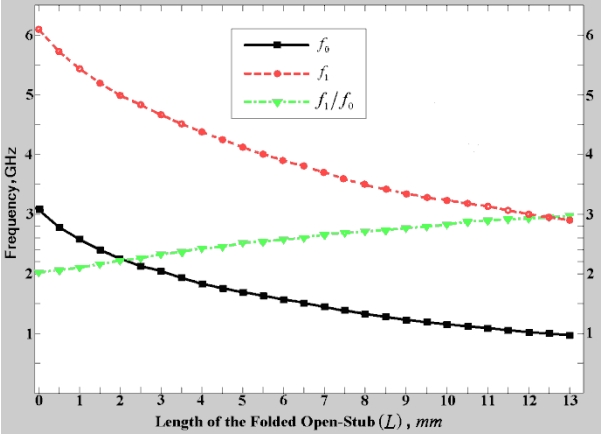

Fig. 3. The fundamental, spurious resonant frequencies and their ratio versus the length of the folded open-stub.

The increase profile of the ratio of the first resonant frequency to the main resonant frequency with the increase of L is similar to the increasing profile of this ratio with C_L. This matter was predictable because both graphs are discussing about an unloaded microstrip line width 18.15 mm length and 0.71 width which exists on a substrate with a relative dielectric constant of 10.2 and a thickness of 0.635 mm, only the open stub of the resonator of Fig. 3 is approximated by a capacitance (Fig. 2). It is important to say that the open-stub should have a wider line or lower characteristic impedance. In this case, according to Fig. 1(c), we have $W_1 = 2\ mm$ and $W_2 = 3.66\ mm$ for the folded open-stub.

To achieve high selectiveness, the order of filter must increase for the Butterworth and Chebyschev filters. Elliptic filter has ripple in the both pass band and rejection band due to having limited transmission zeroes; as a result, it is highly selective and its slope is much more than the above two filters. However, the realization of this type of filter with the printed circuits structure is complicated. The four-pole cross-coupled SIR filter is designed using the proposed basic resonator structure [3].

Figure 4 shows the arrangement of resonators in the quasi-elliptic four-pole SIR filter. Referring to Fig. 4, the coupling between resonators 1 and 4 is of electric type, between 2 and 3 is of magnetic type and between 1 and 2 is of mixed type as well as 3 and 4. More details about electric, magnetic, and mixed coupling between the resonators are discussed in [2].

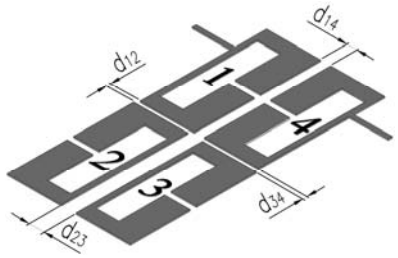

Fig. 4. Schematic of a quasi-elliptic four-pole SIR filter.

In order to design a quasi-elliptic four-pole SIR filter, it is essential to characterize the coupling between adjacent resonators. Fig. 5 shows a typical graph of magnetic coupling between two SIRS's for a desired distance between them, in a certain frequency range. This graph is derived via simulation.

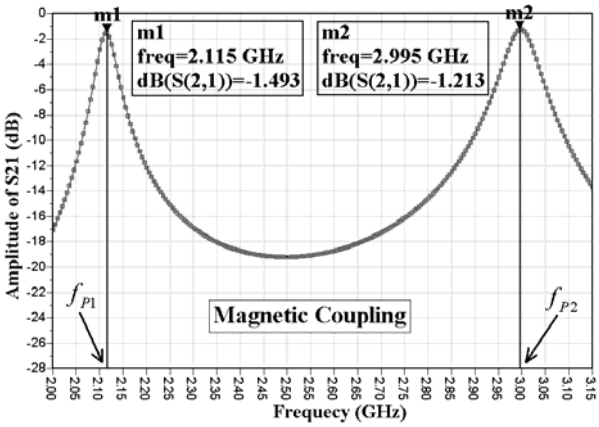

Fig. 5. Typical frequency responses simulated for extracting the coupling coefficient.

The coupling K_{ij} of any pair of adjacent SIR's is determined by [3].

$$K_{ij} = \frac{f_{P2}^2 - f_{P1}^2}{f_{P2}^2 + f_{P1}^2}. \qquad (3)$$

For the example in Fig. 5, the resonant frequencies f_{P1} and f_{P2} are obviously measurable based on amplitude frequency responses. In this sample, the values of resonant frequencies are $f_{P1} = 2.115\ GHz$ and $f_{P2} = 2.995\ GHz$, so according to equation (2), we have:

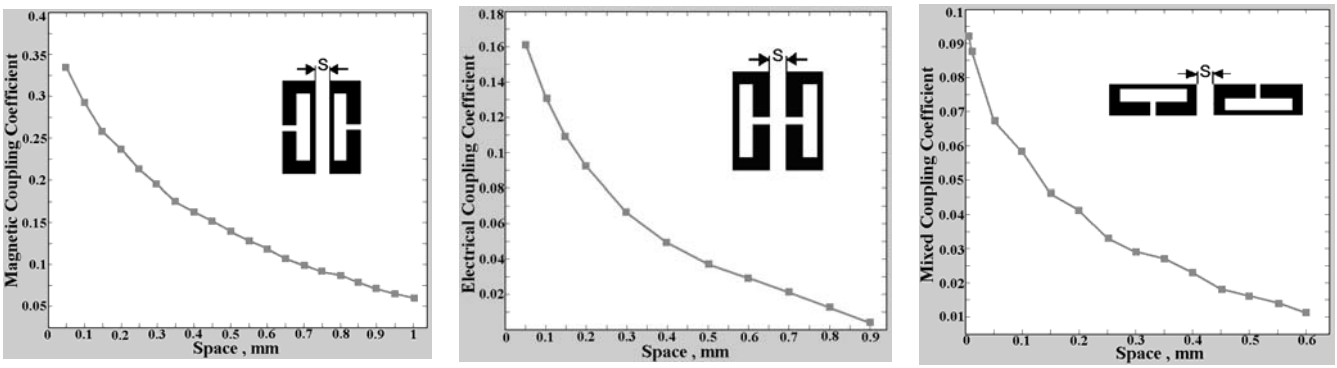

(a) (b) (c)

Fig. 6. Coupling coefficients against space between adjacent resonators (a) magnetic coupling, (b) electric coupling and (c) mixed coupling.

$$K_{23} = 0.334.$$

The graphs of coupling coefficient against space between adjacent resonators are derived according to equation (3) and Fig. 5 for three types of couplings which are used in the design of our filter. These graphs are shown in Fig. 6.

The equations for calculating coupling coefficient of different types of coupling may be obtained as described in [7]:

$$M_{14} = \frac{FBW \cdot J_1}{g_1}$$
$$M_{23} = \frac{FBW \cdot J_2}{g_2} \qquad (4)$$
$$M_{12} = M_{34} = \frac{FBW}{\sqrt{g_1\ g_2}}.$$

The existing factors in (4) are specified for each certain filter characteristics in some tables which are presented in [4]. So the coupling coefficients of our desired filter may be obtained.

By using Fig. 6 spaces between each adjacent resonator may be obtained according to the above specified coupling coefficients. Our desired bandpass filter may be designed by this method.

Based on the substrate we selected, the design parameters of the resonator in Fig. 1(c) and the distance between the resonators of Fig. 4 are summarized in Table 1, with all dimensions shown in millimeters.

The results of the preliminary designed four-pole SIR filter are seen in Fig. 7. One can observe bandpass filter behaviour with central frequency of 0.965 GHz, and bandwidth of 85 MHz. The insertion loss is, also, 1.55 dB and the return loss is better than 23 dB.

Table 1: The values of design parameters of the desired filter

L_1	7.06	W_2	3.66	d_{14}	1.45
L_2	6.58	W_a	0.71	d_{23}	2.11
W_1	2.04	d	18.15	$d_{12} = d_{34}$	0.11

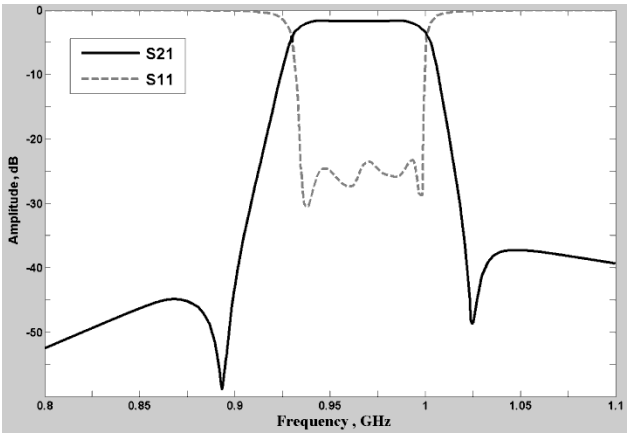

Fig. 7. Simulation of preliminary designed four-pole SIR filter.

Figure 8 shows the simulation results of the rejection band for the four-pole SIR filter. Referring to Fig. 8, the first spurious resonant frequency occurred at 3.2 GHz.

As can be seen, the rejection band width of the designed filter is almost short. Insertion loss at first spurious resonant frequency 3.2 GHz reaches to 5 dB. In order to improve the rejection band

width, we have to eliminate the first spurious frequency. To achieve this, we utilize the defected ground structures (DGS).

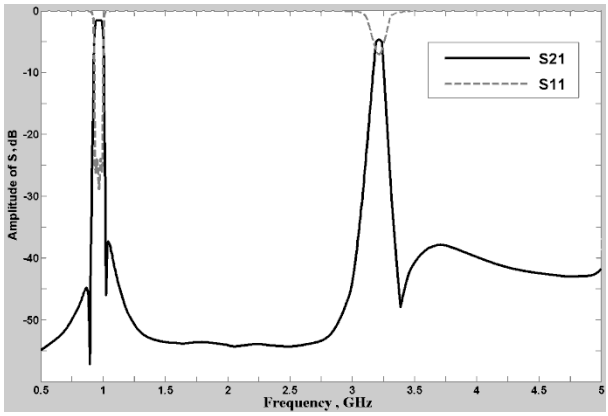

Fig. 8. Simulation of rejection band of the SIR filter.

III. DEFECTED GROUND STRUCTURE

Microstrips structures, with special shapes etched in their ground planes are one of the approaches that researchers use to improve the characteristics of filters. This generic structure is called defected ground structure (DGS). Some advantages of using DGS in filters are simple fabrication, the ability to transfer of high power, low insertion loss and minimization of the filter size. Among various suggested shapes of DGS structures is the rectangular structure due to its simplicity.

An LC equivalent circuit can represent the unit DGS circuit. The equivalent circuit parameters are affected by the physical dimensions of the DGS. The equivalent circuit and parameters of the DGS should be extracted in order to design a circuit with DGS section. One can derive the equivalent circuit of the DGS section using the ADS simulator. The equivalent inductive reactance can be easily calculated by using the prototype element value of the one-pole response.

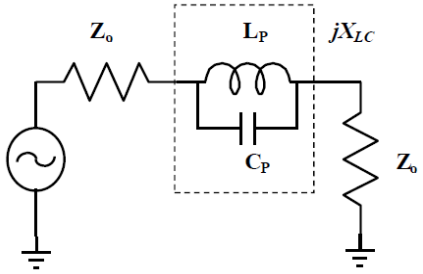

Fig. 9. Equivalent circuit of the DGS circuit.

The parallel capacitance value for the given DGS section can be extracted from the attenuation pole location frequency. The slot in ground plane excited by the microstrip line behaves as parallel resonance. Fig. 9 shows the equivalent circuit of the DGS circuit, where the dotted box shows the DGS section [5].

In Fig. 9, the parallel capacitance value C_P and the parallel inductance value L_P are as follows:

$$C_P = \frac{\omega_C}{Z_0\, g_1\left(\omega_0^2 - \omega_C^2\right)} = \frac{5\, f_C}{\pi\left(f_0^2 - f_C^2\right)} \quad pf\,, \qquad (5a)$$

$$L_P = \frac{250}{C_P\left(\pi\, f_0\right)^2} \quad nH. \qquad (5b)$$

The equivalent reactance value for DGS unit can be expressed as below:

$$jX_{LC} = \frac{j\omega L_P \times \dfrac{1}{j\omega C_P}}{j\omega L_P + \dfrac{1}{j\omega C_P}} = \frac{j\omega L_P}{1-\omega^2 L_P C_P} \qquad (6a)$$

$$\omega_0^2 = \frac{1}{L_P C_P} \qquad (6b)$$

$$X_{LC} = \frac{1}{\omega_0 C_P\left(\dfrac{\omega_0}{\omega} - \dfrac{\omega}{\omega_0}\right)}. \qquad (6c)$$

DGS structures etched under microstrip line increase the inductance and capacitance of line in the rejection band and this, consequently, decreases the propagation velocity. In this situation, the slots in the ground plane cause a portion of density of electrical flow to couple to the side line which in normal design it couples to the ground plane. This will increase the capacitance coupling in coupled lines. Also, because of the type of etched slot on the ground plane, phase velocity of the even and odd modes will be equal. By equalizing the even and odd mode phase velocities it is possible to suppress the first harmonic.

A. Rectangular slots in the direction of coupling line

According to Fig. 10, in this situation of arrangement of DGS unit in the ground plane of coupling lines, slots do not cause any changes in the field lines of the odd mode, but for the even mode, part of electrical field will propagate in the

space under the slot because of the distance between two DGS structures (S_M), Fig. 10 (b). This will decrease the effective relative dielectric coefficient in even mode (ε_{eff}^{e}) [6].

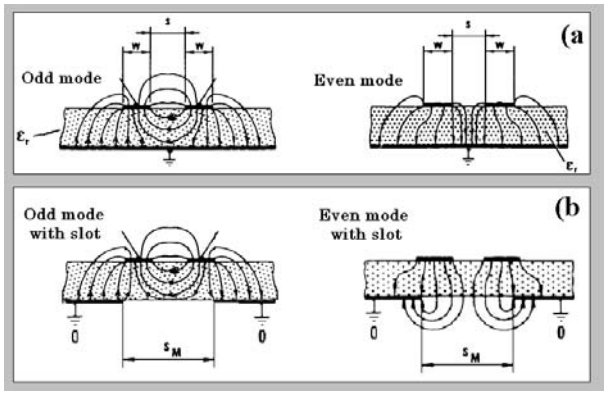

Fig. 10. (a) Electrical filed lines in odd and even modes, in structure of coupling lines without DGS. (b) Electrical filed lines in odd and even modes, in structure of coupling lines with DGS [6].

Etching a slot in a direction of the coupled lines decreases ε_{eff}^{e} and makes it closer in values to ε_{eff}^{o} (the effective relative dielectric coefficient in odd mode). As Fig. 10 shows, ε_{eff}^{o} does not change. So, the difference between phase velocity at even mode and odd mode ($\varepsilon_{eff}^{even} > \varepsilon_{eff}^{odd}$), which exists in normal design, will decrease and the phase velocity of the two modes will become approximately equal. Rectangular slots can be located in different positions in direction of coupling lines which will be discussed. Width, length and location of slots are the main design parameters which increase the coupling and equalize the phase velocity in odd and even modes.

To determine each one of these parameters, two other parameters should be considered as a constant and the influence of changes in the first one on the coupling will be studied. According to Fig. 11 among situations 1, 2, and 3, no. 1 is the most effective one on the coupling. Regarding the width of the slots, three different conditions will be discussed which have better performance than others [5]; first equal to the width of coupling line (W), second equal to the distance between coupling line (S), and third equal to the average of the last two ones (W+S/2). Among these three cases, the second one has the most degree of influence on the coupling. Regarding the effect of length of the slots on the coupling, there are three different options; first equal to half of the length of the coupling line, second equal to the length of the coupling line, and third equal to the total length of the ground plane. The last two options have more influence on coupling compared to the first one. It is notable that between these two, the length equal to the length of the coupling line is more common.

Situation no. 4 in Fig. 11 is a more effective structure to equalize the phase velocity of even and odd phases as well as having great influence on increasing the coupling like the previous study in [5].

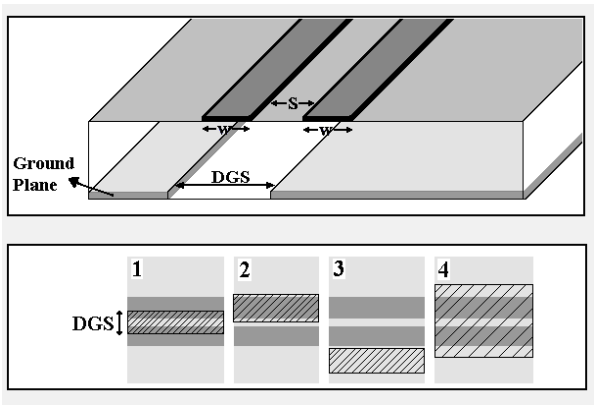

Fig. 11. Different situations of DGS location in ground plane of two coupling lines.

B. Rectangular slots perpendicular to the direction of coupling lines

In this situation, as shown in Fig 10(b), the electrical field lines are similar to the case without DGS; so ε_{eff}^{o} will not change. In even mode, the signal path increases for a special physical length due to the existence of the DGS in the ground plane. This increase in signal path is equal to the decrease of phase velocity in even mode. In other words, ε_{eff}^{e} and ε_{eff}^{o} increase equally. This increase of signal path is similar to the increase of return currents path in ground plane for a simple line with DGS.

In fact, the increase of ε_{eff}^{e} causes more difference between phase velocities in two modes. On the other hand, this increase of ε_{eff}^{e} and no change of ε_{eff}^{o} causes the coupling between the resonator lines to increase, compared to the case without DGS.

IV. IMPROVED MICROSTRIP SIR BANDPASS FILTER USING DEFECTED GROUND STRUCTURES

One method to improve the filter characteristics is to use microstrip structures with defected ground plane. DGS cells are used as complementary of the main filter and also independently in executing the filter, due to having natural resonant characteristics [5]. DGS structures generally affect the filter rejection band. The effects of these structures on improving the filter characteristic in pass band are also discussed. Easily fabrication, low insertion loss, and size reduction of the filters are some advantages of using DGS structure in design of filters [7].

In order to prevent radiation from DGS, we have to know distribution of surface currents on the ground plane of the filter which is shown in Fig. 12.

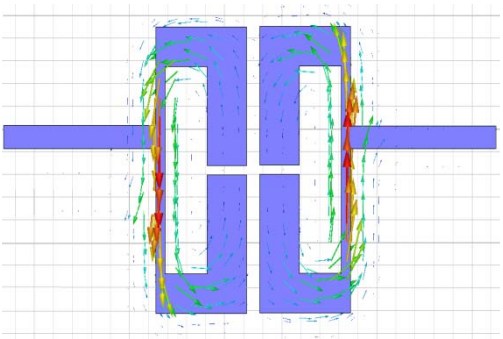

Fig. 12. The distribution of surface currents on the ground plane of the filter.

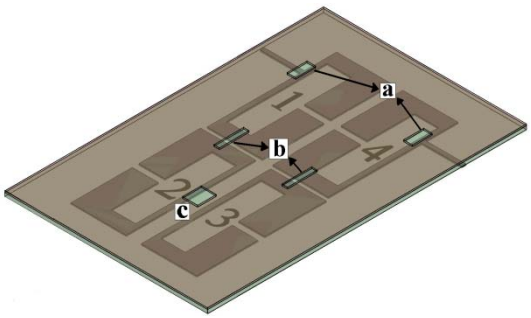

Fig. 13. Schematic of designed four-pole SIR filter with DGS.

For realization of desired DGS structure, considering discussed issues in [7], we utilized a simple linear slot in the ground plane of the preliminary designed filter. Two simple linear slots are etched in the ground plane, one between resonators No. 1 and 2 and the other between resonators No. 3 and 4, in order to improve the mixed coupling between them. The other slots are applied to improve the coupling between the input and output of the filter.

Dimensions of the used DGS slots in Fig. 13 are identified in Table 2, with all dimensions shown in millimeters.

Table 2: Dimension of the DGS slots of Fig. 13

DGS	DGS Length	DGS Width
a	2.8	1.24
b	4.19	0.78
c	2.63	2.11

Figure 14 shows the simulation results of the passband for the four-pole SIR filter with DGS.

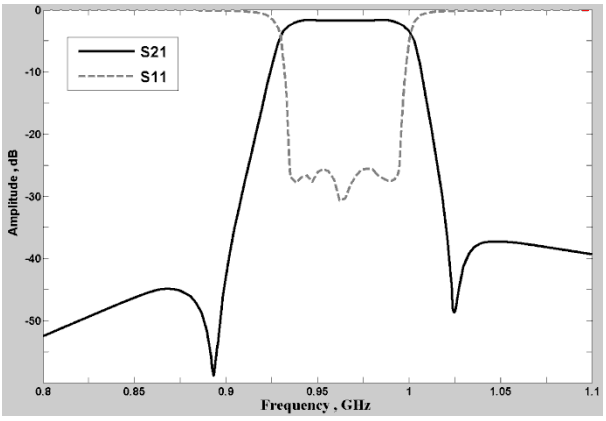

Fig. 14. Simulation results of the pass band for the improved four-pole SIR filter with DGS.

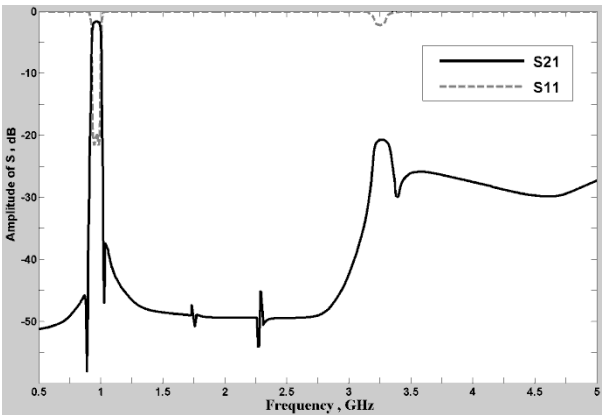

Fig. 15. Simulation results of the SIR filter with DGS in the range 0.5-5 GHz.

As observed in Fig. 14, insertion loss is 1.6 dB and return loss is better than 24 dB. The bandwidth of the filter reached to 85 MHz at 0.965

GHz central frequency which is in a good agreement with the case without DGS.

We can see 16 dB improvements in the insertion loss of the first spurious resonant frequency of the filter according to Fig. 15. In fact, insertion loss at 3.2 GHz reaches 21 dB. In addition, comparing the frequency response of the preliminary SIR filter (without DGS) to the SIR filter with DGS in Fig. 8, we observe elimination of the spurious frequency response in frequency 3.2 GHz. Frequency responses of the filter with and without DGS are compared in Table 3.

Table 3: Comparing the frequency responses of the filter with and without DGS

S parameter	Without DGS	With DGS
Insertion loss at the fundamental frequency (dB)	1.55	1.6
Return loss at the fundamental frequency (dB)	23	24
Insertion loss at the first spurious frequency (dB)	5	21

V. MEASURED RESULTS AND COMPARISON WITH SIMULATED

A sample of four-pole SIR bandpass filter with DGS was fabricated and measured. Photographs of the fabricated filter with DGS are shown in Fig. 16. The prototype circuit size of the filter is around 44.6 mm × 28.4 mm.

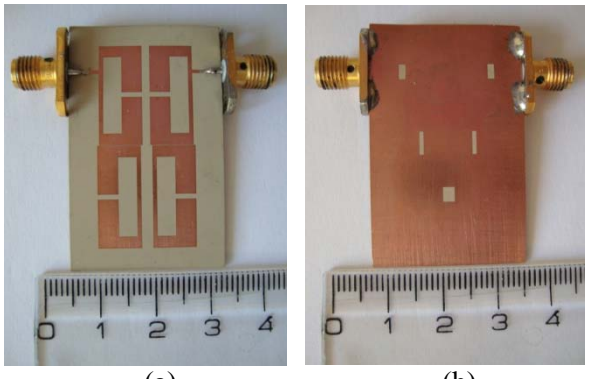

(a) (b)

Fig. 16. Photograph of the fabricated four-pole SIR bandpass filter with DGS (a) top and (b) bottom.

Measurement was carried out using an Agilent HP 8720B Network Analyzer. The results of S-parameter in pass band for the fabricated sample compared to the simulated results are shown in Fig. 17.

As it is observed in Fig. 17, insertion loss of the fabricated model is 2.6 dB at the center frequency, which is about 1 dB higher than the simulation results. In addition, return loss of the fabricated model is 20 dB, which is close to simulation results, as seen in Fig. 17.

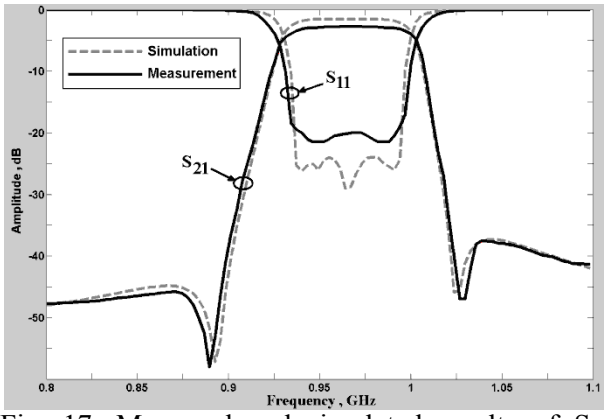

Fig. 17. Measured and simulated results of S-parameter response in pass band.

The measured sample presented a good response in rejection band, as illustrated in Fig. 18. By comparing Fig. 18 to the simulation result (Fig. 15), we observe a good accordance between them.

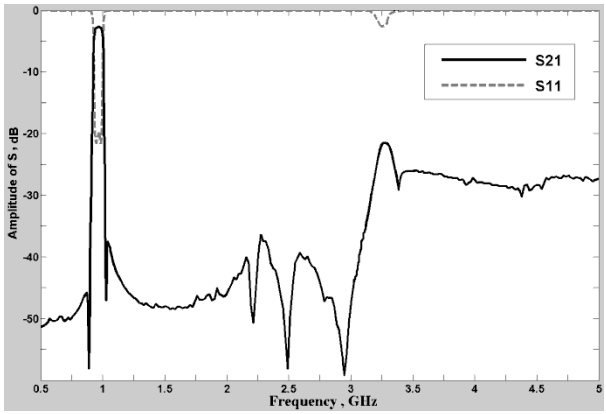

Fig. 18. Measured results in rejection band width.

IV. CONCLUSION

We have designed and fabricated a microstrip quasi-elliptic four-pole cross-coupled FTSIR filter for one of the GSM frequency bands, which may be used in further communication applications. The folded tri-section SIR not only makes the resonator more compact, but also enables the

flexibility of introducing cross coupling in a filter configuration. A comprehensive treatment of a capacitively loaded transmission line resonator is described, which leads us to apply a microstrip folded tri-section stepped impedance resonator. By etching five simple linear slots in the ground plane, we have obtained a great improvement in elimination of the first spurious resonant frequency. The measured results in the pass band and rejection band are in a good agreement with the simulated ones.

REFERENCES

[1] N. Molaei Garmjani and N. Komjani, "Quasi-Elliptic Bandpass Filter Based on SIR With Elimination of First Spurious Response," *Progress In Electromagnetics Research C*, vol. 9, pp. 89-100, 2009.

[2] J. S. Hong and M. J. Lancaster, *Microwave Filters for RF/Microwave Applications*, John Wiley & Sons, 2001.

[3] J. S. Hong and M. J. Lancaster, "Theory and experiment of novel microstrip slow-wave open-loop resonator filters," *IEEE Trans. on Microwave Theory and Tech.,* vol. 45, no. 12, December, 1997.

[4] R. Levy, "Filters with single transmission zeros at real or imaginary frequencies," *IEEE Trans. Microwave Theory Tech.*, vol. MTT-24, pp. 172-181, 1976.

[5] A. Abdel-Rahman, A. K. Verma, A. Boutejdar, and A. S. Omar, "Compact Stub Type Microstrip Bandpass Filter Using Defected Ground Plane, " *IEEE Microwave and Wireless Components Letters*, vol. 14, no. 4, April, 2004.

[6] R. K. Hoffmann, *Handbook of Microwave Integrated Circuits*, Artech House, Norwood, 1987.

[7] D. Ahn, J. S. Park, C. S. Kim, J. Kim, Y. Qian, and T. Itoh, "A Design of the Low-pass Filter using the Novel Microstrip Defected Ground Structure, " *IEEE Trans. Microwave Theory Tech*., vol. 49, no. 1, Jan, 2001.

[8] P. Vágner and M. Kasal, "Bandpass Filter Design Using an Open-Loop Defected Ground Structure Resonator," *15th Conference on Microwave Tech.,* Brno, Czech Republic, 2010.

Nima Molaei Garmjani was born in Tehran, Iran, in 1982. He received the B.S. degree in Electrical Engineering from Azad University, Iran, in 2006, the M.S. degree in Communication Engineering from Iran University of Science and Technology, Tehran, Iran, in 2009. His research interests include the design and analysis of microwave bandpass filter circuits and microstrip stepped impedance resonators (SIR).

Nader Komjani was born in Tehran, Iran, in 1965. He received the B.S., M.S. and Ph.D. degrees in Communication Engineering from Iran University of Science and Technology in 1988, 1991 and 2000, respectively. From 1991 to 1994, he joined the Iranian Science Organization of Science and Technology. His current research interests are in phased array antennas, UWB and multi-band microstrip antenna, and numerical methods in electromagnetic. Currently, he is associated professor and the Director of the Antenna Lab. in the Electrical Engineering Department, Iran University of Science and Technology.

Impact of the Mobile Phone Dimensions on the Hearing Aids Compatibility

I. B. Bonev[1], O. Franek[1], M. Christensen[2], and G. F. Pedersen[1]

[1]Department of Electronics
APNET, Aalborg University, Denmark
ibb@es.aau.dk

[2]Motorola A/S Mobile Devices
Norresundby, Denmark

Abstract- In this work, we have investigated the influence of the mobile phone physical dimensions on the hearing aids compatibility (HAC). In our study, we have considered an inverted F antenna (IFA) and a planar inverted F antenna (PIFA) both fitting into a typical candy bar mobile phone. We have used a generic cubical head model to investigate the user impact on the near fields (NF). The field values are obtained by using the finite difference time domain (FDTD) method. We have observed significant difference in the peak field values between free space and with the head included although only free space values are specified in the relevant standard. Important outcome for the physical dimensions of the mobile phone is that the increase of the length of the handset significantly decreases the peak H value.

I. INTRODUCTION

Several studies have shown that the electromagnetic interference in the hearing aids (HA) due to the GSM digital mobile phones has an annoying effect on the user and a negative influence on the intelligibility of the speech [1-3]. In [4], the presence of discrete peaks in the output spectrum corresponding to the time division multiple access frame rate and its harmonics was shown. In the same study, the interference has been characterized as a buzzing sound. These results were confirmed by a more detailed investigation [5]. A comprehensive study of the NF for typical antennas in mobile handsets does not exist in the open literature. Moreover, the great variety of the HA available on the market complicates the HAC of the mobile phones. This article investigates the influence of the mobile handsets dimensions on the HAC. The IFAs and PIFAs have been investigated for the low band (850 MHz) and high band (1900 MHz) frequency ranges. The conducted analysis is based on the available HAC standard which has been defined for free space [6]. Further, a comparison between free space and with the impact of the head has been carried out to see how well the standard reflects the real case.

II. PREDICTION METHOD

An implementation of a generic mobile handset in the FDTD for computing the electromagnetic field distribution has been presented in [7]. In the same study, the "thin wire" method is used to model the antenna and avoid the "staircasing" effect in FDTD. A parallel FDTD code developed at the Antennas, Propagation and Radio-Networking (APNET) group at Aalborg University has been used for the investigation. The code has been used in a previous study [8]. A cell size of 1 mm which ensures at least twenty samples per wavelength was used. For the termination of the simulation space the perfectly matched layer absorbing boundaries [9] were used.

III. ANTENNA DESIGN AND HEAD MODEL

Figure 1 shows the IFA and PIFA for the low band.

1054-4887 © 2010 ACES

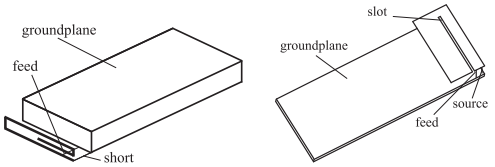

a) b)

Fig. 1. (a) IFA for the low band and (b) PIFA for the low band.

The initial dimension of the mobile handset has been chosen to be 40 x 100 x 10 mm (width x length x thickness). The ground plane and the metallic antenna elements have been modelled as a perfect electric conductor. The heights of the antennas have been chosen in such a way that the proper bandwidth has been established for low and high band cases. The width has been varied to 50, 60, 70 mm; the length to 120, 140, 160, 180, 200 mm; and the thickness to 8, 9, 11, and 12 mm. The IFAs has been placed on the top, on the side or at the bottom of the box phone. The PIFAs has been located on the back top or back bottom of the phone.

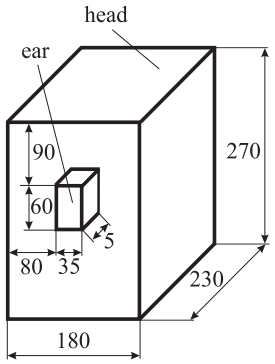

Fig. 2. Generic cubical head model (dimensions in mm).

For simplicity, the head and the ears have been modelled as homogeneous tissue bricks (Fig. 2). The dimensions of the ears have been chosen according to [10]. The thickness of the cubical ear is 5 mm. The electrical properties of the head material have been taken from [11]. We have assumed that the ear consists of fat tissue [12]. In our analysis, we have assumed horizontal orientation of the mobile phone with respect to the head and no gap between the phone and the ear. The mobile phone is positioned in such a way that the speaker, the center of the ear, and the center of the calculation plane (defined in the next part) lie on a line perpendicular to the phone. We have assumed that the speaker is positioned 15 mm from the top edge of the phone.

IV. HAC STANDARD

According to the last version of the available standard, the common operation of a mobile phone and a hearing aid is classified as normal if the HAC category is at least 5. The latter is defined as a sum of the category of the mobile phone (dependent on the measured NF) and the category of the HA (dependent on the HA immunity). Owing to the fact that for the present HA, the achievement of HA category equal to 2 is very easy; the aim for the mobile phone manufacturers is to ensure a mobile phone category of 3 and above. The standard specifies measurement of the NF in a plane 50 by 50 mm at distance 15 mm from the mobile phone (Fig. 3).

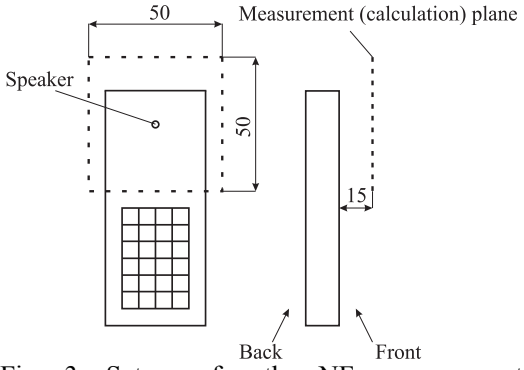

Fig. 3. Set up for the NF measurement according to the available HAC standard.

The phone speaker and the center of the measurement plane lie on a line perpendicular to the phone. After the data are obtained, for both E and H fields, the measurement plane is divided into nine equal sub-grids. For each E and H sub-grid, the maximum value is estimated. In our analysis, the maximum value of the entire measurement plane will have an index m. Then the exclusion procedure has to be applied following the rules:

- The center sub-grid cannot be excluded.
- Three E and three H sub-grids have to be eliminated as at least 4 out of the 6 left sub-grids have to be common for both E and H field.
- For each E and H field, the excluded sub-grids have to be contiguous.

The mobile phone category is defined by the maximum E and H values after the exclusion (these values are called characteristic and in this article are denoted with an index c).

Table 1: Phone emission limits and categories (for frequencies below 960 MHz the values are 10 dB higher)

Category	Telephone RF parameters (above 960 MHz)	
Near Field	E field [dB V/m]	H field [dB A/m]
M1	48.5 to 53.5	-1.9 to 3.1
M2	43.5 to 48.5	-6.9 to -1.9
M3	38.5 to 43.5	-11.9 to -6.9
M4	< 38.5	< -11.9

Table 2: System performance classification

System classification	HAC category
Useable	4
Normal use	5
Excellent performance	6

V. RESULTS AND DISCUSSION

The HAC standard has been defined for the GSM working frequency bands at 850 MHz (low band) and 1900 MHz (high band). These frequencies are used in the USA, Canada, and other countries in the Americas. Of particular interest is to compare the NF produced at these GSM frequency bands with the ones used in the GSM system in Europe. The comparison has been made with respect to the peak electric and magnetic values as we have taken into an account the planar values as defined in the standard and explained in the previous section. To obtain an antenna resonating at lower or higher frequency, we have changed only the length of the radiating element and all other dimensions have been kept constant. Moreover, to be able to fulfill the bandwidth requirements for all four investigated frequency bands, the distance from the wire to the ground-plane for the IFAs has been chosen to be 9 mm. In the case of PIFAs, the minimum investigated height has been 8 mm. The latter was enough to cover the necessary bandwidth. The analysis has been made between all possible antenna configurations obtained via combination of the different physical dimensions of the antennas - width, length, and thickness.

Table 3: Similarity between the NF at close frequencies in free space

Comparison between the NF for close frequencies			Difference in the peak NF between 850 and 900 MHz, [dB]			
Type	Position	Head?	Mean		Deviation	
			ΔE_m	ΔH_m	ΔE_σ	ΔH_σ
IFA	Top	No	0.3	0.8	0.6	0.6
IFA	Top	Yes	0.3	0.5	0.2	0.4
IFA	Side	No	0.5	1	0.1	0.1
IFA	Side	Yes	0.05	0.2	0.2	0.2
IFA	Bottom	No	0.2	0.7	0.2	0.2
IFA	Bottom	Yes	0.1	0.1	0.4	0.2
PIFA	Top	No	0.2	0.3	0.5	0.4
PIFA	Top	Yes	0.3	0.3	0.8	1.1
PIFA	Bottom	No	0.3	0.8	0.2	0.2
PIFA	Bottom	Yes	0.3	0.3	0.1	0.1

Table 4: Similarity between the NF at close frequencies in free space

Comparison between the NF for close frequencies			Difference in the peak NF between 1800 and 1900 MHz, [dB]			
Type	Position	Head?	Mean		Deviation	
			ΔE_m	ΔH_m	ΔE_σ	ΔH_σ
IFA	Top	No	0.4	0.2	0.6	0.4
IFA	Top	Yes	0.3	0.2	0.4	0.3
IFA	Side	No	0.2	0.1	0.3	0.2
IFA	Side	Yes	0.4	0.3	0.3	0.2
IFA	Bottom	No	0.6	0.7	0.1	0.3
IFA	Bottom	Yes	0.3	0.1	0.5	0.3
PIFA	Top	No	0.3	0.1	0.6	0.3
PIFA	Top	Yes	0.2	0.1	0.3	0.2
PIFA	Bottom	No	0.4	0.3	0.1	0.2
PIFA	Bottom	Yes	0.2	0.4	0.3	0.3

As it can be seen from the table, the difference in the peak values is negligible. This is an important conclusion because it gives us the possibility to investigate the NF at the frequency bands defined in the HAC standard and then translate the obtained results for the neighbour frequency bands.

In the analysis of the NF between free space and with the head model, in Table 2 and 3 are shown only the cases for the initial physical dimension of the antennas. Further, if changing any of the dimensions causes a significant difference in the NF for either free space or with the head present, it will be outlined and explained in the text.

For both frequency bands of interest and in the case of top positioned IFAs and PIFAs, the presence of the head model decreases the peak E value compared to the free space cases. For

Table 5: Peak electric and magnetic NF at low band

Antenna type, position	Electric field [dB V/m]				Magnetic field [dB A/m]			
	E_m		E_c		H_m		H_c	
	Free space	With head	Free space	With head	Free space	With head	Free space	With head
IFA, top	60.3	43.3	58.3	43.3	17.4	7.7	1.8	7.6
IFA, bottom	58.4	55.5	57.5	55.3	11.4	8.5	3.5	8.3
PIFA, top	48.6	42	47.9	41.8	4.4	7.8	3.6	7.1
PIFA, bottom	55	42.2	54.8	42	8.6	6.8	0.6	6.8

Table 6: Peak electric and magnetic NF at high band

Antenna type, position	Electric field [dB V/m]				Magnetic field [dB A/m]			
	E_m		E_c		H_m		H_c	
	Free space	With head	Free space	With head	Free space	With head	Free space	With head
IFA, top	52.8	42.5	52.5	42.5	3	7.6	3	7
IFA, bottom	50.1	55.5	46.8	53.8	-1.4	3.6	-3.2	2.8
PIFA, top	53	39.8	52.5	38.8	1.6	5.2	0.8	3
PIFA, bottom	48.8	35.0	48.5	34.8	7.8	0.4	5.1	0.1

both bands and top positioned radiating elements, except the case of top positioned IFA, when comparing the free space with a user, the opposite trend has been observed for the magnetic peak value meaning that the presence of the user increases the peak H value. For that case of top positioned IFA, the interesting fact is the large margin between the peak value H_m and the characteristic value H_c in free space. The peak E and H values are decreased when the head is present compared to free space for bottom low band IFAs and bottom positioned PIFAs. The latter is not the case for bottom located IFA working at high band as both peak electric and magnetic field values increase in the case of a user compared to free space.

In the cases of low and high band bottom positioned IFAs and PIFAs and high band top located IFA for both free space and with an user, increasing the width of the phone from 40 to 70 mm causes reduction of between 3 and 4 dB V/m (A/m) in the peak electric (magnetic) value. For all of the other investigated cases, the width of the handset does not have a significant impact on the peak field values.

The length of the mobile phone appears to be the most important physical dimension. As a general conclusion, increasing the length of the mobile phone from 100 to 200 mm reduces the peak H values.

We have not observed a strict tendency for the influence of the length of the mobile phone on the peak E value. In free space for all different antenna configurations and types, due to the increased length of the mobile phone the reduction of the peak magnetic values is within 4 to 5 dB dB A/m. The decrease in the peak values is stronger with the head present compared to the free space. A simple example has been shown in the next figure.

Figure 4 shows the impact of the length of the mobile phone on the maximum E and H values before and after the exclusion rule was applied for top positioned low band IFA (a) and PIFA (b) with the head presented. The left axis is the E scale, the right axis is the H scale, and the top axis is the mobile phone category specified by the characteristic values E_c (H_c). Each group of four values is specified for a concrete length of the mobile phone as in a consecutive way are shown the electric and magnetic values before and after the exclusion procedure has been applied. For both types of antennas, increasing the length from 100 to 200 mm leads to significant reduction by more than 10 dB A/m of the peak H value, which also will increase the mobile phone category to the value of 3 which will ensure normal common work of the mobile phone with a typical hearing aid. Of all the investigated physical dimensions, the thickness of the mobile phone has the least influence on the NF

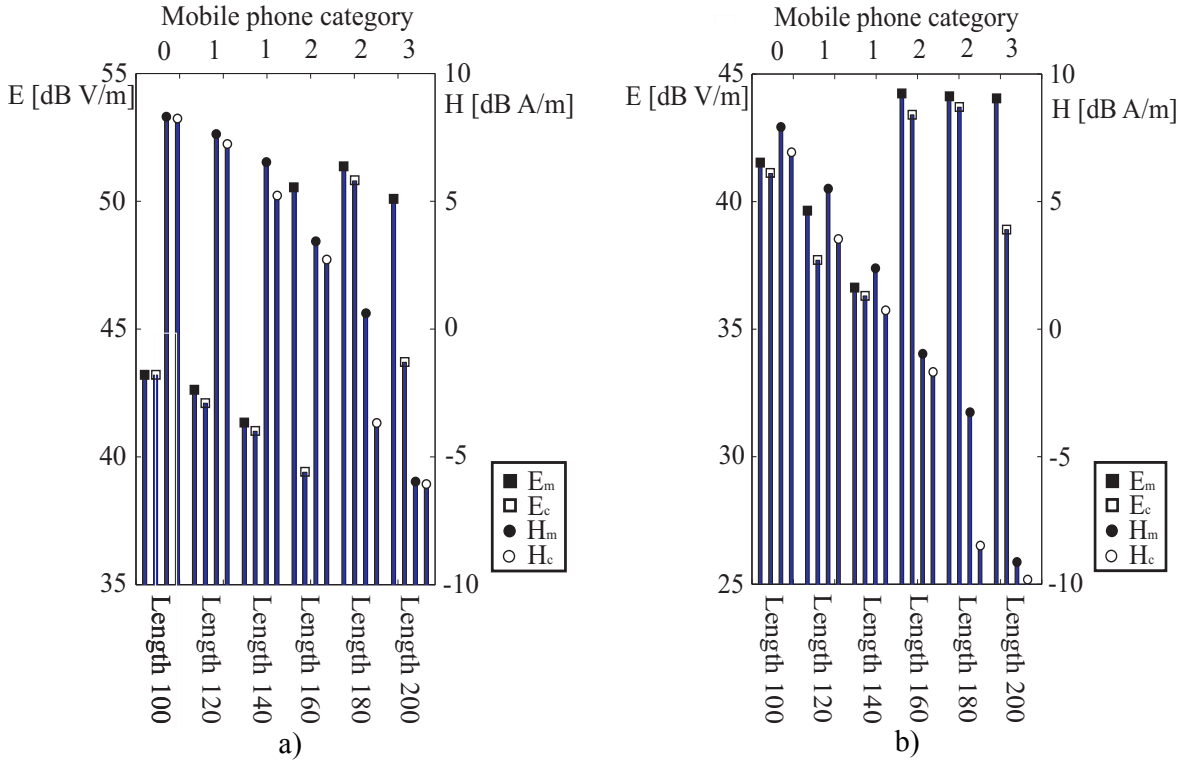

Fig. 4. Bar graphs of maximum E and H values for 850 MHz top positioned antenna with the head present: (a) IFA and (b) PIFA.

values as we have not observed difference in the NF larger than 0.5 dB V/m (dB A/m) when changing the thickness from 8 to 12 mm.

VI. CONCLUSION

In this paper, we have shown that there is a difference in the NF values between free space and with a head. The length of the mobile phone appears to be an important parameter as with its increase, the peak H value decreases. The width and the thickness of the mobile phone do not have significant impact on the NF. The influence of the hand on the NF may, also, need to be explored.

REFERENCES

[1] D. Strange, D. Byrne, K. Joyner, and G. Symons, "Interference to Hearing Aids by the Digital Mobile Telephone System, Global System for Mobile Communications (GSM)," *NAL Report 131*, May 1995.

[2] "Hearing Aids and GSM Mobile Telephones: Interference Problems, Methods of Measurements and Levels of Immunity," *EHIMA GSM Project Final Report*, 1995.

[3] A. Ravindram, R. Schlegel, H. Grant, P. Mathews, and P. Scates, "Study Measures Interference to Hearing Aids from Digital Phones," *The Hearing Journal*, vol. 50, pp. 32-34, April 1997.

[4] M. Scopec, "Hearing Aid Electromagnetic Interference from Digital Cellular Telephones," *18-th Annual International Conference of the IEEE Engineering in Medicine and Biology Society*, 1996.

[5] M. Scopec, "Hearing Aid Electromagnetic Interference from Digital Cellular Telephones," *IEEE Transactions on Rehabilitation Engineering*, vol. 6, no. 2, 1998.

[6] "American National Standard Methods of Measurement of Compatibility between Wireless Communication Devices and Hearing Aids," ANSI C63.19-2007, 2007.

[7] P. S. Excell, P. Olley and N. N. Jackson, "Modelling of an Arbitrarily Oriented Mobile Phone Handset in the Finite Difference Time Domain Field

Computation," *Applied Computational Electromagnetics Society Journal*, vol. 11, no. 2, 1996.

[8] Y. Wang, I. B. Bonev, J. Nielsen, I. Kovacs, and G. F. Pedersen, "Characterization of the Indoor Multi-Antenna Body-to-Body Radio Channel," *IEEE Transactions on Antennas and Propagation*, vol. 56, no. 12, April 2009.

[9] A. Taflove, "Computational electrodynamics: The Finite Difference Time Domain Method," *Artech House Publishers*, Norwood, MA, 2005.

[10] L. Farkas, J. Posnick, and T. Hreczko, "Anthropometric Growth Study of the Ear," *Cleft Palate-Craniofacial Journal*, vol. 29, no. 4, 1992.

[11] "Human exposure to radio frequency fields from hand-held and body-mounted wireless communication devices-human models, instrumentation and procedures, part 1: procedure to determine the specific absorption rate (SAR) for hand-held devices used in close proximity to the ear (frequency range of 300 MHz to 3 GHz)," 2006.

[12] http://niremf.ifac.cnr.it/tissprop/htmlclie/htmlclie.htm#atsftag.

Parametric Analysis of Multi Source Feeding Flare Rolling and Corrugating Effects for H-Plane Horn Radiator

Ahmet S. Turk and Ozan Yurduseven

Department of Electronics and Communication Engineering
Yildiz Technical University, Istanbul, 34349, Turkey
Besiktas, 34349, Istanbul, Turkey
asturk@yildiz.edu.tr

Abstract ─ In this paper, radiation characteristics of H-plane sectoral horn antenna are treated systematically by investigation of the multi source feeding, flare wall rolling and corrugating effects. The analytical regularization method (ARM) is used to solve the problem of E-polarized wave diffraction in a fast and accurate way. The numerical procedure is initially verified by the analytical solutions, and the calculated field patterns are presented for the selected horn antenna configurations. Proper choices of the geometrical parameters, such as source position, back wall shape, multi source feed, metal thickness, and ridged and corrugated flares are proposed for the designers to reach high directivity, narrow beam, and suppressed side and back lobe levels.

Index Terms ─ Analytical regularization method, corrugated horn, flare rolling, horn antenna, multi source feeding.

I. INTRODUCTION

Horn structures are one of the most popular antenna technologies commonly used in wideband RF communication systems, high power microwave devices, electromagnetic compatibility tests, microwave and millimeter wave radars, and parabolic reflector feeder designs [1-6]. The radiation characteristics of horn antennas have been investigated starting from the analysis of principal configurations, and numerous practical types of the horn antennas have been developed in recent years [7-11]. The initial research methods were analytical techniques, which are primarily based on the mode-matching and aperture integration principals [3, 12]. However, the arbitrary shaped horn geometries used in practice were analyzed only by experiments or optical approximations [7]. Thus, direct numerical techniques such as, finite difference time domain (FDTD), finite element method (FEM), method of moments (MoM), and hybrid algorithms are considered more versatile and usable in practical models [13-15]. Nevertheless, they often require a long computing time especially for large size horn designs and wide band analysis [4,14]. Moreover, MoM and FEM can cause unstable numerical process for some structures due to reducing the boundary value problem (BVP) to the algebraic equation set of the first kind that usually has a singular kernel [16]. Hence, the analytical-numerical approaches that transform the ill-conditioned integral equation of first kind into a well-conditioned one of second kind are preferred to solve the matrix equation numerically by truncation method with fast convergence to obtain fast and reliable solutions [9,16]. On this scope, the analytical regularization method (ARM) is proposed for calculation of the horn radiation [17]. The primary analysis of the H-plane horn antenna has been demonstrated by Turk with investigation of the effects of essential parameters such as, different waveguide lengths, widths, flare angles and aperture sizes to characterize the radiation pattern [18].

This study deals with the parametric analysis of radiation from two-dimensional (2D) H-plane horn structure for different geometrical configurations of line source feeder positioning, back wall shaping, multi source locating, and flare rolling and corrugating. The principal aim is to characterize the radiation pattern to achieve low side and back lobe levels. For this purpose, the BVP is essentially formulated with respect to *z*-

1054-4887 © 2010 ACES

component of the electric field satisfying Helmholtz's equation with Dirichlet boundary condition, and the ARM procedure is applied to obtain fast, accurate, and reliable results [5,18]. The numerical results are presented in figures, including performance comparisons with 3D numerical techniques.

II. ARM FORMULATION

The H-plane horn antenna is primarily considered as a perfectly conducting cylindrical obstacle, which is smooth, longitudinally homogeneous, and infinitely long in *z*-direction. The XOY cross section of the structure shown in Fig. 1 is denoted by the closed contour *S*. Let us assume the scalar wave does not vary along *z*-axis. In this case, the scalar diffraction problem of such an object corresponds to the 2D Dirichlet boundary condition for incidence of E-polarized wave. Hence, the incident and scattered scalar wave functions ($u^i(p)$ and $u^s(p)$) should satisfy the Helmholtz equation and the Dirichlet boundary condition given in Eq. (1) and Eq. (2) [16].

$$(\Delta + k^2)u^s(p) = 0, \quad p \in R^2 \setminus S, \tag{1}$$

$$u^{s(+)}(p) = u^{s(-)}(p) = -u^i(p), \quad p \in S, \tag{2}$$

where, *S* is the smooth contour of the structure domain in 2D space R^2 that belongs to the smoothness class $C^{2,\alpha}$ [16]. $u^{s(+)}(p)$ and $u^{s(-)}(p)$ are limiting values of $u^s(p)$ in the inner and the outer sides of *S*, respectively. The solution of the BVP is written in Eq. (3) using the Green's formula and the related boundary condition defined in Eq. (2).

$$-\frac{i}{4}\int_S \left[H_0^{(1)}(k\,|q-p|)Z(p)\right]dl_p = -u^i(q), \quad q, p \in S, \tag{3}$$

where,

$$Z(p) = \frac{\partial u^{s(-)}(p)}{\partial n} - \frac{\partial u^{s(+)}(p)}{\partial n}, \quad p \in S. \tag{4}$$

n is the unit outward with respect to *S* normal of the point *p*. The unknown function *Z(p)* is constructed by solving Eq. (3) and using parameterization of the *S* contour specified by the function $\eta(\theta)=(x(\theta),y(\theta))$ that smoothly parameterizes the contour *S* by the points of $\theta\in[-\pi,\pi]$. The functions $x(\theta)$, $y(\theta)$ are Cartesian-like coordinates of the point $\eta(\theta)\in S$, which are supposed to be infinitely smooth functions after their 2π-periodical continuation on $(-\infty,\infty)$. The parametric representation of the integral equation of the first kind in Eq. (3) can be equivalently rewritten as,

$$\frac{1}{2\pi}\int_{-\pi}^{\pi}\left\{\ln\left|2\sin\frac{\theta-\tau}{2}\right| + K(\theta,\tau)\right\}Z_D(\tau)d\tau = g(\theta), \quad \theta\in[-\pi,\pi], \tag{5}$$

by means of the following $\eta(\theta)$ transformations:

$$Z_D(\theta) = \left([x'(\theta)]^2 + [y'(\theta)]^2\right)^{1/2} Z(\eta(\theta)), \quad \theta\in[-\pi,\pi], \tag{6}$$

$$|q-p| = \left\{[x(\theta)-x(\tau)]^2 + [y(\theta)-y(\tau)]^2\right\}^{1/2}, \quad \theta\in[-\pi,\pi], \tag{7}$$

$$g(\theta) = -u^i(\eta(\theta)), \qquad \theta\in[-\pi,\pi]. \tag{8}$$

In Eq. (5), the unknown function is $Z_D(\tau)$, the given function is $g(\theta)$, and $K(\theta,\tau)$ function is the rather smooth section of the Green's function in comparison with the logarithmic part that contains the main singularity of this equation [17]. The functions are represented by their Fourier series expansions with $k_{s,m}$, z_m, g_m coefficients, as defined in set of Eqs. (9)-(12).

$$K(\theta,\tau) = \sum_{s=-\infty}^{\infty}\sum_{m=-\infty}^{\infty} k_{sm}e^{i(s\theta+m\tau)}, \quad \theta\in[-\pi,\pi], \tag{9}$$

$$\ln\left|2\sin\frac{\theta-\tau}{2}\right| = -\frac{1}{2}\sum_{\substack{n=-\infty\\ n\neq 0}}^{\infty}|n|^{-1}e^{in(\theta-\tau)}, \quad \theta\in[-\pi,\pi], \tag{10}$$

$$Z_D(\tau) = \sum_{n=-\infty}^{\infty} z_n e^{in\tau}, \quad \tau\in[-\pi,\pi], \tag{11}$$

$$g(\theta) = \sum_{n=-\infty}^{\infty} g_n e^{in\theta}, \quad \theta\in[-\pi,\pi]. \tag{12}$$

Finally, one can obtain an infinite system of the linear algebraic equations of the second kind given in Eq. (13).

$$\hat{z}_s + \sum_{m=-\infty}^{\infty}\hat{k}_{s,m}\hat{z}_m = \hat{g}_s, \quad s = \pm1, \pm2, .. \tag{13}$$

where,

$$\hat{k}_{s,m} = -2\tau_s\tau_m\left[k_{s,-m} + (1/2)\delta_{s,0}\delta_{m,0}\right],$$
$$\hat{z}_n = \tau_n^{-1}z_n, \qquad \hat{g}_s = -2\tau_s g_s. \tag{14}$$

Here, $\delta_{s,n}$ is the Kronecker delta function. As a result, Eq. (13) leads to the generic form of equation of the second kind that guarantees the convergence and stability of this numerical process. Therefore, the scattered field $u^s(q)$ for $q\in R^2$ are calculated by the integral equation representation of the Eq. (3) with any required

accuracy by the truncation method [17].

III. PARAMETRIC DESIGN OF H-PLANE HORN ANTENNA

The described ARM procedure is derived for the selected horn antenna types, and the geometrical cross-section of the horn is modeled by ARM as a closed contour L that goes from point A to point T and back to A corresponding to $\theta \in [-\pi, \pi]$, as illustrated in Fig. 1. The relation between l and θ is formulated in Eq. (15).

$$\left.\begin{aligned} & l = (\theta + \pi) L / 2\pi \\ & l \in [0, L] \to (\theta, \tau) \in [-\pi, \pi] \end{aligned}\right\}. \tag{15}$$

Then, the effects on radiation characteristics of the treated design parameters such as, multi source positioning, feeder back wall shaping, and flare wall rolling and corrugating are determined.

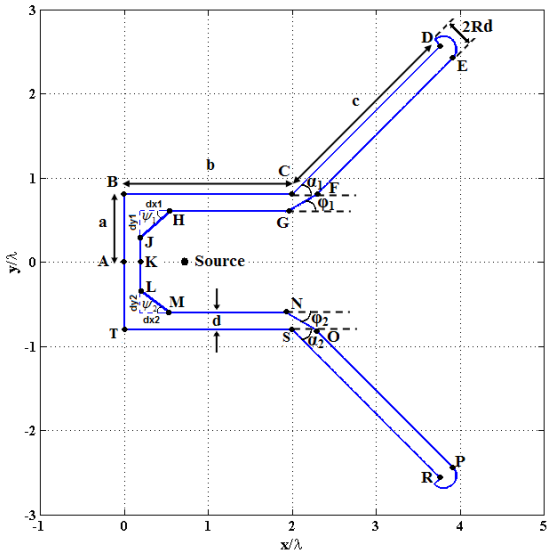

Fig. 1. XOY-plane geometry of H-plane horn.

The horn structure consists of totally 18 contour parts, which are defined in Table 1 and 2. The parameterization of the contour line is implemented separately from point A to T, and back to A by means of the variable $l \in [0, L]$ as follows:

$$x = 0, \quad y = l - L_{AB} + a, \quad l \in [AB) \tag{16}$$

$$x = l - L_{AB}, \quad y = a \quad , l \in [BC) \tag{17}$$

$$\left.\begin{aligned} x &= (l - L_{BC}) \cos\alpha_1 + b \\ y &= (l - L_{BC}) \sin\alpha_1 + a \end{aligned}\right\}, l \in [CD) \tag{18}$$

$$\left.\begin{aligned} x &= \left[\frac{d}{2}\sin\alpha_1 + b + c\cos\alpha_1\right] + R\frac{d}{2}\cos\left[\left(\frac{\pi}{2} + \alpha_1\right) - 2\left(\frac{l - L_{CD}}{Rd}\right)\right] + X_0 \\ y &= \left[-\frac{d}{2}\cos\alpha_1 + a + c\sin\alpha_1\right] + R\frac{d}{2}\sin\left[\left(\frac{\pi}{2} + \alpha_1\right) - 2\left(\frac{l - L_{CD}}{Rd}\right)\right] + Y_0 \\ X_0 &= -(R-1)\frac{d}{2}\sin\alpha_1, \quad Y_0 = (R-1)\frac{d}{2}\cos\alpha_1 \end{aligned}\right\}, l \in [DE) \tag{19}$$

$$\left.\begin{aligned} x &= b + d\sin\alpha_1 + [c - l + L_{DE}]\cos\alpha_1 \\ y &= a - d\cos\alpha_1 + [c - l + L_{DE}]\sin\alpha_1 \end{aligned}\right\}, \quad l \in [EF) \tag{20}$$

$$\left.\begin{aligned} x &= d/\sin\alpha_1 + b - (l - L_{EF})\cos\varphi_1 \\ y &= a - (l - L_{EF})\sin\varphi_1 \end{aligned}\right\}, l \in [FG) \tag{21}$$

$$x = -l + L_{FG} + b - db_1, \quad y = a - d \quad , l \in [GH) \tag{22}$$

$$\left.\begin{aligned} x &= (-l + L_{GH})\cos(\psi_1) + d + dx_1, \\ y &= a - d - (l - L_{GH})\sin(\psi_1), \end{aligned}\right\}, l \in [HJ) \tag{23}$$

$$x = d, \quad y = -l + L_{HJ} + a - d - dy_1, l \in [JK) \tag{24}$$

$$x = d, \quad y = -l + L_{JK}, \; l \in [KL) \tag{25}$$

$$\left.\begin{aligned} x &= d + (l - L_{KL})\cos(\psi_2) \\ y &= -a + d + dy_2 - (l - L_{KL})\sin(\psi_2) \end{aligned}\right\}, l \in [LM) \tag{26}$$

$$x = l - L_{LM} + d + dx_1, \quad y = -a + d, \; l \in [MN) \tag{27}$$

$$\left.\begin{aligned} x &= b - db_2 + (l - L_{MN})\cos\varphi_2 \\ y &= -a + d - (l - L_{MN})\sin\varphi_2 \end{aligned}\right\}, \; l \in [NO) \tag{28}$$

$$\left.\begin{aligned} x &= d/\tan\alpha_2 + b + (l - L_{NO})\cos\alpha_2 + 0.5d\sin\alpha_2 \\ y &= -a - (l - L_{NO})\sin\alpha_2 \end{aligned}\right\}, l \in [OP) \tag{29}$$

$$\left.\begin{aligned} x &= \frac{d}{2}\sin\alpha_2 + b + c\cos\alpha_2 + R\frac{d}{2}\cos\left[\frac{\pi}{2} - \alpha_2 - 2\left(\frac{l - L_{OP}}{Rd}\right)\right] + X_0 \\ y &= -\left(-\frac{d}{2}\cos\alpha_2 + a + c\sin\alpha_2\right) + R\frac{d}{2}\sin\left[\frac{\pi}{2} - \alpha_2 - 2\left(\frac{l - L_{OP}}{Rd}\right)\right] + Y_0 \\ X_0 &= -(R-1)\frac{d}{2}\sin\alpha_2, \quad Y_0 = -(R-1)\frac{d}{2}\cos\alpha_2 \end{aligned}\right\}, l \in [PR) \tag{30}$$

$$\left.\begin{aligned} x &= -(l - L_{PR})\cos\alpha_2 + b + c\cos\alpha_2 \\ y &= (l - L_{PR} - c)\sin\alpha_2 - a \end{aligned}\right\}, l \in [RS) \tag{31}$$

$$x = -l + L_{RS} + b \quad y = -a \quad , \; l \in [ST) \tag{32}$$

$$x = 0, \quad y = l - L_{ST} - a \quad , \; l \in [TA) \tag{33}$$

The horn antenna is supposed to be excited by line source(s) located in the waveguide region at specified pin inset apart from the back wall. Thus, the incident wave at any (*x,y*) coordinate of the horn structure ($u^i(x,y)$) is calculated by the line source radiation formula.

Table 1: Parametric definitions of horn contour

No	Region	Definition
1	*AB*	$-\pi \le \theta < -\pi + 2L_{AB}\,\pi/L$
2	*BC*	$-\pi + 2L_{AB}\,\pi/L \le \theta < -\pi + 2L_{BC}\,\pi/L$
3	*CD*	$-\pi + 2L_{BC}\,\pi/L \le \theta < -\pi + 2L_{CD}\,\pi/L$
4	*DE*	$-\pi + 2L_{CD}\,\pi/L \le \theta < -\pi + 2L_{DE}\,\pi/L$
5	*EF*	$-\pi + 2L_{DE}\,\pi/L \le \theta < -\pi + 2L_{EF}\,\pi/L$
6	*FG*	$-\pi + 2L_{EF}\,\pi/L \le \theta < -\pi + 2L_{FG}\,\pi/L$
7	*GH*	$-\pi + 2L_{FG}\,\pi/L \le \theta < -\pi + 2L_{GH}\,\pi/L$
8	*HJ*	$-\pi + 2L_{GH}\,\pi/L \le \theta < -\pi + 2L_{HJ}\,\pi/L$
9	*JK*	$-\pi + 2L_{HJ}\,\pi/L \le \theta < -\pi + 2L_{JK}\,\pi/L$
10	*KL*	$-\pi + 2L_{JK}\,\pi/L \le \theta < -\pi + 2L_{KL}\,\pi/L$
11	*LM*	$-\pi + 2L_{KL}\,\pi/L \le \theta < -\pi + 2L_{LM}\,\pi/L$
12	*MN*	$-\pi + 2L_{LM}\,\pi/L \le \theta < -\pi + 2L_{MN}\,\pi/L$
13	*NO*	$-\pi + 2L_{MN}\,\pi/L \le \theta < -\pi + 2L_{NO}\,\pi/L$
14	*OP*	$-\pi + 2L_{NO}\,\pi/L \le \theta < -\pi + 2L_{OP}\,\pi/L$
15	*PR*	$-\pi + 2L_{OP}\,\pi/L \le \theta < -\pi + 2L_{PR}\,\pi/L$
16	*RS*	$-\pi + 2L_{PR}\,\pi/L \le \theta < -\pi + 2L_{RS}\,\pi/L$
17	*ST*	$-\pi + 2L_{RS}\,\pi/L \le \theta < -\pi + 2L_{ST}\,\pi/L$
18	*TA*	$-\pi + 2L_{ST}\,\pi/L \le \theta < \pi$

IV. NUMERICAL RESULTS

The parametric analysis of the horn antenna is focused on the investigation of the effects of feeder positioning, back wall shaping, multi source locating, and rolling and corrugating of the flare wall to characterize the radiation pattern. First aim of this work is to minimize the side and back lobes. Before we demonstrate the numerical results, it is important to explain the reliability of the generic ARM algorithm, which has already been verified with analytical results by achieving very good agreements for the cases of plane wave scattering from a circular cylinder and radiation from open ended waveguide [5,18]. The ARM results of one horn type were also compared with analytical solutions additionally, and good agreements were obtained as shown in Fig. 2.

Table 2: Segment lengths of the contour regions

No	Region	Segment Length
1	*AB*	$L_{AB} = a$
2	*BC*	$L_{BC} = L_{AB} + b$
3	*CD*	$L_{CD} = L_{BC} + c$
4	*DE*	$L_{DE} = L_{CD} + \pi Rd/2$
5	*EF*	$L_{EF} = L_{DE} + c - d/\tan\alpha_1$
6	*FG*	$L_{FG} = L_{EF} + d/\sin\varphi_1$
7	*GH*	$L_{GH} = L_{FG} + b - db_1 - d - dx$
8	*HJ*	$L_{HJ} = L_{GH} + \sqrt{(dx_1^2 + dy_1^2)}$
9	*JK*	$L_{JK} = L_{HJ} + a - d - dy_1$
10	*KL*	$L_{KL} = L_{JK} + a - d - dy_2$
11	*LM*	$L_{LM} = L_{KL} + \sqrt{(dx_2^2 + dy_2^2)}$
12	*MN*	$L_{MN} = L_{LM} + b - db_2 - dx_2 - d$
13	*NO*	$L_{NO} = L_{MN} + d/\sin\varphi_2$
14	*OP*	$L_{OP} = L_{NO} + c - d/\tan\alpha_2$
15	*PR*	$L_{PR} = L_{OP} + \pi Rd/2$
16	*RS*	$L_{RS} = L_{PR} + c$
17	*ST*	$L_{ST} = L_{RS} + b$
18	*TA*	$L = L_{ST} + a$
$db_{1,2} = d/\tan\varphi_{1,2} - d\tan\alpha_{1,2}$		

The analysis results for different back wall corner angle, ridged flare, wall thickness, corrugated teeth length, line source positioning at horizontal and vertical axis, and multi source feeding configurations are presented in Fig. 3, Fig. 4, Fig. 5, Fig. 6, Fig. 7, Fig. 8, and Fig. 9, respectively. The major effects are briefly commented as that; the back wall corner can suppress the first side lobes up to 5 dB (see Fig. 3), the flare rolling can decrease both side and back lobes between 5-10 dB (see Fig.4), the thick metal walls can yield 15 dB suppressed back lobes (see Fig. 5), and the corrugating teeth can reach narrowed main beam width with about 5-10 dB improved side and back lobe levels (see Fig. 6). Figsures 7-9 indicate the back lobe suppression and side lobe asymmetry performances of pin inset and multi-pin localizations along *x* and *y* axis.

Figure 10 proposes a flare ridged horn design combined with triple source feeding to obtain 20 dB more suppressed side lobe levels. The multi source fed corrugated horn design shown in Fig. 11 is another antenna proposal that can successfully achieve -40 dB back lobe and -15 dB side lobe levels.

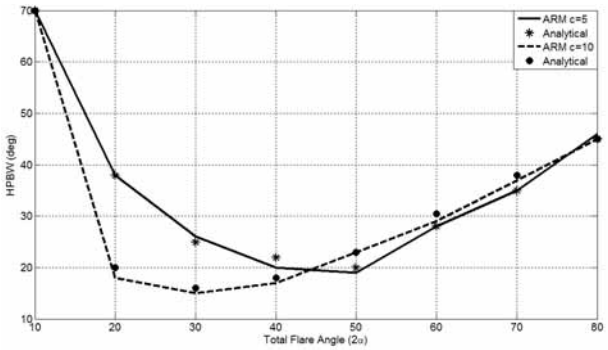

Fig. 2. Half-power beam width plots of ARM calculations and analytical results [3].
(Type 1: a= 0.6λ, b= 4λ, d= 0.1λ, R= 1, α_1= α_2= φ_1= φ_2= α, Ψ_1 = Ψ_2 = 0º)

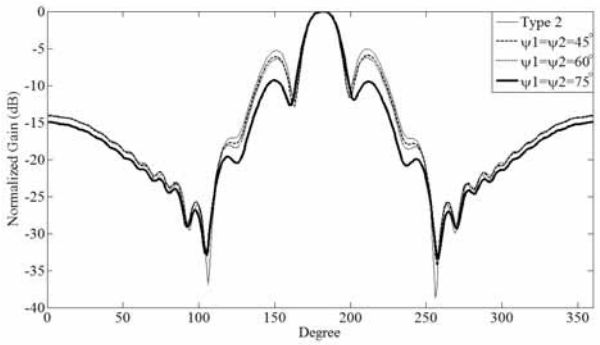

Fig. 3. Normalized radiation patterns of the horn for different back wall corner angles.
(Type 2: a= 1.1λ, b= 2λ, c= 4λ, d= 0.1λ, R= 1, α_1= α_2= 45º, φ_1= φ_2= 45º, dx= 0.25λ)

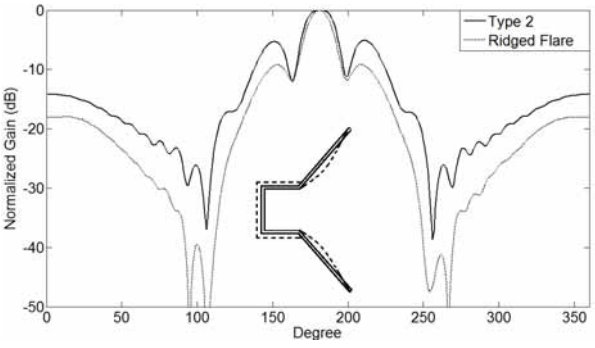

Fig. 4. Normalized radiation pattern of flare rolled type horn.
(Type 2: a= 1.1λ, b= 2λ, c= 4λ, d= 0.1λ, R= 1, α_1= α_2= 45º, φ_1= φ_2= 45º, Ψ_1 = Ψ_2 = 0º)

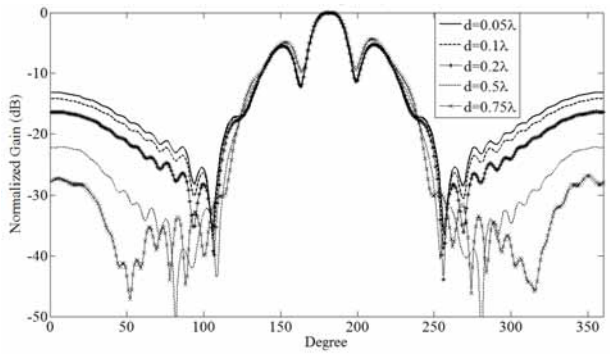

Fig. 5. Normalized radiation patterns of the horn for different wall thicknesses.
(Type 2: a= 1.1λ, b= 2λ, c= 4λ, R= 1, α_1= α_2= 45º, φ_1= φ_2= 45º, Ψ_1 = Ψ_2 = 0º)

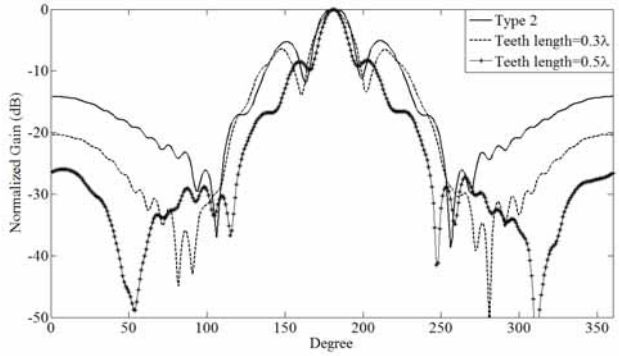

Fig. 6. Normalized radiation patterns of the corrugated horn for different lengths of the teeth.
(Type 2: a= 1.1λ, b= 2λ, c= 4λ, d= 0.1λ, R= 1, α_1= α_2= 45º, Ψ_1 = Ψ_2 = 0º)

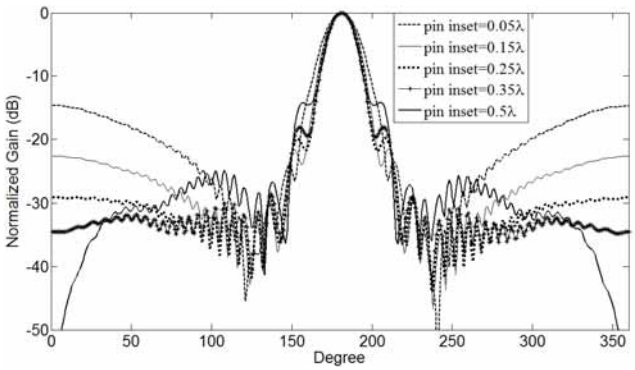

Fig. 7. Normalized radiation patterns of the horn for different pin insets (along x-axis).
(Type 3: a= 0.481λ, b= 2.6λ, c= 8.664λ, d= 0.1λ, α_1= α_2= 11.18º, φ_1= φ_2= 11.18º, Ψ_1 = Ψ_2 = 0º)

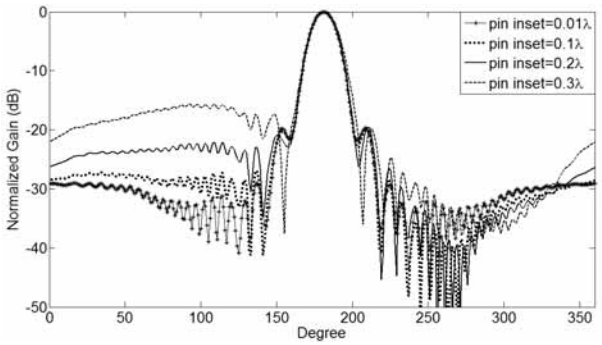

Fig. 8. Normalized radiation patterns of the horn for different pin insets (along *y*-axis).
(Type 3: a= 0.481λ, b= 2.6λ, c= 8.664λ, d= 0.1λ, $\alpha_1 = \alpha_2 = 11.18º$, $\varphi_1 = \varphi_2 = 11.18º$, $\Psi_1 = \Psi_2 = 0º$)

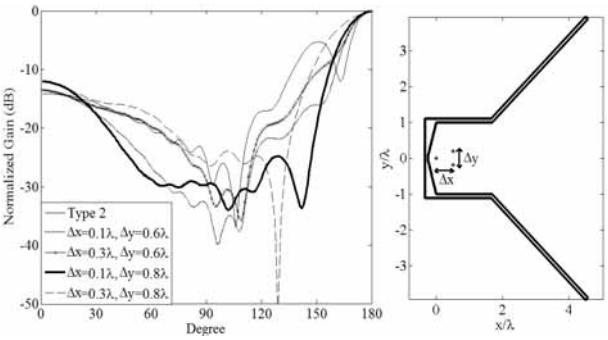

Fig. 9. Normalized radiation patterns of the horn for different triple line source feeding configurations.
(Type 2: a= 1.1λ, b= 2λ, c= 4λ, d= 0.1λ, R= 1, $\alpha_1 = \alpha_2 = 45º$, $\varphi_1 = \varphi_2 = 45º$, $\Psi_1 = \Psi_2 = 75º$)

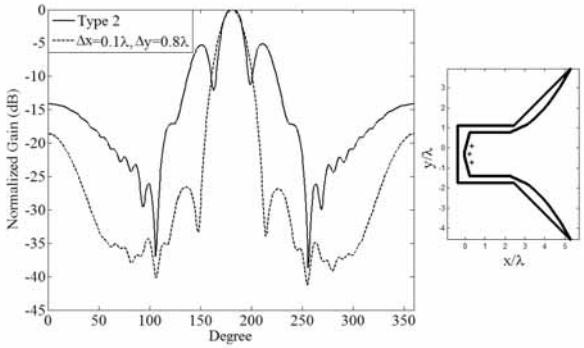

Fig. 10. Normalized radiation pattern of the flare ridged horn version with triple line source feeding.

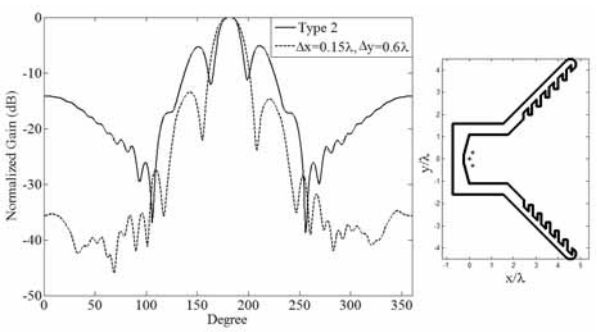

Fig. 11. Normalized radiation pattern of the corrugated horn version with triple line source feeding.

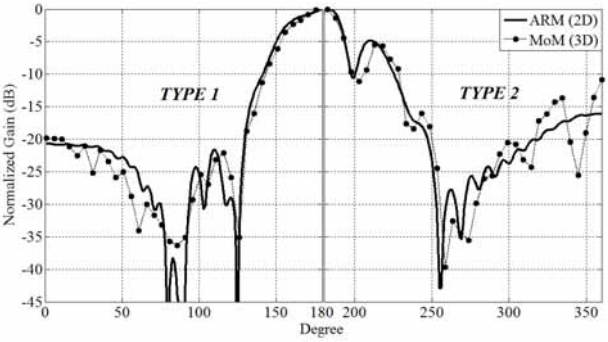

Fig. 12. Comparisons of radiation patterns calculated by 2D ARM and 3D MoM simulator.
(a) Type 1: a= 0.6λ, b= 4λ, c= 4λ, d= 0.1λ, R= 1, $\alpha_1 = \alpha_2 = 45º$
(b) Type 2: a= 1.1λ, b= 2λ, c= 4λ, d= 0.1λ, R= 1, $\alpha_1 = \alpha_2 = 45º$

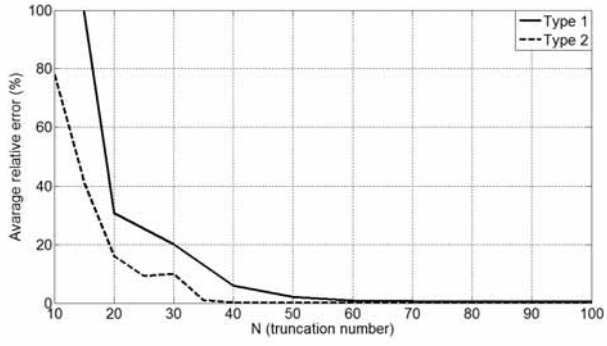

Fig. 13. Average of relative errors in numerical calculations (demonstrated for two horn types).

Finally, the 2D ARM solutions of two different horn types are compared with 3D MoM simulator results. The coherency observed in Fig. 12 implies that ARM is a useful technique due to

fast convergence and short calculation times (see Table 3 and Fig. 13), especially for rough model design and wide band analysis of the horn antennas.

Table 3: Computation times of ARM and 3D MoM simulator (2.53 GHz, 4 GB RAM)

Type	Truncation Number (*N*)	Computation Time	
		2D ARM	3D MoM
1	40	16.92 sec.	13 min. 48 sec.
	60	51.18 sec.	
2	40	16.92 sec.	12 min. 45 sec.
	60	51.18 sec.	
3	40	16.92 sec.	16 min. 23 sec.
	60	51.18 sec.	

V. CONCLUSION

This paper has presented the parametric analysis of the radiation characteristics of the H-plane horn antenna essentially for the geometric versions of multi source feeding, flare rolling, and corrugating. The analytical regularization method is used to perform 2-D analysis of the E-polarized electromagnetic wave scattering problem. The analysis results of different back wall corner angle, ridged flare, wall thickness, corrugated tooth length, vertical and horizontal line source positioning, multi source feeding configurations, and combined proposals are demonstrated on the radiation patterns. The main goal of this work is to provide systematic information for the horn designers to attain desired antenna patterns, such as high gain, narrow beam, and suppressed side and back lobes, in a fast and accurate way.

ACKNOWLEDGMENT

The authors would like to thank to Dr. Yury A. Tuchkin for the contribution in this study.

REFERENCES

[1] M. I. Skolnik, "*Radar handbook,*" 2nd ed., McGraw-Hill, 1990.

[2] T. A. Milligan, "Modern Antenna Design," 2nd ed., *IEEE Press*, John Wiley & Sons, 2005.

[3] C. A. Balanis, "*Antenna Theory Analysis and Design,*" 3rd ed., John Wiley & Sons, 2005.

[4] W. Ewe, L. Li, Q. Wu, and M. Leong, "Analysis of Reflector and Horn Antennas Using Adaptive Integral Methods," *IEICE Trans.* Comm., vol. E88-B, no.6, 2005.

[5] A. S. Turk, "Analysis of aperture illumination and edge rolling effects for parabolic reflector antenna design," *Int. J. Electronics Communications (AEÜ)*, vol. 60, pp. 257-266, 2006.

[6] C. Chang, X. X. Zhu, and Z. Q. Zhang, "Design and experiments of the GW high-power microwave feed horn," *Progress In Electromagnet. Research (PIER)*, vol. 101, pp. 157-171, 2010.

[7] M. Hamid and A. Al-Sulaiman, "New types of dielectric-loaded horn antennas," *Int. Journal of Electronics*, vol. 55, pp. 729-750. 1983.

[8] E. A. Parker, B. Philips, and R. J. Langley, "Experimental variable beam width horn," *Electronic Letters*, vol. 31, pp. 1539-1540, 1995.

[9] V. P. Chumachenko and A. S. Turk, "Radiation characteristics of wide-angle H-plane sectoral horn loaded with dielectric of multiangular shape," *Int. Journal Electronics*, vol. 88, no. 1, pp. 91-101, 2001.

[10] V. Jamnejad and A. Hoorfar, "Design of corrugated horn antennas by evolutionary optimization techniques," *IEEE Antennas and Wireless Prop. Letters*, vol. 3, pp. 276-279, 2004.

[11] D. R. Heydari, H. R. Hassani, and A. R. Mallahzadeh, "A new 2-18 GHz quad-ridged horn antenna," *Progress In Electromagnetics Research (PIER)*, vol. 81, pp. 183-195, 2008.

[12] S. Maci, P. Ya. Ufimtsev, and R. Tiberio, "Equivalence between physical optics and aperture integration for radiation from open-ended waveguides," *IEEE Trans. Antennas Propagation*, vol. 45, no. 1, pp. 183-185, 1997.

[13] C. Reig, E. A. Navarro, and V. Such, "FDTD Analysis of E-sectoral horn antennas for broad-band applications," *IEEE Trans. Antennas Propagation*, vol. 45, pp. 1484-1487, 1997.

[14] F. Arndt, J. Brandt, V. Catina, J. Ritter, I. Rullhusen, J. Dauelsberg, U. Hilgefort, and

W. Wessel, "Fast CAD and optimization of waveguide components and aperture antennas by hybrid MM/FE/MoM/FD methods: State of the art and recent advances," *IEEE Trans. Microwave Theory Tech.*, vol. 52, no.1, 2004.

[15] D. Baumann, C. Fumeaux, P. Leuchtmann, and R. Vahldieck, "Finite-volume time-domain (FVTD) modelling of a broadband double-ridged horn antenna," *Int. J. Numerical Modelling*, vol. 17, pp. 285-298, 2004.

[16] Yu. A. Tuchkin, "Wave scattering by an open cylindrical screen of arbitrary profile with Dirichlet boundary value condition," *Soviet Physics Doclady*, vol. 30, pp. 1027-1030, 1985.

[17] E. Karacuha and A. S. Turk, "E-polarized scalar wave diffraction by perfectly conductive arbitrary shaped cylindrical obstacles with finite thickness," *Int. J. Infrared and Millimeter Waves*, vol. 22, pp. 1531-1546, 2001.

[18] A. S. Turk, O. M. Yucedag, and O. Yurduseven, "Parametric analysis of H-plane horn antenna radiation," Proc. 7th Int. Kharkiv Symposium on Physics and Engineering of Microwaves, Millimeter Submilimeter Waves (MSMW), *IEEE press*, Ukraine, 21-26 June 2010.

Ahmet Serdar Turk received the B.S. degree in Electronics-Communication Engineering from Yıldız Technical University, Istanbul, Turkey in 1996. He received M.S. and Ph.D. degrees in Electronics Engineering from Gebze Institute of Technology, Kocaeli-Turkey in 1998 and 2001, respectively. He joined the Scientific and Technical Research Council of Turkey (TUBITAK) in 1998.

He has been working on land mine detection systems as an impulse radar RF system and antenna designer since 1998. His research interests include horn, reflector, array, and ultra-wide band antenna designs in RF and microwave bands, numerical methods in electromagnetic wave scattering, high frequency surface wave radar, ground penetrating radar, and microwave and millimeter wave radar systems.

He is currently working as associated professor at Yıldız Technical University.

Ozan Yurduseven received the B.S. degree in Electronics- Communication Engineering from Yıldız Technical University, Istanbul, Turkey in 2009. His research interests include microwave antenna design and numerical techniques in electromagnetics, especially method of moments, analytical regularization method, and optimization of radar cross section.

2010 INSTITUTIONAL MEMBERS

DTIC-OCP LIBRARY
8725 John J. Kingman Rd, Ste 0944
Fort Belvoir, VA 22060-6218

AUSTRALIAN DEFENCE LIBRARY
Northcott Drive
Canberra, A.C.T. 2600 Australia

BEIJING BOOK CO, INC
701 E Linden Avenue
Linden, NJ 07036-2495

BUCKNELL UNIVERSITY
69 Coleman Hall Road
Lewisburg, PA 17837

ROBERT J. BURKHOLDER
OHIO STATE UNIVERSITY
1320 Kinnear Road
Columbus, OH 43212

DARTMOUTH COLLEGE
6025 Baker/Berry Library
Hanover, NH 03755-3560

DSTO EDINBURGH
AU/33851-AP, PO Box 830470
Birmingham, AL 35283

SIMEON J. EARL – BAE SYSTEMS
W432A, Warton Aerodome
Preston, Lancs., UK PR4 1AX

ELLEDIEMME
Libri Dal Mondo
PO Box 69/Poste S. Silvestro
Rome, Italy 00187

ENGINEERING INFORMATION, INC
PO Box 543
Amsterdam, Netherlands 1000 Am

ETSE TELECOMUNICACION
Biblioteca, Campus Lagoas
Vigo, 36200 Spain

OLA FORSLUND
SAAB MICROWAVE SYSTEMS
Nettovagen 6
Jarfalla, Sweden SE-17588

GEORGIA TECH LIBRARY
225 North Avenue, NW
Atlanta, GA 30332-0001

HRL LABS, RESEARCH LIBRARY
3011 Malibu Canyon
Malibu, CA 90265

IEE INSPEC
Michael Faraday House
6 Hills Way
Stevenage, Herts UK SG1 2AY

IND CANTABRIA
PO Box 830470
Birmingham, AL 35283

INSTITUTE FOR SCIENTIFIC INFO.
Publication Processing Dept.
3501 Market St.
Philadelphia, PA 19104-3302

KUWAIT UNIVERSITY
Postfach/po box 432
Basel, Switzerland 4900

LIBRARY – DRDC OTTAWA
3701 Carling Avenue
Ottawa, Ontario, Canada K1A OZ4

LIBRARY of CONGRESS
Reg. Of Copyrights
Attn: 407 Deposits
Washington DC, 20559

LINDA HALL LIBRARY
5109 Cherry Street
Kansas City, MO 64110-2498

RAY MCKENZIE – TELESTRA
13/242 Exhibition Street
Melbourne, Vic, Australia 3000

MISSISSIPPI STATE UNIV LIBRARY
PO Box 9570
Mississippi State, MS 39762

MISSOURI S&T
400 W 14th Street
Rolla, MO 56409

MIT LINCOLN LABORATORY
Periodicals Library
244 Wood Street
Lexington, MA 02420

OSAMA MOHAMMED
FLORIDA INTERNATIONAL UNIV
10555 W Flagler Street
Miami, FL 33174

NAVAL POSTGRADUATE SCHOOL
Attn:J. Rozdal/411 Dyer Rd./ Rm 111
Monterey, CA 93943-5101

NDL KAGAKU
C/0 KWE-ACCESS
PO Box 300613 (JFK A/P)
Jamaica, NY 11430-0613

OVIEDO LIBRARY
PO BOX 830679
Birmingham, AL 35283

PENN STATE UNIVERSITY
126 Paterno Library
University Park, PA 16802-1808

DAVID J. PINION
1122 E PIKE STREET #1217
SEATTLE, WA 98122

KATHERINE SIAKAVARA-
ARISTOTLE UNIV OF
THESSALONIKI
Gymnasiou 8
Thessaloniki, Greece 55236

SWETS INFORMATION SERVICES
160 Ninth Avenue, Suite A
Runnemede, NJ 08078

TIB & UNIV. BIB. HANNOVER
DE/5100/G1/0001
Welfengarten 1B
Hannover, Germany 30167

UNIV OF CENTRAL FLORIDA
4000 Central Florida Boulevard
Orlando, FL 32816-8005

UNIVERSITY OF COLORADO
1720 Pleasant Street, 184 UCB
Boulder, CO 80309-0184

UNIVERSITY OF KANSAS –
WATSON
1425 Jayhawk Blvd 210S
Lawrence, KS 66045-7594

UNIVERSITY OF MISSISSIPPI
JD Williams Library
University, MS 38677-1848

UNIVERSITY LIBRARY/HKUST
CLEAR WATER BAY ROAD
KOWLOON, HONG KONG

UNIV POLIT CARTAGENA
Serv Btca Univ,
Paseo Alfonso XIII, 48
Cartagena, Spain 30203

THOMAS WEILAND
TU DARMSTADT
Schlossgartenstrasse 8
Darmstadt, Hessen, Germany 64289

STEVEN WEISS
US ARMY RESEARCH LAB
2800 Powder Mill Road
Adelphi, MD 20783

YOSHIHIDE YAMADA
NATIONAL DEFENSE ACADEMY
1-10-20 Hashirimizu
Yokosuka, Kanagawa,
Japan 239-8686

ACES COPYRIGHT FORM

This form is intended for original, previously unpublished manuscripts submitted to ACES periodicals and conference publications. The signed form, appropriately completed, MUST ACCOMPANY any paper in order to be published by ACES. PLEASE READ REVERSE SIDE OF THIS FORM FOR FURTHER DETAILS.

TITLE OF PAPER:

AUTHORS(S)

PUBLICATION TITLE/DATE:

RETURN FORM TO:

Dr. Atef Z. Elsherbeni
University of Mississippi
Dept. of Electrical Engineering
Anderson Hall Box 13
University, MS 38677 USA

PART A - COPYRIGHT TRANSFER FORM

(NOTE: Company or other forms may not be substituted for this form. U.S. Government employees whose work is not subject to copyright may so certify by signing Part B below. Authors whose work is subject to Crown Copyright may sign Part C overleaf).

The undersigned, desiring to publish the above paper in a publication of ACES, hereby transfer their copyrights in the above paper to The Applied Computational Electromagnetics Society (ACES). The undersigned hereby represents and warrants that the paper is original and that he/she is the author of the paper or otherwise has the power and authority to make and execute this assignment.

Returned Rights: In return for these rights, ACES hereby grants to the above authors, and the employers for whom the work was performed, royalty-free permission to:

1. Retain all proprietary rights other than copyright, such as patent rights.
2. Reuse all or portions of the above paper in other works.
3. Reproduce, or have reproduced, the above paper for the author's personal use or for internal company use provided that (a) the source and ACES copyright are indicated, (b) the copies are not used in a way that implies ACES endorsement of a product or service of an employer, and (c) the copies per se are not offered for sale.
4. Make limited distribution of all or portions of the above paper prior to publication.
5. In the case of work performed under U.S. Government contract, ACES grants the U.S. Government royalty-free permission to reproduce all or portions of the above paper, and to authorize others to do so, for U.S. Government purposes only.

ACES Obligations: In exercising its rights under copyright, ACES will make all reasonable efforts to act in the interests of the authors and employers as well as in its own interest. In particular, ACES REQUIRES that:

1. The consent of the first-named author be sought as a condition in granting re-publication permission to others.
2. The consent of the undersigned employer be obtained as a condition in granting permission to others to reuse all or portions of the paper for promotion or marketing purposes.

In the event the above paper is not accepted and published by ACES or is withdrawn by the author(s) before acceptance by ACES, this agreement becomes null and void.

AUTHORIZED SIGNATURE — TITLE (IF NOT AUTHOR)

EMPLOYER FOR WHOM WORK WAS PERFORMED — DATE FORM SIGNED

Part B - U.S. GOVERNMENT EMPLOYEE CERTIFICATION

(NOTE: if your work was performed under Government contract but you are not a Government employee, sign transfer form above and see item 5 under Returned Rights).

This certifies that all authors of the above paper are employees of the U.S. Government and performed this work as part of their employment and that the paper is therefor not subject to U.S. copyright protection.

AUTHORIZED SIGNATURE — TITLE (IF NOT AUTHOR)

NAME OF GOVERNMENT ORGANIZATION — DATE FORM SIGNED

PART C - CROWN COPYRIGHT

(NOTE: ACES recognizes and will honor Crown Copyright as it does U.S. Copyright. It is understood that, in asserting Crown Copyright, ACES in no way diminishes its rights as publisher. Sign only if *ALL* authors are subject to Crown Copyright).

This certifies that all authors of the above Paper are subject to Crown Copyright. (Appropriate documentation and instructions regarding form of Crown Copyright notice may be attached).

AUTHORIZED SIGNATURE TITLE OF SIGNEE

NAME OF GOVERNMENT BRANCH DATE FORM SIGNED

Information to Authors

ACES POLICY

ACES distributes its technical publications throughout the world, and it may be necessary to translate and abstract its publications, and articles contained therein, for inclusion in various compendiums and similar publications, etc. When an article is submitted for publication by ACES, acceptance of the article implies that ACES has the rights to do all of the things it normally does with such an article.

In connection with its publishing activities, it is the policy of ACES to own the copyrights in its technical publications, and to the contributions contained therein, in order to protect the interests of ACES, its authors and their employers, and at the same time to facilitate the appropriate re-use of this material by others.

The new United States copyright law requires that the transfer of copyrights in each contribution from the author to ACES be confirmed in writing. It is therefore necessary that you execute either Part A-Copyright Transfer Form or Part B-U.S. Government Employee Certification or Part C-Crown Copyright on this sheet and return it to the Managing Editor (or person who supplied this sheet) as promptly as possible.

CLEARANCE OF PAPERS

ACES must of necessity assume that materials presented at its meetings or submitted to its publications is properly available for general dissemination to the audiences these activities are organized to serve. It is the responsibility of the authors, not ACES, to determine whether disclosure of their material requires the prior consent of other parties and if so, to obtain it. Furthermore, ACES must assume that, if an author uses within his/her article previously published and/or copyrighted material that permission has been obtained for such use and that any required credit lines, copyright notices, etc. are duly noted.

AUTHOR/COMPANY RIGHTS

If you are employed and you prepared your paper as a part of your job, the rights to your paper initially rest with your employer. In that case, when you sign the copyright form, we assume you are authorized to do so by your employer and that your employer has consented to all of the terms and conditions of this form. If not, it should be signed by someone so authorized.

NOTE RE RETURNED RIGHTS: Just as ACES now requires a signed copyright transfer form in order to do "business as usual", it is the intent of this form to return rights to the author and employer so that they too may do "business as usual". If further clarification is required, please contact: The Managing Editor, R. W. Adler, Naval Postgraduate School, Code EC/AB, Monterey, CA, 93943, USA (408)656-2352.

Please note that, although authors are permitted to re-use all or portions of their ACES copyrighted material in other works, this does not include granting third party requests for reprinting, republishing, or other types of re-use.

JOINT AUTHORSHIP

For jointly authored papers, only one signature is required, but we assume all authors have been advised and have consented to the terms of this form.

U.S. GOVERNMENT EMPLOYEES

Authors who are U.S. Government employees are not required to sign the Copyright Transfer Form (Part A), but any co-authors outside the Government are.

Part B of the form is to be used instead of Part A only if all authors are U.S. Government employees and prepared the paper as part of their job.

NOTE RE GOVERNMENT CONTRACT WORK: Authors whose work was performed under a U.S. Government contract but who are not Government employees are required so sign Part A-Copyright Transfer Form. However, item 5 of the form returns reproduction rights to the U. S. Government when required, even though ACES copyright policy is in effect with respect to the reuse of material by the general public.

APPLIED COMPUTATIONAL ELECTROMAGNETICS SOCIETY JOURNAL
http://aces.ee.olemiss.edu

INFORMATION FOR AUTHORS

PUBLICATION CRITERIA

Each paper is required to manifest some relation to applied computational electromagnetics. **Papers may address general issues in applied computational electromagnetics, or they may focus on specific applications, techniques, codes, or computational issues.** While the following list is not exhaustive, each paper will generally relate to at least one of these areas:

1. **Code validation.** This is done using internal checks or experimental, analytical or other computational data. Measured data of potential utility to code validation efforts will also be considered for publication.

2. **Code performance analysis.** This usually involves identification of numerical accuracy or other limitations, solution convergence, numerical and physical modeling error, and parameter tradeoffs. However, it is also permissible to address issues such as ease-of-use, set-up time, run time, special outputs, or other special features.

3. **Computational studies of basic physics.** This involves using a code, algorithm, or computational technique to simulate reality in such a way that better, or new physical insight or understanding, is achieved.

4. **New computational techniques** or new applications for existing computational techniques or codes.

5. **"Tricks of the trade"** in selecting and applying codes and techniques.

6. **New codes, algorithms, code enhancement, and code fixes.** This category is self-explanatory, but includes significant changes to existing codes, such as applicability extensions, algorithm optimization, problem correction, limitation removal, or other performance improvement. **Note: Code (or algorithm) capability descriptions are not acceptable, unless they contain sufficient technical material to justify consideration.**

7. **Code input/output issues.** This normally involves innovations in input (such as input geometry standardization, automatic mesh generation, or computer-aided design) or in output (whether it be tabular, graphical, statistical, Fourier-transformed, or otherwise signal-processed). Material dealing with input/output database management, output interpretation, or other input/output issues will also be considered for publication.

8. **Computer hardware issues.** This is the category for analysis of hardware capabilities and limitations of various types of electromagnetics computational requirements. Vector and parallel computational techniques and implementation are of particular interest.

Applications of interest include, but are not limited to, antennas (and their electromagnetic environments), networks, static fields, radar cross section, inverse scattering, shielding, radiation hazards, biological effects, biomedical applications, electromagnetic pulse (EMP), electromagnetic interference (EMI), electromagnetic compatibility (EMC), power transmission, charge transport, dielectric, magnetic and nonlinear materials, microwave components, MEMS, RFID, and MMIC technologies, remote sensing and geometrical and physical optics, radar and communications systems, sensors, fiber optics, plasmas, particle accelerators, generators and motors, electromagnetic wave propagation, non-destructive evaluation, eddy currents, and inverse scattering.

Techniques of interest include but not limited to frequency-domain and time-domain techniques, integral equation and differential equation techniques, diffraction theories, physical and geometrical optics, method of moments, finite differences and finite element techniques, transmission line method, modal expansions, perturbation methods, and hybrid methods.

Where possible and appropriate, authors are required to provide statements of quantitative accuracy for measured and/or computed data. This issue is discussed in "Accuracy & Publication: Requiring, quantitative accuracy statements to accompany data," by E. K. Miller, *ACES Newsletter,* Vol. 9, No. 3, pp. 23-29, 1994, ISBN 1056-9170.

SUBMITTAL PROCEDURE

All submissions should be uploaded to ACES server through ACES web site (http://aces.ee.olemiss.edu) by using the upload button, journal section. Only pdf files are accepted for submission. The file size should not be larger than 5MB, otherwise permission from the Editor-in-Chief should be obtained first. Automated acknowledgment of the electronic submission, after the upload process is successfully completed, will be sent to the corresponding author only. It is the responsibility of the corresponding author to keep the remaining authors, if applicable, informed. Email submission is not accepted and will not be processed.

PAPER FORMAT (INITIAL SUBMISSION)

The preferred format for initial submission manuscripts is 12 point Times Roman font, single line spacing and single column format, with 1 inch for top, bottom, left, and right margins. Manuscripts should be prepared for standard 8.5x11 inch paper.

EDITORIAL REVIEW

In order to ensure an appropriate level of quality control, papers are peer reviewed. They are reviewed both for

technical correctness and for adherence to the listed guidelines regarding information content and format.

PAPER FORMAT (FINAL SUBMISSION)

Only camera-ready electronic files are accepted for publication. The term **"camera-ready" means that the material is neat, legible, reproducible, and in accordance with the final version format listed below.**

The following requirements are in effect for the final version of an ACES Journal paper:

1. The paper title should not be placed on a separate page. The title, author(s), abstract, and (space permitting) beginning of the paper itself should all be on the first page. The title, author(s), and author affiliations should be centered (center-justified) on the first page. The title should be of font size 16 and bolded, the author names should be of font size 12 and bolded, and the author affiliation should be of font size 12 (regular font, neither italic nor bolded).

2. An abstract is required. The abstract should be a brief summary of the work described in the paper. It should state the computer codes, computational techniques, and applications discussed in the paper (as applicable) and should otherwise be usable by technical abstracting and indexing services. The word "Abstract" has to be placed at the left margin of the paper, and should be bolded and italic. It also should be followed by a hyphen (—) with the main text of the abstract starting on the same line.

3. All section titles have to be centered and all the title letters should be written in caps. The section titles need to be numbered using roman numbering (I. II. ….)

4. Either British English or American English spellings may be used, provided that each word is spelled consistently throughout the paper.

5. Internal consistency of references format should be maintained. As a guideline for authors, we recommend that references be given using numerical numbering in the body of the paper (with numerical listing of all references at the end of the paper). The first letter of the authors' first name should be listed followed by a period, which in turn, followed by the authors' complete last name. Use a coma (,) to separate between the authors' names. Titles of papers or articles should be in quotation marks (" "), followed by the title of journal, which should be in italic font. The journal volume (vol.), issue number (no.), page numbering (pp.), month and year of publication should come after the journal title in the sequence listed here.

6. Internal consistency shall also be maintained for other elements of style, such as equation numbering. As a guideline for authors who have no other preference, we suggest that equation numbers be placed in parentheses at the right column margin.

7. The intent and meaning of all text must be clear. For authors who are not masters of the English language, the ACES Editorial Staff will provide assistance with grammar (subject to clarity of intent and meaning). However, this may delay the scheduled publication date.

8. Unused space should be minimized. Sections and subsections should not normally begin on a new page.

ACES reserves the right to edit any uploaded material, however, this is not generally done. It is the author(s) responsibility to provide acceptable camera-ready pdf files. Incompatible or incomplete pdf files will not be processed for publication, and authors will be requested to re-upload a revised acceptable version.

COPYRIGHTS AND RELEASES

Each primary author must sign a copyright form and obtain a release from his/her organization vesting the copyright with ACES. Copyright forms are available at ACES, web site (http://aces.ee.olemiss.edu). To shorten the review process time, the executed copyright form should be forwarded to the Editor-in-Chief immediately after the completion of the upload (electronic submission) process. Both the author and his/her organization are allowed to use the copyrighted material freely for their own private purposes.

Permission is granted to quote short passages and reproduce figures and tables from and ACES Journal issue provided the source is cited. Copies of ACES Journal articles may be made in accordance with usage permitted by Sections 107 or 108 of the U.S. Copyright Law. This consent does not extend to other kinds of copying, such as for general distribution, for advertising or promotional purposes, for creating new collective works, or for resale. The reproduction of multiple copies and the use of articles or extracts for commercial purposes require the consent of the author and specific permission from ACES. Institutional members are allowed to copy any ACES Journal issue for their internal distribution only.

PUBLICATION CHARGES

All authors are allowed for 8 printed pages per paper without charge. Mandatory page charges of $75 a page apply to all pages in excess of 8 printed pages. Authors are entitled to one, free of charge, copy of the journal issue in which their paper was published. Additional reprints are available for a nominal fee by submitting a request to the managing editor or ACES Secretary.

Authors are subject to fill out a one page over-page charge form and submit it online along with the copyright form before publication of their manuscript.

ACES Journal is abstracted in INSPEC, in Engineering Index, DTIC, Science Citation Index Expanded, the Research Alert, and to Current Contents/Engineering, Computing & Technology.